An Experimental Study of Longitudinally Embedded Vortices in a Turbulent Boundary Layer via the Non-Invasive Comprehensive LDV Technique

Joseph Michael Derlaga

Thesis submitted to the faculty of the

Virginia Polytechnic Institute and State University

in partial fulfillment of the requirements for the degree of

Master of Science

In

Aerospace Engineering

Roger L. Simpson, Chair

William J. Devenport

Christopher J. Roy

April 30, 2012

Blacksburg, Virginia

Keywords: non-intrusive flow measurement, laser Doppler velocimetry, laser Doppler anemometry, boundary layers, Reynolds stresses, turbulence

An Experimental Study of Longitudinally Embedded Vortices in a Turbulent Boundary Layer via the Non-Invasive Comprehensive LDV Technique

Joseph Michael Derlaga

(ABSTRACT)

This report documents the measurements of turbulence quantities resulting from vortices embedded in a zero pressure gradient turbulent boundary layer. Turbulent boundary layers are found in most flow regimes over large scale vehicles and have been studied for many years. Various systems to control separation of boundary layers have been proposed, but vortex generators have proven to be an economical choice as they are often used to fix deficiencies in a flow field after large scale production of a vehicle has commenced. In order to better understand the interaction between vortex generators and the boundary layer in which they are embedded, an experiment has been performed using through non-invasive Comprehensive Laser Doppler Velocimeter.

The results show that normalization on edge velocity is appropriate for comparison with previous work. The 1/S parameter and $\overline{vq^2}$ parameter were found to be most appropriate to correlate the Reynolds stresses and triple products, respectively. The higher inflow edge velocity and greater momentum thickness, creating a lower vortex generator to boundary layer height ratio, result in a more diffuse vortex as compared to previous work conducted in the same wind tunnel, with the same geometry, but with different inflow conditions.

Acknowledgements

I must thank the National Science Foundation for the funding to conduct this research,as well as Dr. Roger Simpson for giving me the chance to do this research and for his guidance throughout this process which has given me better insight into the issues of computational turbulence modeling and has already allowed me to bridge gaps between experimental and computational aerodynamics. I am grateful to Dr. William Devenport for his guidance in technical writing and to Dr. Christopher Roy for his patience as I completed this work.

Special thanks go to Dr. K. Todd Lowe, Dr. Nathaniel Varano, and Dr. Andrew Hopkins, all of whom helped to teach me how to properly operate the CompLDV. Dr. Gwibo Byun, Dr. Joshua DeMoss, Deirdre Hunter, and Max Rusche have my gratitude for all the help they loaned while I was working in the lab.

This work could not have been completed without the help of the AOE machine shop, nor without the help of the fine members of the AOE office staff. Steve Edwards must be noted for his help with maintaining the Enterprise supercomputer and allowing me to help with bringing many processors back online. I thank my parents, John and Karen, as well as my brother Jake who often gave a much needed helping hand in the lab while he was an undergraduate. Finally, I thank my wife Anna Pearl who was with me throughout this work and helped to review this thesis.

All photographs in this work were taken by the author.

Contents

List of Figures

List of Tables

Chapter 1. Overview

1.1 Purpose

The goal of this study was to experimentally interrogate the near wall structure of contra-rotating vortices embedded in a two-dimensional turbulent boundary layer. Through the use of the Comprehensive Laser Doppler Velocimeter, this study contributes a high quality, non-invasive data set to the current body of knowledge, which had previously focused on the mean vortical structure of embedded vortices using invasive techniques. This study will allow for finer study of the closure assumptions of existing turbulence models used in conjunction with the Reynolds Averaged Navier-Stokes (RANS) equations, as well as those models utilized by Large Eddy Simulations (LES) and Detached Eddy Simulations (DES).

1.2 Background and Motivation

Vortex generating devices are commonly used to improve heat transfer in turbomachinery or to delay separation over aerodynamic surfaces, as stated by Lin [2002]. Flow separation can be a large contributor to drag on an aircraft or detrimental to the performance of high lift devices. While many concepts have been proposed to prevent flow separation, none are as simple, cheap, and easy to maintain as vortex generators. The benefits of vortex generators are balanced by an increase in parasite drag, which, as Lin [2002] states, must be taken into account when designing the vortex generator. These devices are typically installed when deficiencies are found during prototype test flights to address issues not predicted during initial design studies.

While computational methods are increasingly used during initial design studies, accurate

predictions of flow field physics over all flight regimes are not yet within the abilities of current computational technology. Depending upon when flow field deficiencies are found during initial design, it is practical to study the effect of adding vortex generators to the computational model to fix any computed deficiencies rather than relying on costly wind tunnel or flight tests. However, it is generally necessary to regenerate a mesh after the addition of a vortex generator to the CAD model, which is a time consuming operation, especially on complete configuration studies. Therefore, much research has been focused on the development of empirical models of the effects of vortex generators on the mean flow, such as the work of Wendt and Hingst [1994], Wendt and Reichert [1996], May [2001], and Jirasek [2004]. Instead of physically meshing each vortex generator, a secondary flow perturbation is placed at the desired location of the vortex generator.

These flow perturbation models rely on the ability of the computational engineer to properly choose the vortex strength, with no guarantee beyond experience that the choice is correct. While these methods may produce acceptable 'quick-fix' solutions, there is no assurance that the proper flow physics are actually captured. In addition, the results can be highly dependent on both the computational grid and the turbulence model used in the RANS codes in which the vortex model is utilized.

This dependency on the form of the turbulence model is not limited to empirical models. RANS closure models have been developed over several decades, with most based upon studies of 2D turbulent boundary layers and the assumption of isotropic turbulence. As such, these models generally fail to predict the preferred directions of 3D turbulent boundary layers, especially near the wall. This has led to a shift towards calculating more of the large scale turbulence structures and relying less on RANS turbulence models, as embodied by the LES

technique. While LES methods have shown much promise, such as the study of You et al. [2006], and hybrid RANS/LES methods such as Detached Eddy Simulation are now becoming more common, the computations are still costly for large scale simulations. Therefore, RANS calculations still dominate practical applications, mainly due to their low cost in terms of time and computing resources. However, many RANS codes are coupled to closure models which have not been fully validated against a wide range of 3D turbulent boundary layers. This has led to the resurgence of fundamental experimental testing in order to provide proper validation information to computational engineers, building on the work of Oberkampf and Aeschliman [1992].

Over the past several decades, numerous experimental studies, such as those of Mehta et al. [1983], Cutler and Bradshaw [1986], Bragg and Gregorek [1987], Pauley and Eaton [1987], Cutler and Bradshaw [1989], Pauley and Eaton [1989], Wendt et al. [1993], and Kuhl [2001], have been performed in order to not only qualitatively understand the flow structure created by individual, paired, and arrays of vortex generators, but to also quantify their effects. However, most of these studies were performed using invasive techniques, such as hot wires and Pitot probes, which are generally not capable of simultaneously measuring all three velocity components near a boundary. With the advent and refinement of the laser Doppler and particle image velocimetry (LDV and PIV) techniques, non-invasive measurements are now possible, allowing for more accurate and detailed validation data.

1.3 Current Work

For the current study, two half delta wing vortex generators were mounted inside the Virginia Tech Small Boundary Layer Wind Tunnel, as show in Figure 1.3.1. This creates a

simple geometry that is well suited for computational studies. The Comprehensive Laser Doppler Velocimeter (CompLDV), developed at Virginia Tech, was used to obtain detailed flow field measurement at two planes downstream of the vortex generators and normal to the flow direction.

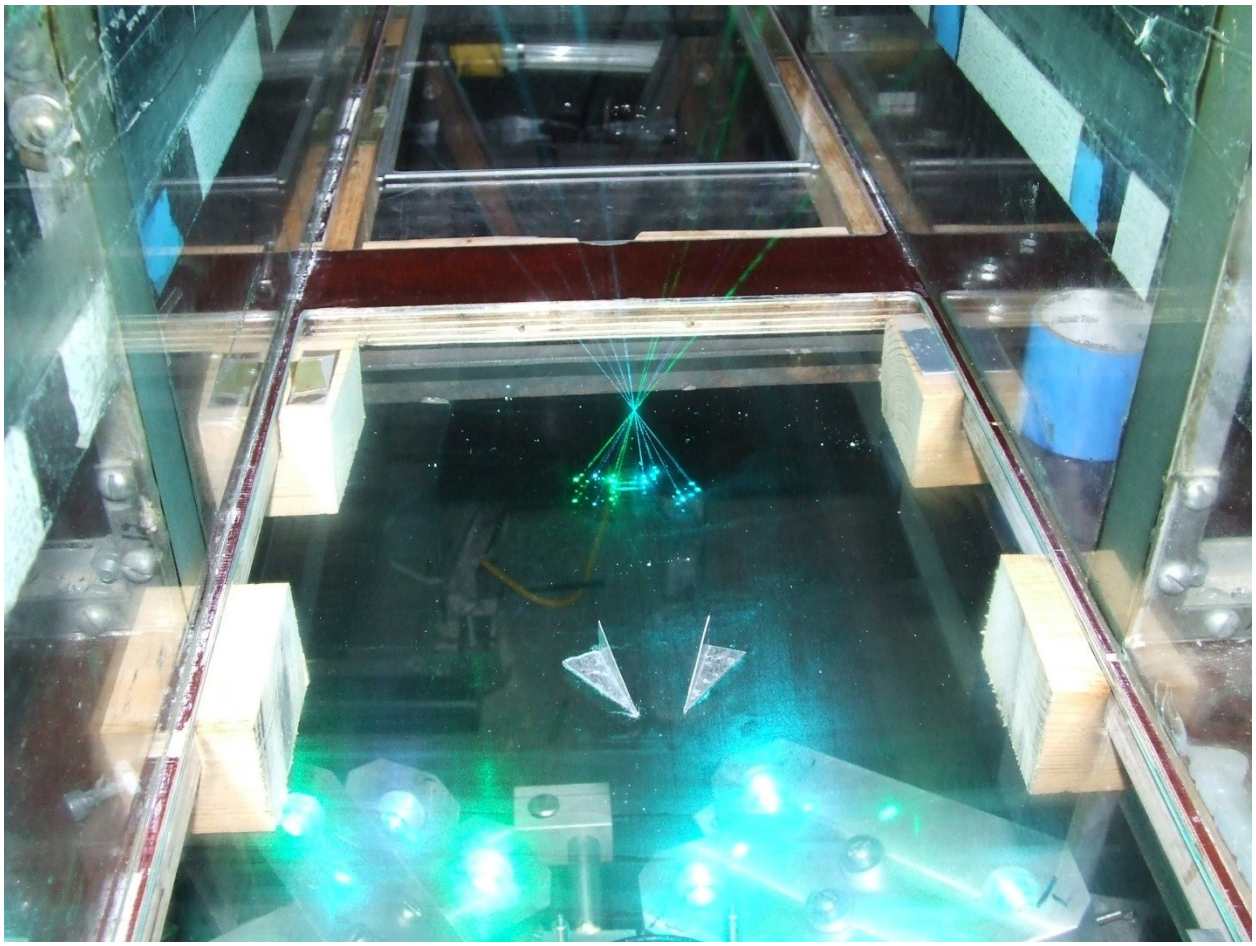

Figure 1.3.1 Vortex Generators, in situ, with launched CompLDV beams

1.4 Thesis Outline

This thesis is organized as follows. Chapter two contains a detailed discussion of the experimental apparatus utilized during the study, as well as data acquisition and processing techniques. Chapter three presents the experimental results and discussion, and chapter four

offers conclusions. Appendices include data not otherwise discussed in the body of the text.

Chapter 2. Experimental Apparatus and Principles

2.1 Introduction

This chapter discusses the facilities and experimental apparatus utilized in this study, including the data acquisition system and processing paradigms.

2.2 Wind Tunnel

All tests were performed in the Virginia Tech Small Boundary Layer Wind Tunnel, Figure 2.2.1, which is described in detail by Bennington [2004]. This closed return tunnel has a test section roughly 200 cm in length, 24 cm in width, and 10 cm in height. The flow was tripped at the contraction exit by a 0.125 inch square bar and a second bar 2.0 inches downstream of the first, both of which span the tunnel test section. A piece of 20-grit silicon-carbide sand paper is placed between the square bars, as used by Varano [2010] and Hopkins [2010]. As has been previously reported by Bennington [1994], there is an approximately 6 cm width on either side of the centerline where the boundary layer on the sidewalls does not affect the mean flow at the approximate location of the 44.5 cm measurement plane. All measurements were taken within 5 cm of the centerline to stay within this region and to avoid clipping of the outer laser beams by the tunnel structure.

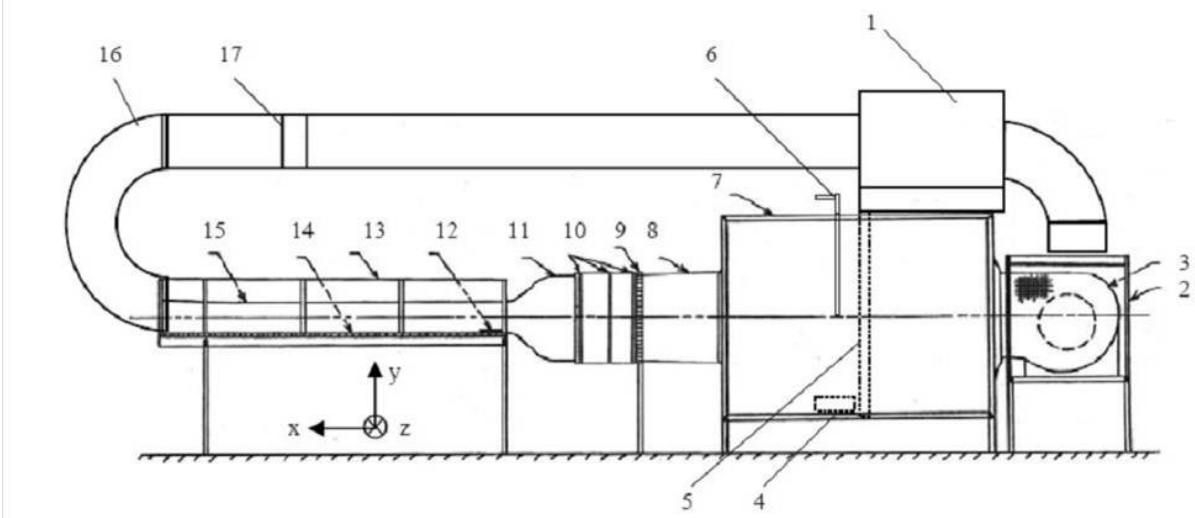

1. Air Conditioner
2. Filter Box
3. Blower
4. Drip Pan
5. Baffle Plate
6. Seeding Pipe
7. Plenum Chamber
8. Contraction
9. Honeycomb
10. Screens
11. Contraction
12. Trip Arrangement
13. Glass Side Walls
14. Bottom Wall
15. Top Wall
16. Return Ducting
17. Rubber Joint

Figure 2.2.1 Virginia Tech Boundary Layer Wind Tunnel Schematic, from Bennington [2004]. Used under fair use, 2012.

The tunnel is powered by a 2.5 hp centrifugal blower and flow speed is mainly controlled by a butterfly valve located in the ductwork upstream of the blower. The tunnel roof is an adjustable panel made of 0.375 inch Plexiglas and provides secondary control of the tunnel speed via its adjustment points. That is, the roof can be adjusted to set the pressure gradient. Ports are located in the roof to allow for Pitot probe access in order to check the pressure gradient. One port is reserved for a thermometer, sealed to the tunnel, for monitoring temperature during test runs. For the tests conducted for this study, the free-stream velocity was set to a nominal speed

of 21.1 m/s, as shown by Figure 2.2.2, with a zero, to slightly favorable, pressure gradient. A hatch is located approximately 120 cm downstream of the contraction exit and is primarily used to access the tunnel for cleaning. The roof and access hatch are sealed using plastic tape whenever the tunnel is operated.

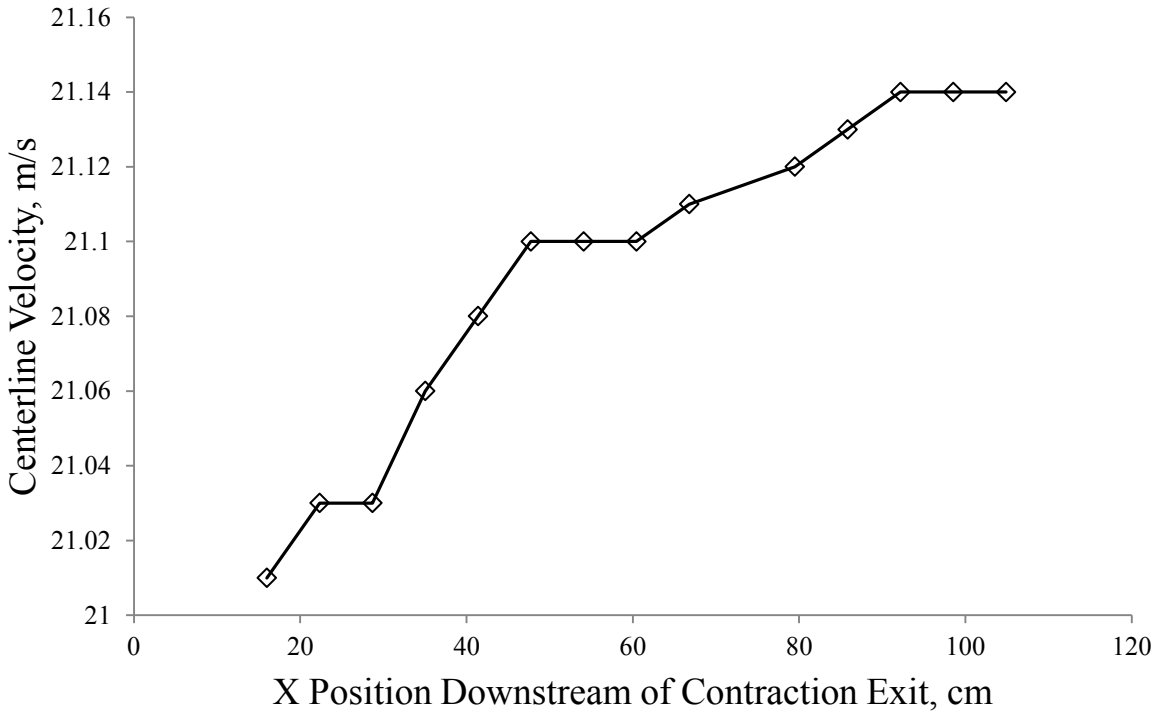

Figure 2.2.2 Velocity Profile along Wind Tunnel Centerline

For this work, the entire floor of the tunnel was retrofitted with glass viewing panels for full CompLDV access, and this configuration was retained for the work of Varano [2010] and Hopkins [2010]. 3M Scotch Magic Tape was used to seal the glass panels to the tunnel structure in order to completely seal the test section.

2.3 Flow Seeding

Seeding consisted of aerosolized dioctyl phthalate (DOP) created by passing compressed air through Laskin nozzles submerged in a liquid DOP bath, as developed by Echols and Young [1963]. Atomized particles are then passed to a collecting chamber before being passed through a VAPCON system, which was developed by Liu et al. [1966], in order to control particle size.

In order for a LDV system to produce accurate results, the particle size must be carefully controlled, as too large a particle will not properly follow the flow field. It has been shown in Lehmann et al. [2002] that the departure of the seed velocity from the flow velocity can be modeled by:

$$\tau = \frac{d_p^2\left(\rho_p + \frac{1}{2}\rho_f\right)}{18\mu}$$

where the time constant, τ, depends on the densities of the fluid, ρ_f, and particle, ρ_p, as well as the fluid viscosity and particle diameter. As long as τ is less than the Kolmogorov time scale, the particle will follow the flow well.

This constraint on maximum particle size is balanced by the practical consideration that too small a particle will not scatter enough light. Therefore, a balance must be reached between flow tracking by the particle and maximization of light scatter. The temperature of the VAPCON is therefore adjusted to create a particle size that balances these parameters.

The first halves of the four steel tubes that create the VAPCON manifold are wrapped in heating elements that are set to hold a temperature of approximately 770° F. The high temperature causes the DOP to vaporize at the top of the manifold and then condense at the

bottom of the manifold into nearly ideal 0.61±0.07 micron particles, as found by Lowe [2006], before being introduced into the wind tunnel. The amount of seed is adjusted by changing the pressure of the compressed air flowing through the Laskin nozzles, with care being taken not to introduce too much seed at the expense of dual bursts, or too little seed which can create a low data rate. The proper amount of seed particles is found through trial and error, as there is no direct way to measure the seeding density within the tunnel.

Due to the high heat generated by the VAPCON system, the wind tunnel is equipped with an integral air conditioning system. This system maintained the air temperature within the tunnel to within ±0.5 K of a baseline temperature recorded at the start of each profile acquisition, and frequently checked during data acquisition.

2.4 Vortex Generators

The 22 gauge sheet metal, half delta-wing, vortex generators used in this study have a chord of 2.5 cm and height of 1.0 cm, mounted at 18° to the tunnel centerline and 0.8 chord length apart at mid chord. This is the same geometry studied by Kuhl [2001], and is modeled on the work of Pauley and Eaton [1987]. The leading edge of the vortex generators were located 50 cm downstream of the contraction exit. In order to maximize the range of access for the CompLDV, the vortex generators were mounted directly to a glass floor plate, Figure 2.4.1. The coordinate system used in this study is shown schematically in Figure 2.4.2.

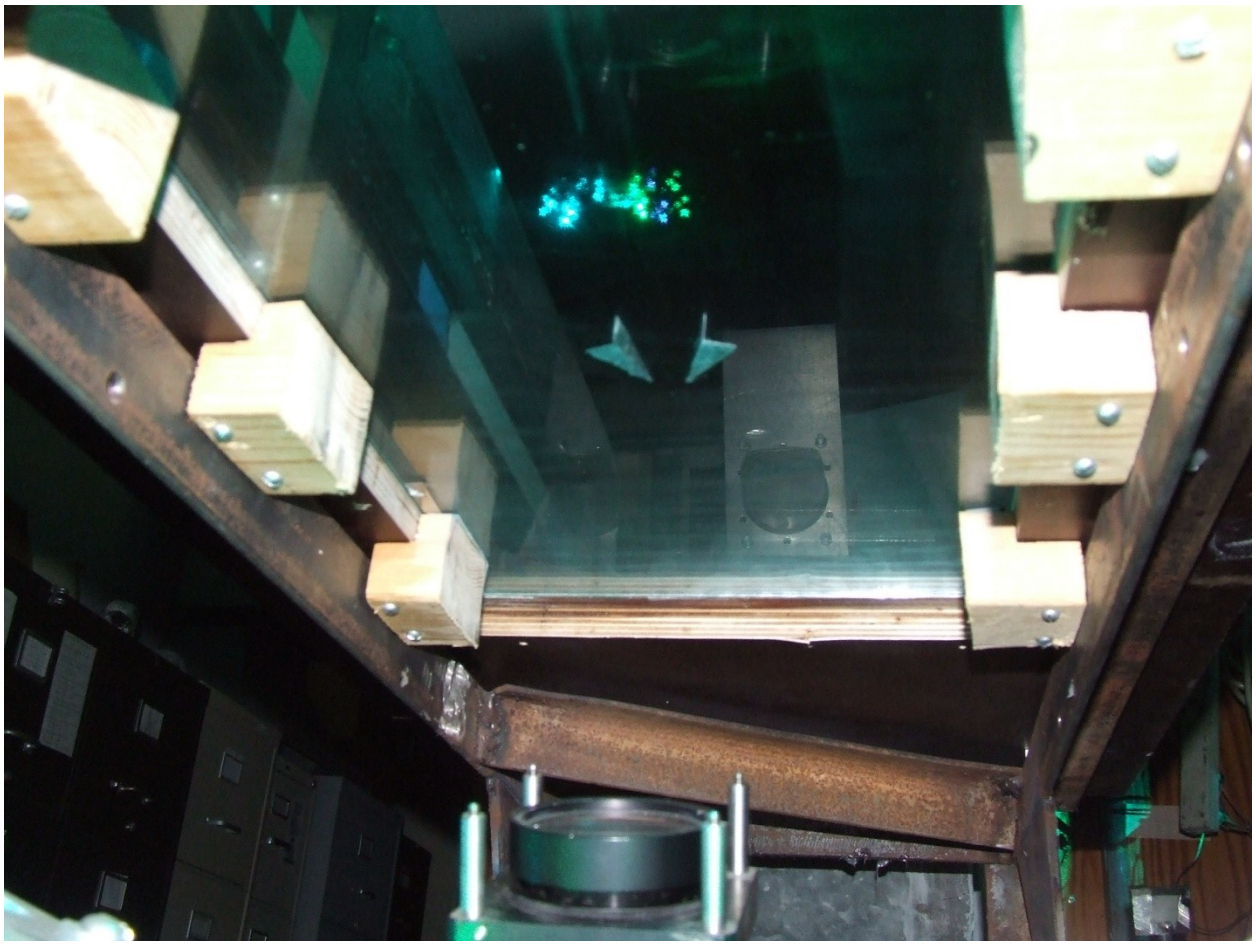

Figure 2.4.1 Vortex Generators Mounted on Floor

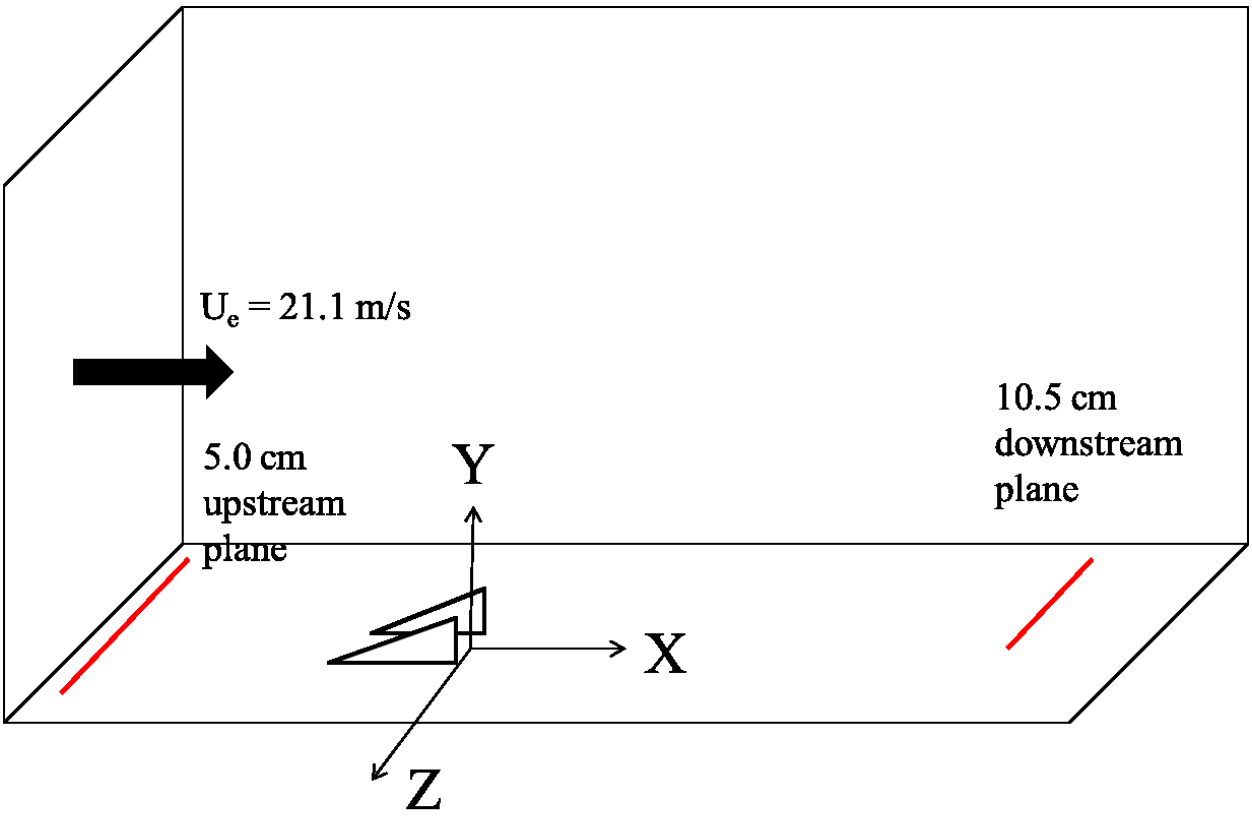

Figure 2.4.2 Vortex Generator Schematic Showing Coordinate System

2.5 Inflow Examination.

Several boundary layer profiles were obtained 5 cm upstream from the leading edge of the vortex generators at z = -2.5, 0.0, and 2.5 cm for inflow information. It was found that the inflow boundary layer is nearly two-dimensional, with an average Re_θ = 3500 and edge velocity of 21.1 m/s. The inflow profile for z = 0.0 cm is shown in Figure 2.5.1. Kuhl's work had an average Re_θ = 1100 and edge velocity of approximately 12.9 m/s. This was calculated by a fit of a modified Spalding Equation, as used by Madden [1997], to the data as not enough near wall data was available due to flare from seed buildup on the wall. This upstream measurement location could not be easily reached for cleaning as it was not possible to avoid the possibility of

damaging the vortex generators or disturbing the alignment of the probe.

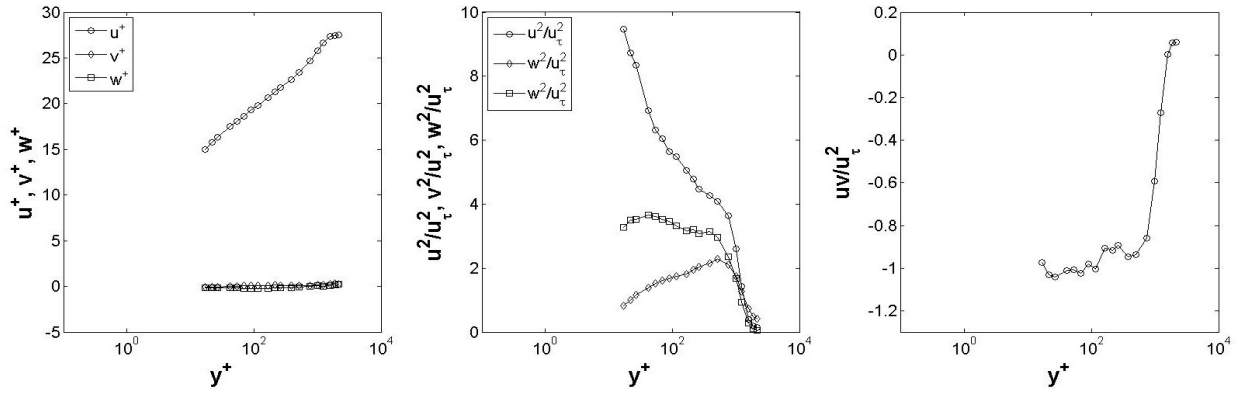

Figure 2.5.1 Non-dimensionalized Inflow Boundary Layer Profile at Tunnel Centerline

In Lin's study, a maximum vortex generator to inflow boundary layer height ratio, h/δ, of 0.5 is suggested as the balance point between vortex generator efficiency and increased parasite drag. For this study, the h/δ ratio is approximately 0.31, based on a boundary layer thickness definition of 99% U_e, while the h/δ ratio of Kuhl's study is approximately 0.65.

2.6 Flow field symmetry

Before measurements began in full, a vortex symmetry study was conducted. In order to quickly determine if the vortex generators had been placed correctly, a flow visualization using a titanium dioxide/kerosene mixture was performed, as per the formula of Tian [2006]. As shown by Figure 2.6.1, the vortices left nearly symmetric streak lines behind the vortex generators, implying nearly equal vortex strength.

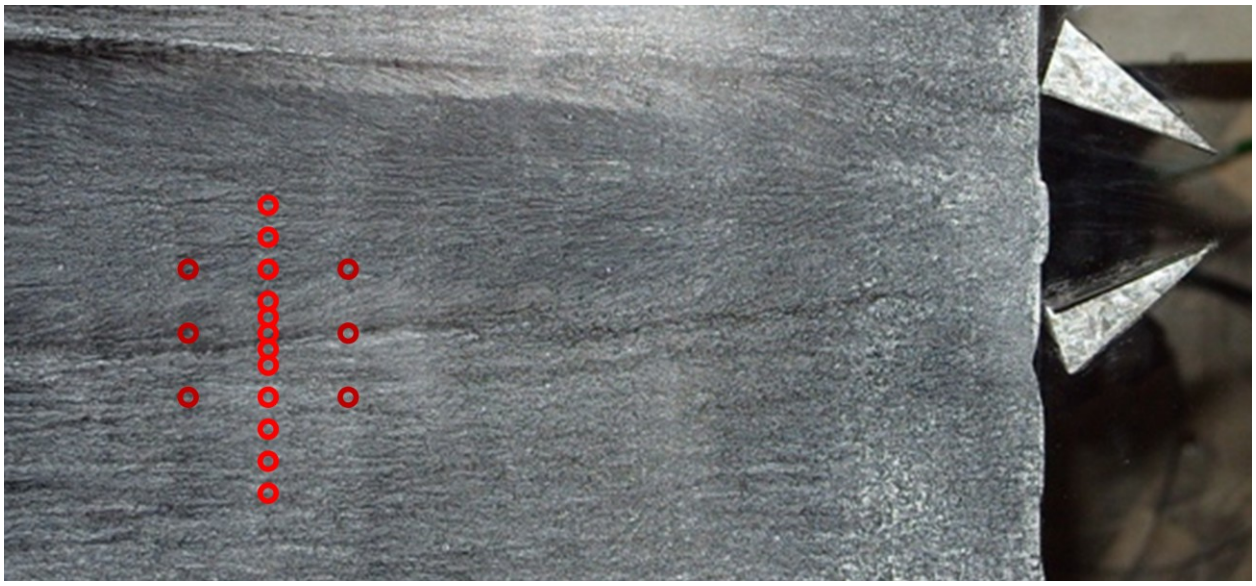

Figure 2.6.1 Flow Visualization with Approximate 10.5 cm Plane Measurement Locations

In order to verify that the vortices were nearly identical in strength , the CompLDV was traversed at a location 10.5 cm downstream of the vortex generator trailing edge and 0.75 cm from the wall from z = -2.5 to z = 2.5 cm in half centimeter increments. Figure 2.6.2 demonstrates that the vortices have nearly equal strength.

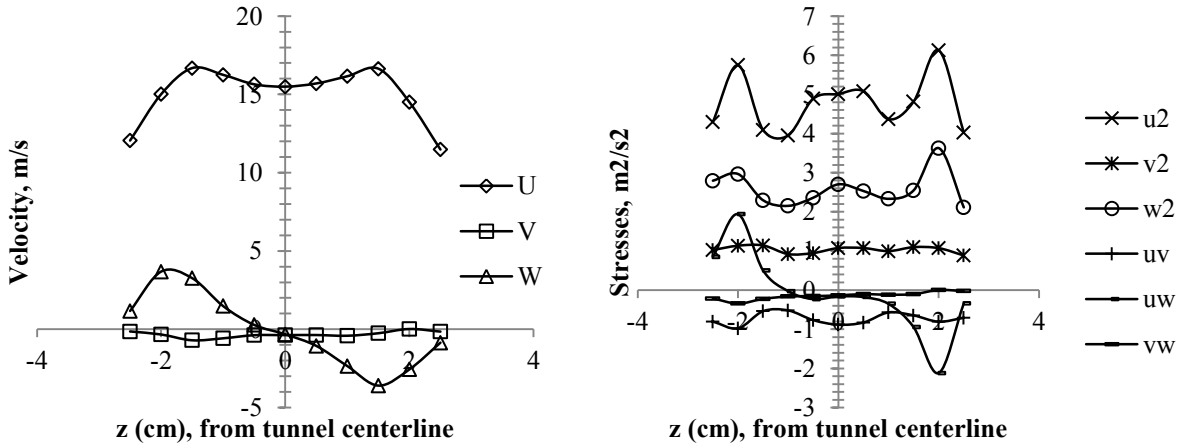

Figure 2.6.2 Symmetry Study at x = 10.5 cm, y = 0.75 cm

2.7 Measurement locations

Due to the results of the symmetry study, measurements were only obtained in the negative z direction, which is closest to the optics table. In order to compare the current results to the work of Kuhl, similar measurement planes were used at x = 10.5 cm and 44.5 cm downstream of the trailing edge of the vortex generators.

Approximately 20, logarithmically spaced, data points were recorded between y ≈ 0.3 mm and y ≈ 52.1 mm. In addition, two to three data points were taken below y = 300 microns in order to determine the wall location. These points were often partially submerged in the wall and aided in wall finding, as will be discussed in Section 2.14.

2.8 Comprehensive LDV System

This section will discuss the operating principles behind the Comprehensive LDV as well as the design of the probe itself.

2.8.1 Principles of the Comprehensive LDV

Several researchers, as found in the works of Czarske [2001], Czarske et al. [2002], Bttner and Czarske [2001], Bttner and Czarske [2003], and Bttner and Czarske [2006], have examined the problem of locating a particle's position within a measurement volume but have limited themselves to one position component. This work was expanded upon by Lowe [2006] to simultaneously measure all three position components and all three velocity components. The novel off-waist beam crossing configuration and number of overlapping sub-measurement volumes give the CompLDV its position and acceleration measurement capabilities. However, the basic operating principles of the CompLDV are still built upon traditional, parallel fringe, LDV techniques.

The Doppler equation, Equation 2.8.1, relates the velocity perpendicular to the laser fringes to the product of the fringe spacing, d, and the Doppler frequency, f_D.

$$U_{\perp} = f_D d \tag{2.8.1}$$

If two measurement volumes are crossed and a particle passes through both, then the ratio of the above equation for each beam pair must be equal. While this is trivial for parallel fringes, if two measurement volumes are crossed which have a non-uniform fringe gradient, then the ratio is a dependent on where the particle passes through the measurement volume. Such a system can be created by crossing a beam pair before or after the beam waists, the narrowest diameter of the focused laser beam, so that a set of converging or diverging fringes is developed.

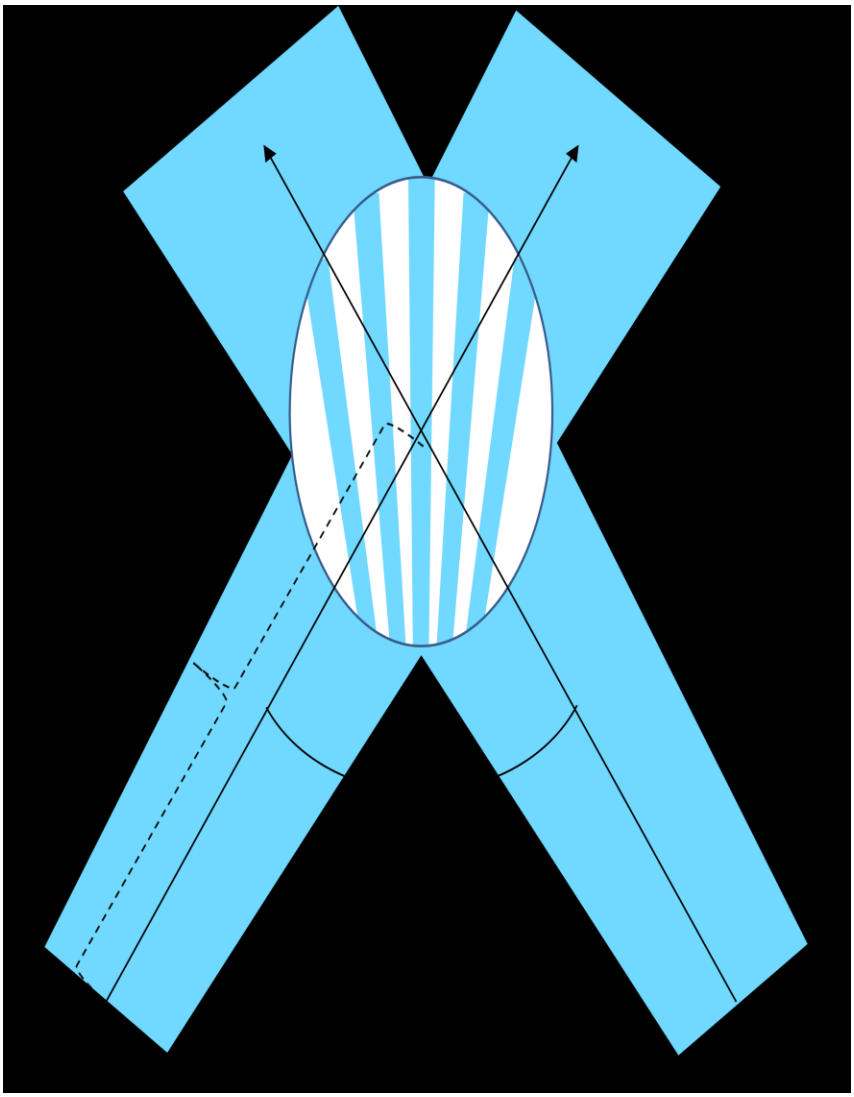

Figure 2.8.1 Schematic of Single Measurement Volume with Diverging Fringes

As long as the beams are crossed at the same location from the waist, and assuming a Gaussian beam intensity distribution, the fringe gradients created in this situation has been shown by Miles [1996] to vary monotonically. This relation is given in Equation 2.8.2, where x' is measured along the beam bisector, θ is the angle between the beams, x'_W is the distance between the waist of the beam and the center of the measurement volume, λ is the wavelength of the light, and $x'_R = \frac{\pi\omega_o^2}{\lambda}$ is the beam Rayleigh number, with the radius of the beam at the waist

defined as ω_0. Figure 2.8.1 shows a schematic of a single measurement volume to help explain the variables in Equation 2.8.2.

$$d(x') = \frac{\lambda}{2\sin\theta}\left(1 + \frac{x'\cos^2\theta\left(x'\cos^2\theta - x'_W\right)}{x'^2_R\cos^2\theta - x'_W\left(x'\cos^2\theta - x'_W\right)}\right) \tag{2.8.2}$$

Using this relationship, along with Equation 2.8.1, it can be shown that the measured Doppler frequency is a monotonic function of the crossing location of each measurement volume the particle passes through. However, each term in Equation 2.8.2 must be determined. As the wavelength of light is known, the waist size is determined by the optics, and the crossing position of the beams is determined based on a desired measurement volume size of 200 μm, the remaining unknown is the beam angles.

Originally, these angles were found by marking points on a piece of paper as the measurement volume was traversed vertically, and then carefully measuring the positions using dial calipers. In order to improve on this technique, the paper is scanned at high resolution, and the angles are determined from the digital version. It was found that this method greatly reduced variations in velocity statistics that were caused by slight fringe gradient imbalances created by the non-digitized method, although calculation of the proper fringe gradients remained a problem for this work.

During post processing the sub-measurement volume velocity distributions were observed to be incorrect. Two partially overlapping measurement volumes would produce vastly different meanflow results at the same sub-measurement volume location. However, the trend in sub-measurement volume velocity distributions was the same for each point in a profile, indicating an error in the fringe gradients. An algorithm was developed where x'_W was treated as

a free parameter for each beam and attempts were made at adjusting the beam crossing distances in order to remove the fringe imbalance, but no satisfactory correction was found. This could be explained by damage, such as burned fiber optics or scratched lenses, within the CompLDV system creating a non-Gaussian beam intensity that would cause Miles' fringe gradient equation to break down. As a result, the instantaneous velocity measurements are in error, and creating large uncertainties in particle accelerations, which require that the fringe gradients be accurately known. However, the time averaged velocity quantities for the whole measurement volume were found to be in agreement with values taken from a small subset at the center of the measurement volume. Due to this, only time averaged results will be presented.

2.8.2 Probe Design and Equipment

Since the initial design, the probe has undergone several revisions. Most visibly, the probe angle was redesigned so that measurements could be made on the tunnel roof for the work of Varano [2010] and Hopkins [2010]. Each beam pair fiber was equipped with a Newport Optics FPR1-C1A three axis traverse for easier alignments when utilizing the projection method of Varano [2010]. Due to this, the y-plane adjusting traverses of Lowe's design were removed and replaced with aluminum channel spacers, greatly reducing the weight of the probe. In addition, a thin laser sheet was mounted such that the sheet intersected the measurement volume normal to the primary flow direction. The redesigned probe head is shown in Figure 2.8.1.

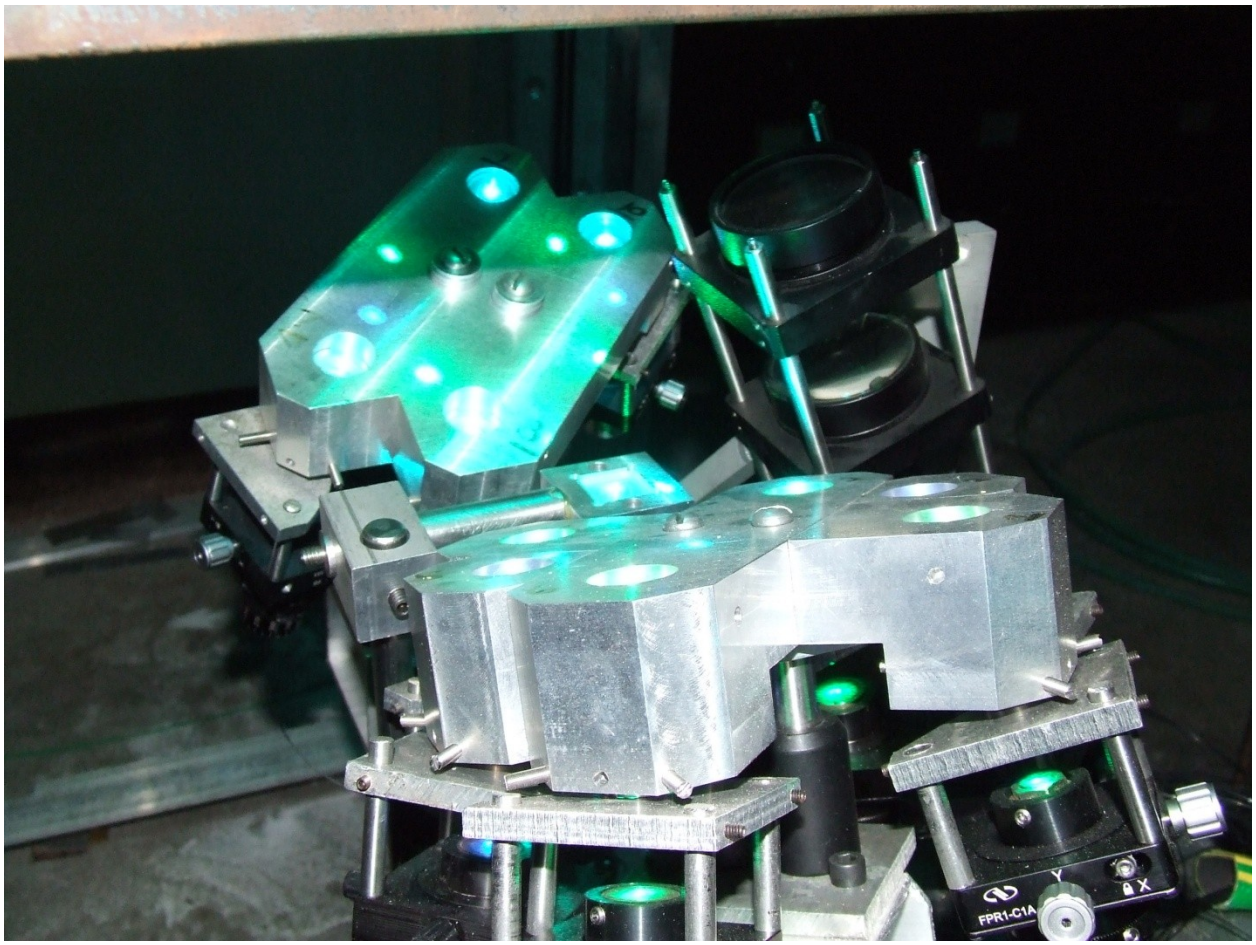

Figure 2.8.1 Redesigned CompLDV probe

Two Coherent INNOVA 90-5C argon-ion lasers supply the necessary laser lines for the CompLDV probe, as shown in Figure 2.8.2. The initial laser output is split into separate wavelengths by prisms. Each color line used to define the measurement volume is then passed through an acousto-optic/Bragg cell which splits and shifts the beam via acoustic beating. Use of the Bragg cells allowed for multiple signals to be combined, or multiplexed, onto a single data channel due to the Bragg frequency operating as a carrier frequency for each Doppler burst. The beams resulting from each split form a pair, each of which are directed to Newport (F-91-C1) fiber couplers and passed through fiber optic cables to the probe head in such a way that coherency is preserved. Each beam pair is then focused at the proper distance in order to form

the converging/diverging fringe patterns necessary for sub-measurement volume position resolution.

Figure 2.8.2 CompLDV Optics Table

The laser sheet does not define the measurement volume, but instead serves as a reference point within the measurement volume. As such, the laser line used for the sheet is not required to pass through a Bragg cell but is instead passed directly to the probe head via fiber optics, collimated, and focused into a sheet which is then aligned with the center of the measurement volume. During data processing, it was found that the position of the laser sheet

was unstable; causing undue rejection of otherwise good bursts Therefore, processing with the laser sheet restriction was removed.

In addition to the laser sheet optics and twelve sets of optics; one for each beam in the measurement volume, the probe head includes the receiving optics which consists of a 5 cm lens system which captures, collimates, and focuses back scattered light from particles passing through the measurement volume onto a receiving fiber. This fiber then passes the light onto a photomultiplier tube (PMT) array, shown in Figure 2.8.3. The light is then separated into its individual laser colors via wavelength specific band-pass filters. Each color band, green, blue, purple, and teal are then focused onto Hammamatsu 5102 PMT's, with the signals amplified by Sonoma Instrument 315 amplifiers powered by Brandenburg Model Series 477 power supplies, and in the case of the teal laser sheet signal, a custom wired Hammamatsu power supply, before being passed to the data acquisition system.

Figure 2.8.3 PMT Array, Amplifiers, and Power Supplies

2.9 Beam Alignment

During initial setup of the probe system, alignment of the crossing beams was accomplished via the projection method of Varano [2010]. The method itself is simple; a sheet of paper is taped to the tunnel floor to act as a viewing plane, and a disassembled beam launcher microscope is used to enlarge the image and project it onto a flat screen.

At a single plane, each beam is focused to its waist, and the position of the probe traverse is then noted as a baseline. Based on the desired size of the measurement volume, as well as

simple geometric relations, the probe is traversed in the y-direction (vertical) to calculated planes and the corresponding beam is focused to its waist. When this has been completed for all ten beams, the probe is returned to the baseline plane. Now, rather than being focused at the waist, each beam is set to the desired measurement volume diameter. The projection method allows for easy viewing of the beams as they are manually overlapped to form the measurement volume using the previously described three-axis beam traverses. Once this procedure is completed, the probe is traversed to make sure that none of the beams move due to hysteresis in the beam traverses. If the alignment passes this step, the final alignment step is a signal check utilizing the DAQ code which is discussed below.

This information is then used to develop the fringe gradient model for the current alignment, as previously discussed in Section 2.8.1. During data processing, a fringe gradient imbalance was found that could not be corrected, and prevented the correct extraction of particle position and acceleration statistics.

2.10 Signal Check

As part of the standard operations for the CompLDV system, the signal strength is checked after each alignment and before each profile is obtained. Before this begins, the beam intensity is manually adjusted on the laser table to ensure that each beam in the pair has nearly equal power. Upon launching the beam, the intensity in the tunnel is maximized by eye and then checked with a power meter. If everything appears to be satisfactory, the wind tunnel can be started and seed introduced. The fast Fourier transform (FFT) feature built into the DAQ code allows for monitoring of the signal-to-noise ratio for each beam pair. If a signal is too weak, the laser intensity is measured between the probe head and the tunnel. In the case of differing

intensity between beams in a pair, an attempt is made to maximize the power at the beam launcher. If this fails to correct the problem, it is an indication that the optics may be dirty or the fibers must be polished.

2.11 Probe Traverse

A three stage traverse, used in conjunction with the probe, was redesigned for lighter weight and smoother operation. It was discovered that the previous traverse design introduced wobble into the system, destabilizing the redesigned probe heads and causing misalignment. By redesigning the traverse with an emphasis on stiffness, and eliminating unnecessary pieces in both the traverse and probe head, the traversed weight was greatly decreased and the probe wobble was essentially eliminated. As such, the time between alignments was increased due to the lessened vibration.

The redesigned traverse allowed for greater range of movement of the probe, and also allowed for positioning both at the front of the tunnel and rear of the tunnel, which the previous traverse did not allow. Each positioning stage consists of a Velmex BiSlide positioner with Superior Electric MO92 series stepper motors controlled by a Velmex, Inc. VP9000 stepper motor controller. An optical encoder, a Metronics Quick-Chek QC-1100, is attached to the y position stage giving height readouts within ±0.5 μm.

2.11 Data Acquisition

Data acquisition was accomplished through an IBM compatible, Pentium 4 PC running Windows XP SP3 utilizing a custom LabView data acquisition (DAQ) code. Previous data acquisition systems relied on PATA hard disk drives, which created a data transfer bottleneck. In order to alleviate this problem, a switch to SATA hard disks was made, which reduced the

wall clock data acquisition times by more than a factor of two. This time savings allowed for several additional benefits including less time for laser drift to affect measurements and minimization of flow property variations during data acquisition.

The DAQ code also controlled the vertical movement of the traverse within ± 3 microns of a designated y height via the RS-232 output of the VP9000 stepper motor controller. This allowed for automated data recording where the acquisition computer could be monitored remotely in case of seeding or signal issues. Photomultiplier tube voltage was recorded via a Strategic Test UF.258 8-bit digitizer sampling at 250 MS/s on two channels. The 256MB of onboard storage allows for a continuous sampling length of 0.54 seconds per channel.In addition, burst arrival time was recorded using the built in clock on a National Instruments 5112 8-bit digitizer. This feature was used to record the initial trigger time for each file sampled using the continuous data acquisition method and each burst trigger time when using the 'good-burst' acquisition method as discussed in Section 2.12.

2.12 Data Acquisition Methodology

The CompLDV DAQ had originally been utilized to record continuous data samples of 0.54 seconds. However, while recording 0.54s of data takes exactly that time, the transfer time from the Strategic-Test card over the PCI-bus to the improved SATA hard disk drive takes approximately twenty-five times longer. This equates to a total data acquisition time of approximate twelve to thirteen seconds for each 0.54s data point. If thirty seconds of data is requested per point in the boundary layer, sixty data files are generated, and total acquisition time is close to thirteen minutes per point. For a ten to fifteen point profile, which is quite sparse, two to three hours is necessary for each test, and close to 200GB of data is stored.

This time delay presents several problems. As time passes, there is a greater chance of temperature wander in the tunnel if there are great changes in ambient temperature. However, for all test results presented, care was taken to ensure that the temperature in the tunnel stayed within ±0.5 K of a baseline temperature value. The same was not true for laboratory conditions, which caused issues with the optics on the laser table. In addition, the lasers used are also dependent on the stability of the water temperature used for cooling, which can vary throughout the day depending upon water usage throughout the building in which the lab facility is located. Gross fluctuations in water temperature were observed to cause great changes in laser power, causing weak Doppler signals.

As such, an alternative data recording technique, known as the 'good-burst' method, was developed in which only a requested number of bursts were recorded. Therefore, if 100,000 raw Doppler bursts are desired at one point and 200,000 at another, these values can be programmed into the LabView DAQ code and the system will automatically record just the data around the burst trigger event, while simultaneously recording the burst arrival time. This cuts out much of the 'noise' signal that occurs between bursts recorded with the continuous method, greatly reducing the amount of memory needed to store the data and reducing the transfer times. On average, only three to four minutes of wall clock time were required to record data for each point, so a twenty point boundary layer profile could be recorded within one to one and a half hours. An added bonus was that only 25 to 35 GB of storage was necessary per profile depending upon how much buffer data was recorded around the burst.

2.13 Data processing

2.13.1 Computer Equipment

Due to the two different data acquisition methods, two widely varying amounts of data needed to be processed. For the 'good-burst' data, processing was accomplished on a desktop PC running an Intel Core 2 Quad at 2.5 GHz with 2 GB of RAM. In order to process the continuous data, the Enterprise supercomputer, formerly located at the Virginia Tech Corporate Research Center, was utilized. This parallel system allowed for the embarrassingly parallel processing of each twelve point continuous profile in less than 24 hours, including data transfer time, as compared to 72+ hours on the processing PC.

2.13.2 Processing Method

Regardless of the type of data acquisition, the processing method was the same. A brief discussion of the processing methods and codes is found below. Additional information can be found in Lowe [2006], Varano [2010], and Hopkins [2010].

- Step One, Frequency Band Selection: Since each Doppler signal is carried by a Bragg cell frequency, it is possible to decompose each burst signal by its five individual Bragg frequencies. A fast Fourier transform (FFT) is performed on one of the raw data files from each measurement volume location and the maximum frequency peaks, and a prescribed bound around them, are automatically selected as corresponding to a band of interest. These frequency bands are then used to create band pass filters so as to limit the scope of the signal processing in later steps.
    - Since a low SNR value may produce misleading results, MATLAB is used to plot the FFT results, in order to ensure that the proper frequency bands have been

selected. If the calculated frequency bands are found to be deficient, the user can then manually update the frequency bands before creating simulated band-pass filters.

- Step Two, Doppler Signal Extraction: With knowledge of each frequency band and the appropriate filters, a trigger data file is created by searching through one of the two data files for acceptable burst signals. The user selects a SNR value to act as a trigger floor, and the arrival times of any burst greater than this floor are flagged. The trigger file is used to search for the corresponding data locations in the second data file. The bursts from both files have their arrival time, frequency content, and signal to noise ratio (SNR) extracted and stored to two corresponding files.
    - This step requires some experience on the part of the user, as too high of a trigger value may reject too many bursts, while too low of a value can result in an excessive amount of noise triggers, which have no corresponding burst in the second data file.
- Step Three, Combine Data: This step simply combines the data files from the previous step and counts the number of raw bursts found as defined by the trigger file.
- Step Four, Frequency Clipping: In order to further reduce the amount of data, the data extracted from the previous step is plotted on frequency vs. SNR axes using MATLAB. This allows the user to further examine the frequency bands determined in Step One and make any corrections that are needed. If corrections are needed, the frequency band file and filters must be corrected, and the data reprocessed from Step Two. If the frequency bands are acceptable, the user then manually removes data that does not appear to correspond to a Doppler burst, i.e. background noise or noise spikes. This is done by

setting a lower SNR bound and maximum and minimum frequency values are selected. Data which falls within the bound of the clipping are then written to a new file.

- Step Five, Velocity and Position Solution: Using the system of equations developed by Lowe [2006], the position and velocity information for each particle passed by Step Four is solved for using a linear solver and written to file. This step depends on the fringe gradient model discussed in Section 2.8.1.
- Step Six, Position and Velocity Clipping: The files created in Step Five are loaded using MATLAB and the y and z position of each particle is plotted on a scatter plot. This position data is then clipped based on where the measurement volume appears to be, and raw U, V, and W velocity histograms, and acceleration histograms, are developed and subsequently clipped at each profile point. Data which passes clipping is then written to file for further processing such as extraction of velocity statistics.

2.14 Glass Cleaning and Wall Finding

In previous studies, the wall location was initially determined by finding the point of maximum flare as the measurement volume was passed through a glass boundary. This occurs when the center of the measurement volume passes through the wall boundary and scatters light off the wall, as well as anything deposited on the wall, such as DOP. The CompLDV has a much larger, approximately 200 micron, measurement volume than most traditional, three-component LDV systems and therefore creates more flare. Due to this, it was difficult to accurately locate the position at which the center of the measurement volume passed through the wind tunnel floor. The larger measurement volume also causes a wider range in which flare overwhelms the PMT's, so that data cannot be obtained near the wall.

In order to address these issues, the floor wall was carefully cleaned before taking data. Ethanol was used in combination with lens tissue to remove DOP buildup without scratching the glass floor. Using the SBench oscilloscope software distributed by Strategic-Test, the amount of flare as the measurement volume passed through the floor was monitored. While even slightly dirty glass would cause flare to completely swamp the PMT's, a properly cleaned floor would produce an almost negligible noise increase in flare between the glass/air interfaces. As such, it was often difficult to determine exactly where the wall was based on the maximum flare location.

During the frequency clipping step of data processing, described above, it was observed that there was a sharp cut-off in the frequency domain that corresponded to when the measurement volume was partially located in the glass wall; an example of this is seen in Figure 2.14.1. The points at which this phenomenon occurred was noted and used to help narrow the y-shift during the determination of the wall friction velocity.

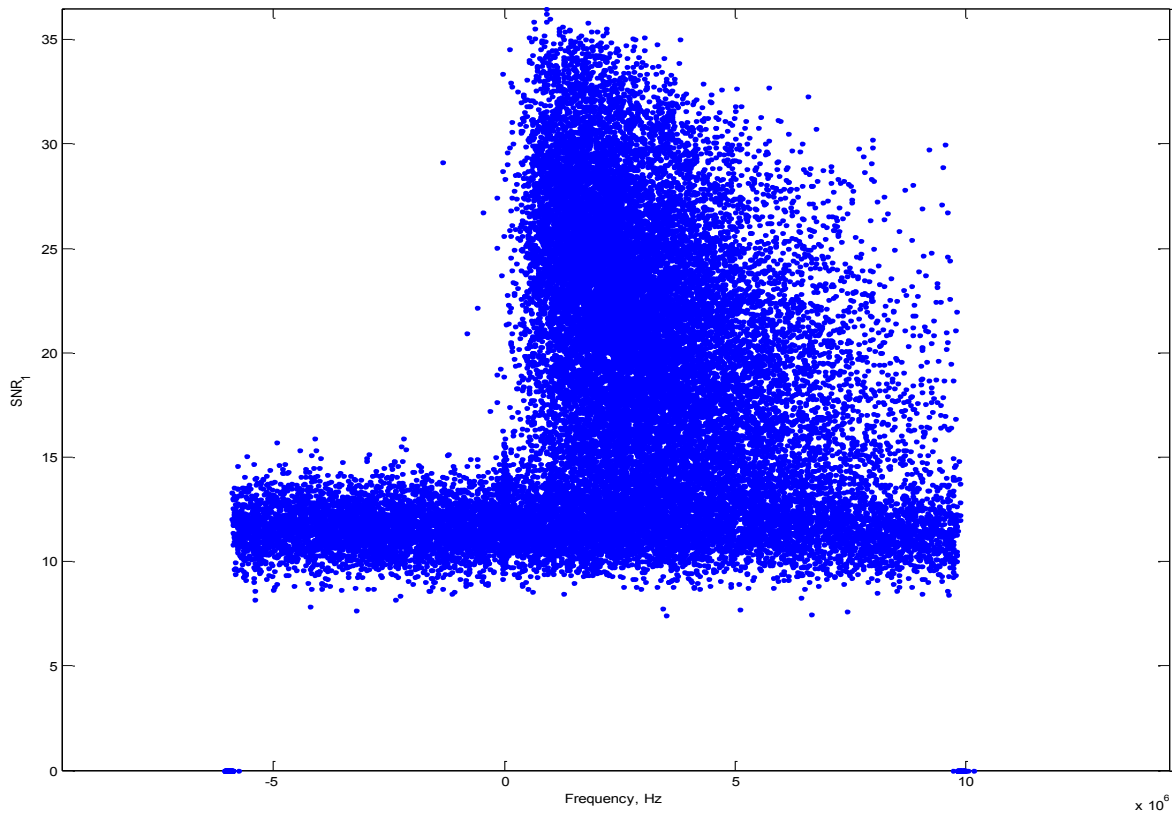

Figure 2.14.1 Example of Frequency Cut-off Due to Presence of Wall

2.15 Uncertainties in Volume Averaged Quantities

Due to the uncertainties in the linear behavior of the fringe gradients, a traditional jitter analysis would result in difficult to quantify uncertainty distribution within the volume. Estimates of uncertainties for volume averaged quantities are based on two profiles obtained at the same locations upstream of the vortex generator on two different days. This method was determined to be the most appropriate method to calculate the volume averaged uncertainties, in light of the fringe gradient problems, including uncertainties in the flow field and probe. These uncertainties are based on 20:1 odds with approximately 50,000 bursts recorded per point. These uncertainties are approximate 1.5x to 2x greater than the uncertainties of Varano [2010] and Hopkins [2010], but this is can be explained by the larger measurement volume of the current study.

$\frac{\delta U}{U_e}$	0.003093	$\frac{\delta\overline{u^3}}{{U_e}^3}$	1.85 x 10^{-5}
$\frac{\delta V}{U_e}$	0.005895	$\frac{\delta\overline{v^3}}{{U_e}^3}$	1.61 x 10^{-5}
$\frac{\delta W}{U_e}$	0.016452	$\frac{\delta\overline{w^3}}{{U_e}^3}$	2.98 x 10^{-5}
$\frac{\delta\overline{u^2}}{{U_e}^2}$	0.001821	$\frac{\delta\overline{u^2v}}{{U_e}^3}$	1.85 x 10^{-5}
$\frac{\delta\overline{v^2}}{{U_e}^2}$	0.000518	$\frac{\delta\overline{u^2w}}{{U_e}^3}$	6.75 x 10^{-5}
$\frac{\delta\overline{w^2}}{{U_e}^2}$	0.001103	$\frac{\delta\overline{uv^2}}{{U_e}^3}$	1.18 x 10^{-5}
$\frac{\delta\overline{uv}}{{U_e}^2}$	0.000512	$\frac{\delta\overline{uw^2}}{{U_e}^3}$	4.41 x 10^{-5}
$\frac{\delta\overline{uw}}{{U_e}^2}$	0.000541	$\frac{\delta\overline{v^2w}}{{U_e}^3}$	3.04 x 10^{-5}
$\frac{\delta\overline{vw}}{{U_e}^2}$	0.000178	$\frac{\delta\overline{vw^2}}{{U_e}^3}$	3.51 x 10^{-5}
		$\frac{\delta\overline{uvw}}{{U_e}^3}$	2.36 x 10^{-5}

Table 2.15.1 Uncertainties in Volume Average Quantities

2.16 Determination of Wall Friction Velocity

Based on the work of Kuhl [2001], the modified Spalding Equation due to Madden [1997] was used to determine the proper y-shift and friction velocity for each profile. A two-step iterative strategy was used to determine the fit. The data was hand-fit to the modified equation to provide an acceptable initial condition and then an iterative solver was used to finalize the best fit. Final results are shown in Section 3.4.

2.17 Difficulties and Suggestions

Lack of control over lab conditions, such as water and air temperature variations introduced to the lab after the original development of the CompLDV, were found to have a detrimental effect on the optical table. Variations in temperature of the water used to cool the ion lasers caused decreases in laser power and enough movement in beam path to cause burned optic fibers. It was found that the water temperature varied with usage throughout the building in which the experiments were conducted, and once normal operating hours were over, laser output became erratic due to the change in load on the water system, especially during colder months.

The optic table was draped by a plastic tent to protect the optics from contamination; however, heat generated by the system was trapped inside, creating a warm steady-state after initial warm up. When the plastic sides were moved, such as during beam launching, this trapped heat would escape and the system would become destabilized. Over time, the system would again reheat and the optics would wander, causing reduced beam power in the tunnel, resulting in a repetition of the process. Under certain circumstances, the beam wandering resulted in burned fibers, causing lost time in order to re-polish or re-terminate the damaged

fiber. This turned out to be an insurmountable problem during the months of January and February as the difference in temperature in the lab and under the tent was severe, and the optics constantly wobbled as a result.

Due to the changes in the layout of the lab, the HVAC system should be reexamined to make sure that it is capable of providing the proper output. It may be possible to install a simple water heater system to address the water temperature issues during cold months and provide a buffer against changes in system usage throughout the building. In addition, temperature controlled mixing valves could be used to provide a constant temperature water supply that is cooler than water supplied by a water heater.

In light of the success of improving the DAQ computer via the upgrade to SATA hdd's, the use of solid state drives should be examined as they become more available. The current PCI Strategic Test A/D converter should also be replaced in the near future with either a newer model with faster and more memory, and/or a newer model with a PCI-Express interface, which will significantly decrease data acquisition times. This would also improve some issues noticed during data processing where noise floors could change between data files. The processing codes would need to be updated to take advantage of a newer DAQ card, but this should be considered anyways due to the frequent occurrence of the processing programs crashing, causing significant lost time in debugging and reprocessing.

Chapter 3. Experimental Results

3.1 Introduction

This chapter contains dimensional, and non-dimensionalized, results for average velocities, Reynolds stresses, turbulent kinectic energy (TKE), and TKE transport at each measurement plane. Reynolds strees and triple product correlations are presented, as well as wall friction velocity and measures of streamwise vorticity and helicity. Full mean flow, Reynolds stress and triple product results at each spanwise location, non-dimensionalized on $y^+ = {u_\tau y}/{\nu}$ and $u_\tau = \sqrt{{\tau_w}/{\rho}}$, can be found in Appendix A.

There were approximately 20 points in each profile, logarithmically spaced between 0.3 mm and 52 mm. In addition, two or three points were taken below 300 microns in order to determine the wall location. The 10.5 cm plane consists of profiles at z = 0.0, -0.5, -1.0, -1.5, -1.75, -2.0, -2.25, -2.5, -3.0, -3.5, -4.0, and -4.5 cm. The 44.5 cm plane consists of profiles at z = 0.0, -1.0, -1.5, -2.0, -2.5, -3.0, -3.5, -4.0, and -4.5 cm.

It is helpful to consider each turbulence quantity as a contour plot to better understand how the vortex generators have affected the flow field. Most every contour plot, except where noted, shows z location in cm as the abscissa and z location in cm as the ordinate. The tunnel centerline location corresponds to z = 0.0 cm, and the triangular areas where data is missing at the top of each figure is due to beam clipping by the vortex generators, in the case of the centerline, and by the tunnel structure, in the region of z = -4.5 cm. Each contour plot was developed using a cubic interpolation of the data within MATLAB in order to be able to properly differentiate the flow field on a regular mesh.

3.2 Results at x = 10.5 cm Plane

3.2.1 Mean Velocities

Figure 3.2.1 demonstrates the characteristic thinning of the boundary layer in the tunnel centerline region due to the effects of the two common flow down vortex cores. This region is apparent in the oil flow visualization, shown in Figure 2.6.1, and is due to the high wall shear stresses in this region, as shown below. At the center of the vortex core lays a nearly vertical line of zero V component velocity. This line corresponds with the demarcation between the high shear stress region near the centerline and the outboard, low shear stress region, also visible in Figure 2.6.1. This line was used in conjunction with Figure 3.2.3 to find the approximate center of the vortex core, estimated to be at z = -1.825 cm at a height of y = 0.80 cm, which corresponds to a y^+ of approximately 550. From these measurements, it is found that the height of the vortex is approximately a quarter of the height of the boundary layer, which is 3.21 cm at this location. Kuhl found that the core of the vortex in that study was located at half the height of the boundary layer at the same location. This discrepancy can be accounted for by the fact that the boundary layer of the previous study was thinner and had a lower edge velocity.

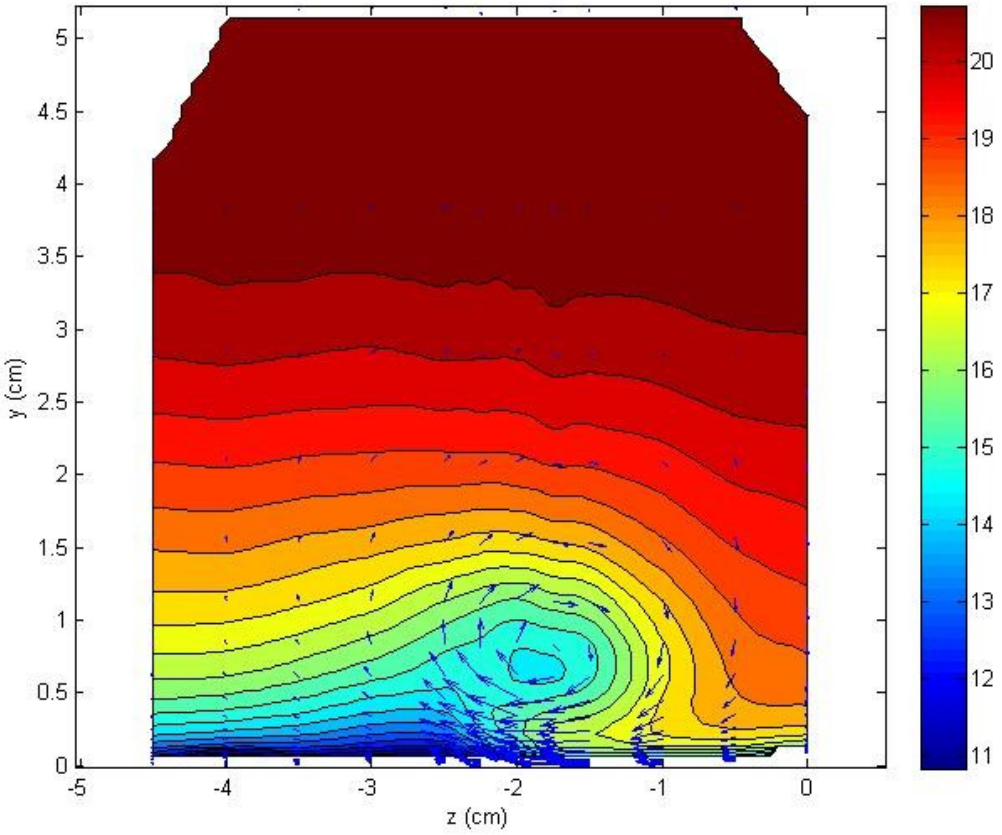

Figure 3.2.1 Dimensional *U*, *m/s*, with overlay of secondary (*VW*) flow vectors

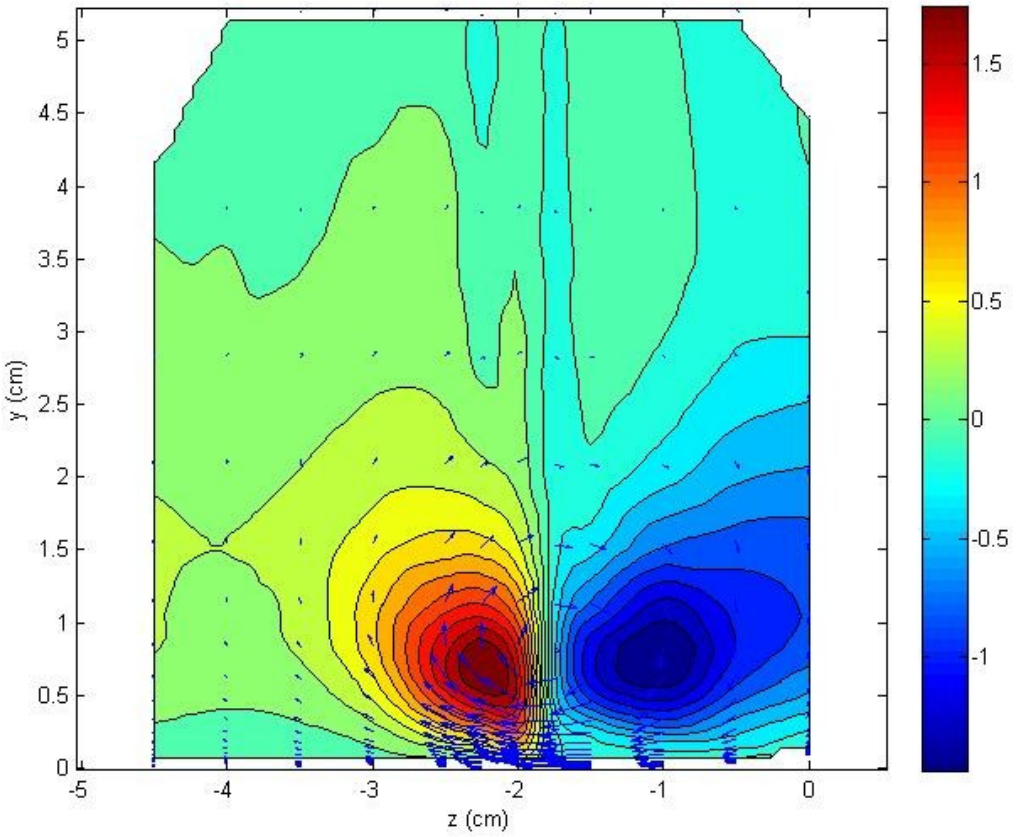

Figure 3.2.2 Dimensional *V*, *m/s*, with overlay of secondary (*VW*) flow vectors

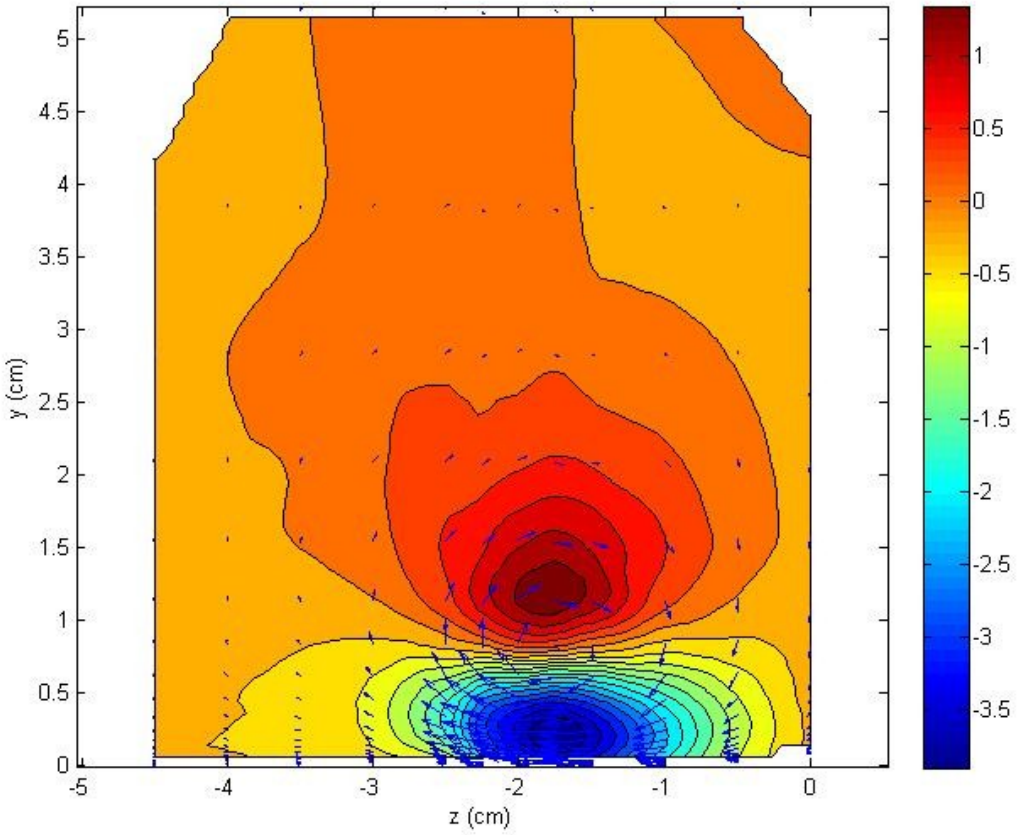

Figure 3.2.3 Dimensional *W*, *m/s*, with overlay of secondary (*VW*) flow vectors

The vortex cores of the current and previous study are at approximately the same physical location, despite the higher circulation of -0.0251 m^2/s compared to Kuhl's -0.0234 m^2/s, implying that the vortex position is only dependent upon the vortex generator geometry. This is shown in side by side comparisons in Figures 3.2.4 and 3.2.5.

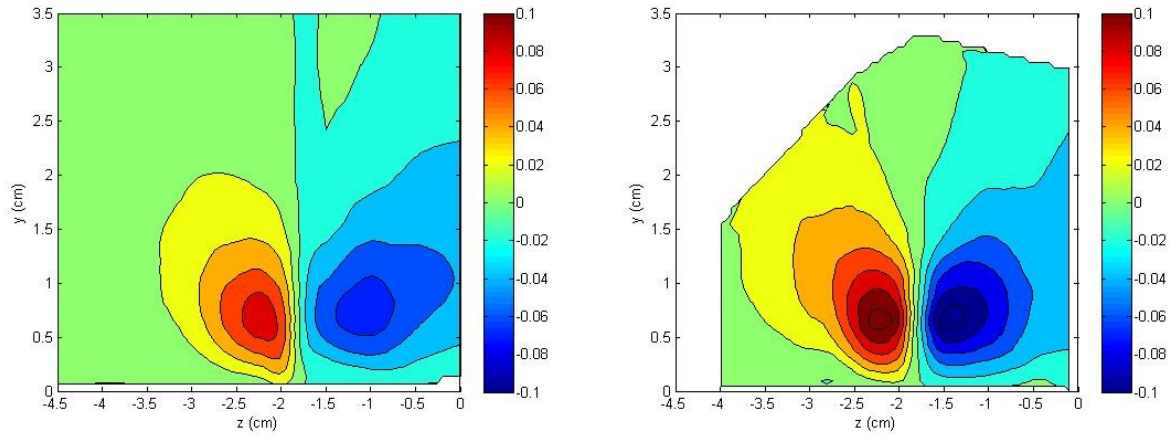

Figure 3.2.4 *V/U*$_e$ for the Current Study (Left) and Kuhl's Study (Right)

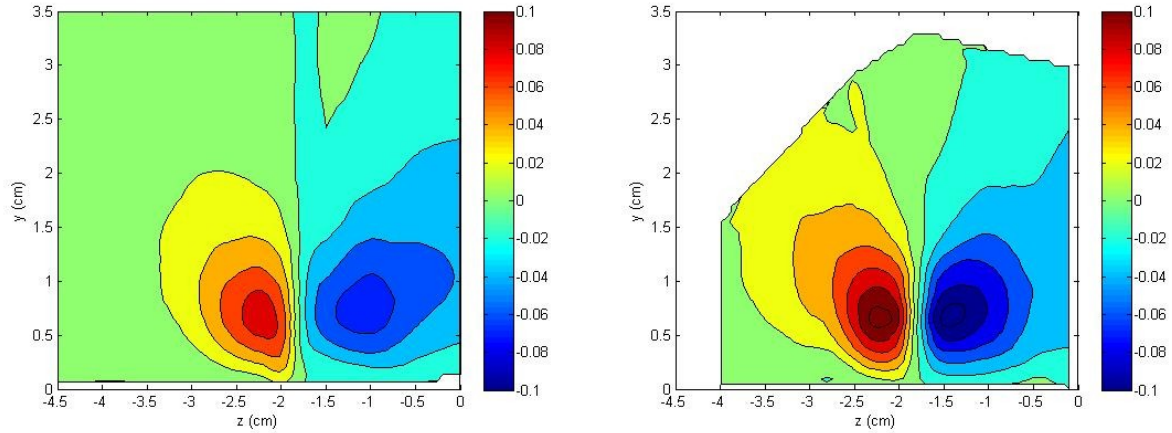

Figure 3.2.5 *W/U*$_e$ for the Current Study (Left) and Kuhl's Study (Right)

Researcher	h (cm)	h/δ	Re_θ	U_h (m/s)	U_h/ U_e	Γ (m^2/s)	C_Γ
Derlaga	1.0	0.31	3500	17.8	0.843	-0.0325	-0.1826
Kuhl	1.0	0.62	1100	8.68	0.668	-0.0234	-0.2696

Table 3.2.1 Comparison of Circulation Information

Table 3.2.1 lists a brief summary of the circulation information for both studies, where U_h is the upstream velocity at a height equal to 1 cm and $C_\Gamma = \frac{\Gamma}{h * U_h}$ is a non-dimensionalized circulation. Using the idealized leading-edge-suction analogy from Polhamus [1968], with the freestream velocity taken to be U_h, the idealized circulation for the current study is -0.0916 m^2/s and for Kuhl's work it is -0.0447 m^2/s. Clearly, the current study has a much lower ratio of true circulation to ideal circulation, but this is most likely due to the boundary layer thickness. The vortex generator in the current study 'sees' a sharper gradient in inflow velocity to height as compared to Kuhl's vortex generator and this would affect the vortex roll-up along the sharp leading edge.

3.2.2 Reynolds Normal Stresses

The normal stresses exhibit similar behavior to that noted by Kuhl. There is a tightly focused peak in $\overline{v^2}$ at the center of the vortex, which seems to indicate the value of $\overline{v^2}$ as an indicator of vorticity, and $\overline{w^2}$ shows a peak at nearly the same location. The $\overline{u^2}$ normal stress shows peaks near the surface, similar to a two-dimensional boundary layer, but shares a peak with $\overline{w^2}$ just outboard of z = -2.0 cm which corresponds with boundary layer thickening shown by Figure 3.2.1.

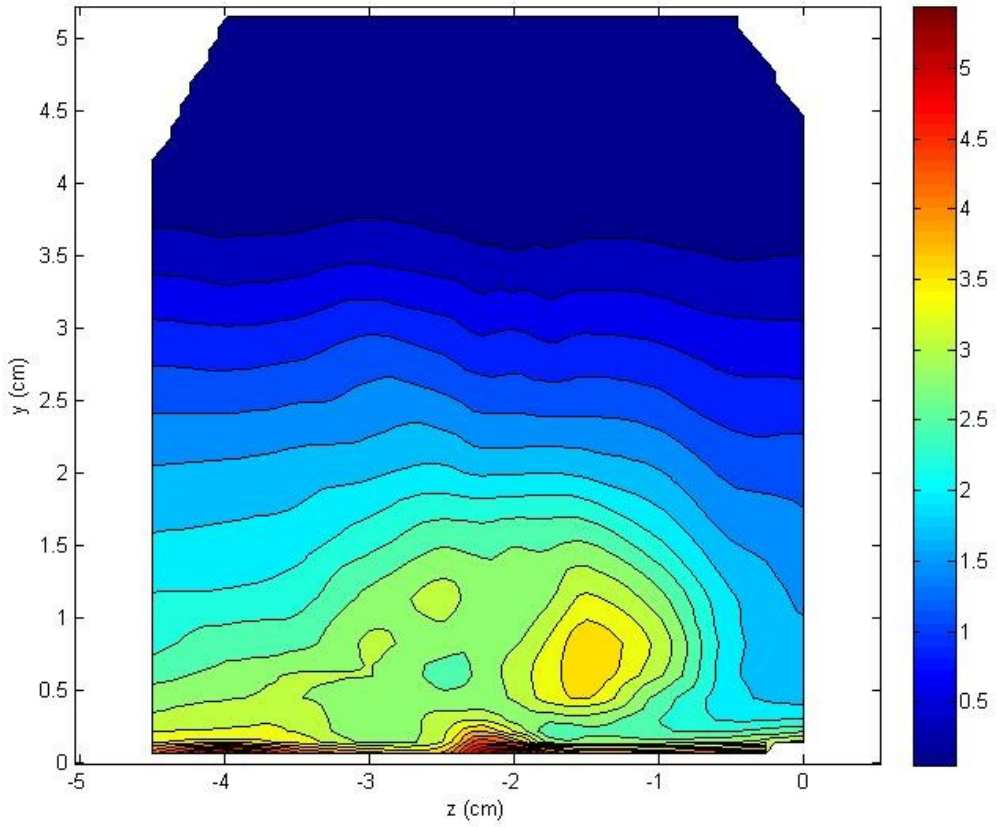

Figure 3.2.6 Mean u^2 normal stress, m^2/s^2

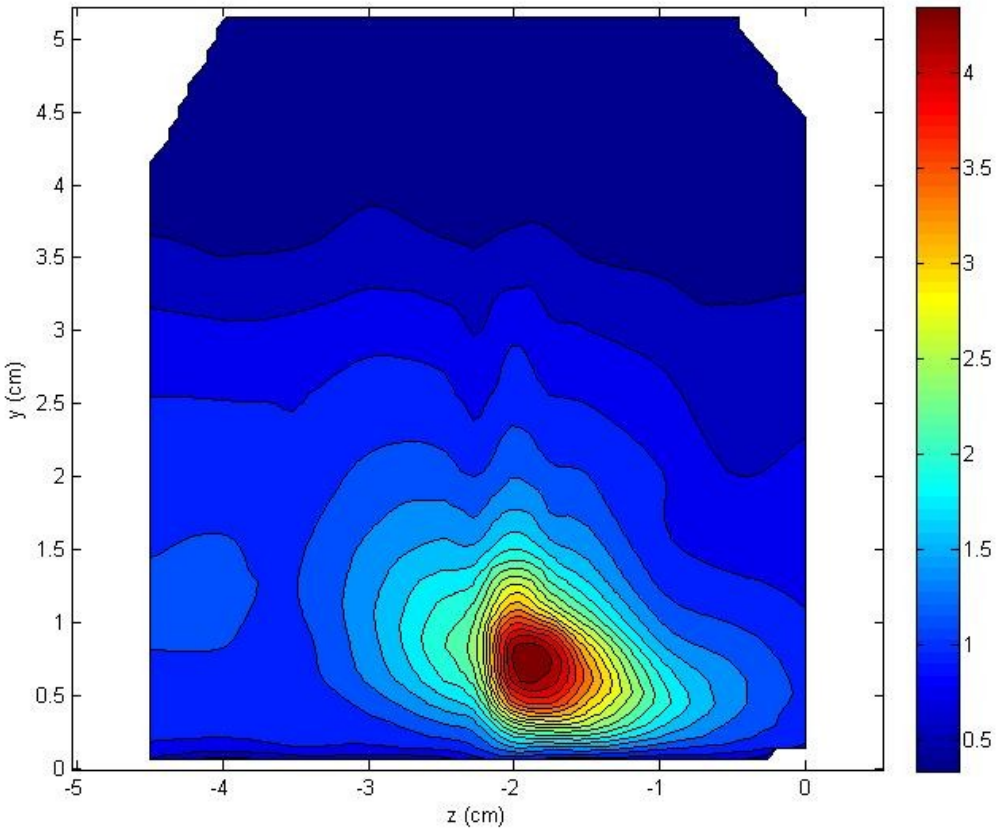

Figure 3.2.7 Mean v^2 normal stress, m^2/s^2

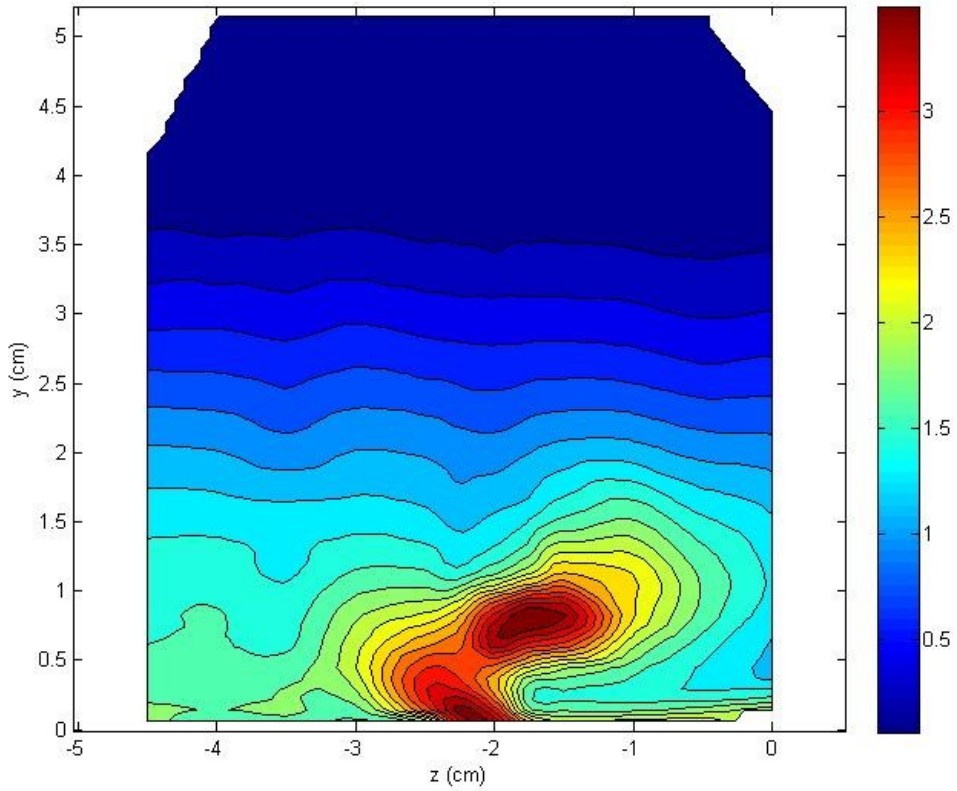

Figure 3.2.8 Mean w^2 normal stress, m^2/s^2

Figures 3.2.9 through 3.2.11 show the normal stresses non-dimensionalized on U_e^2 for direct comparison. It should be noted that the non-dimensional $\overline{v^2}$ is much stronger in the current study, but that the non-dimensional $\overline{w^2}$ is weaker; this can be attributed to the different inflow boundary layers between the studies.

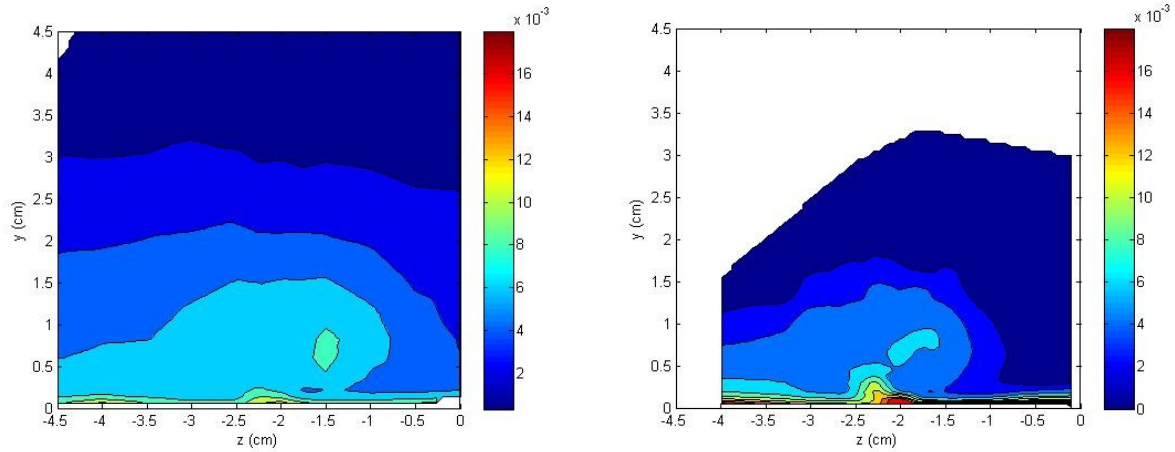

Figure 3.2.9 Non-dimensional mean u^2/U_e^2 normal stress, Current Study (Left) and Kuhl's Study (Right)

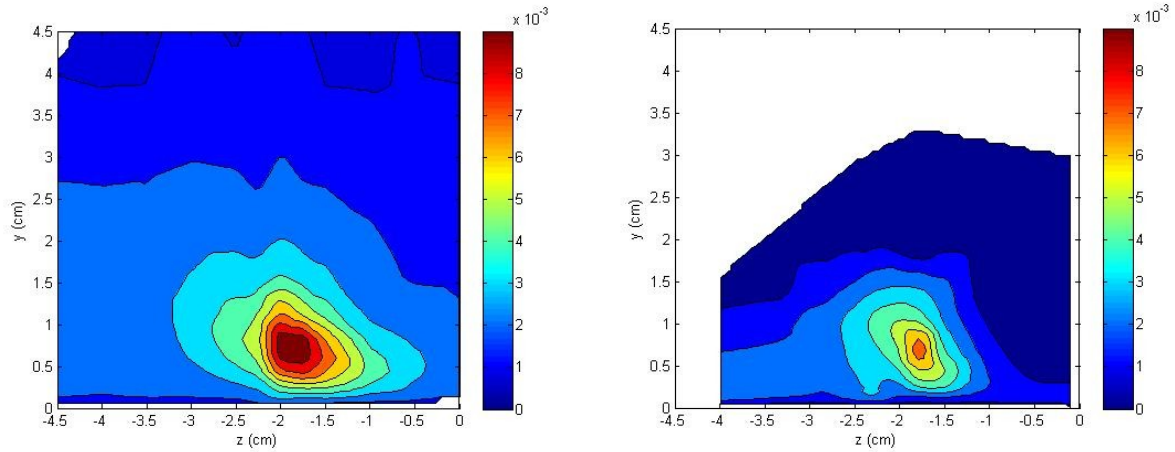

Figure 3.2.10 Non-dimensional mean v^2/U_e^2 normal stress, Current Study (Left) and Kuhl's Study (Right)

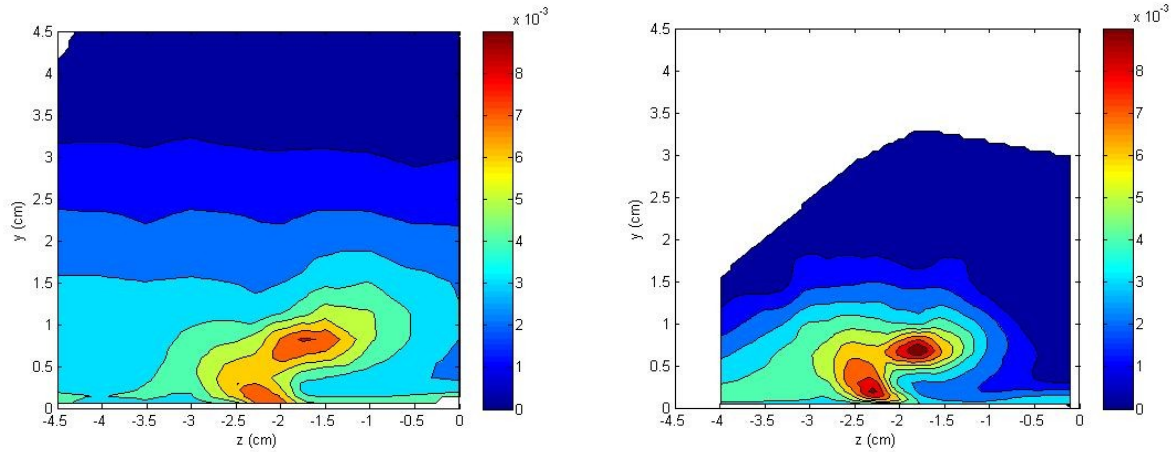

Figure 3.2.11 Non-dimensional mean w^2/U_e^2 normal stress, Current Study (Left) and Kuhl's Study (Right)

3.2.3 Turbulent Kinetic Energy

The turbulent kinetic energy, $TKE = \frac{1}{2}\left(\overline{u^2} + \overline{v^2} + \overline{w^2}\right)$, term shows different behavior than Kuhl's work as seen in Figure 3.2.13, non-dimensionalized on $\boldsymbol{U_e^2}$. While there are peaks in the near wall region for this dataset, the magnitude is not as high in the current study. Instead, peak TKE is shown at the vortex core, which is not surprising considering the vortex strength.

By examining the Reynolds normal stresses, it can be seen that the primary contributor to TKE at the vortex core is the $\overline{v^2}$ term. This implies that the isotropic turbulence assumption of many turbulence models is not a good choice for the non-wall generated turbulent vortex.

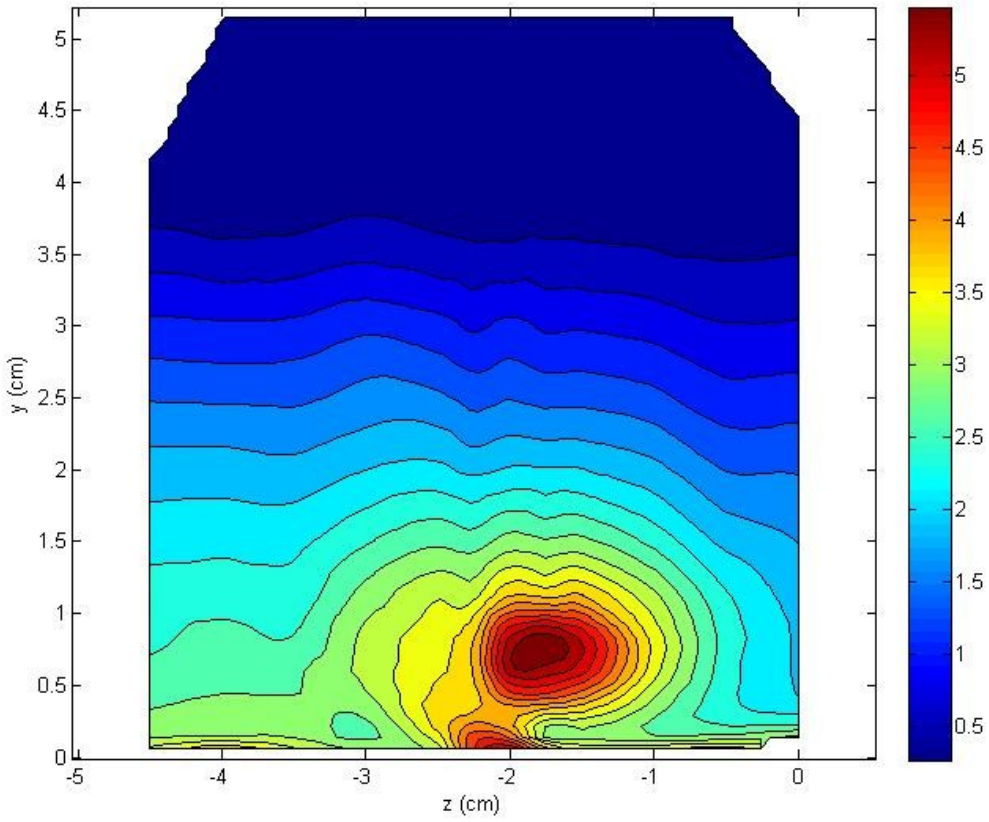

Figure 3.2.12 Dimensional *TKE*, m^2/s^2

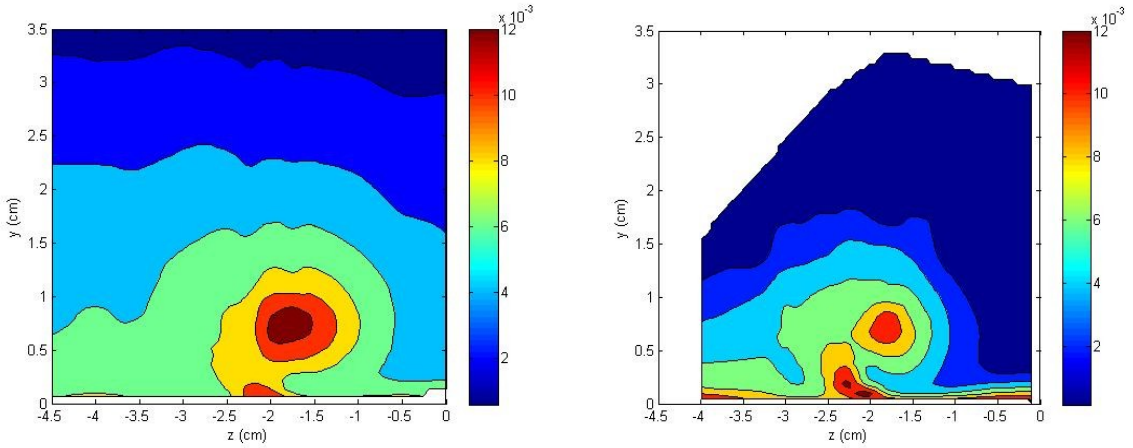

Figure 3.2.13 Non-dimensional *TKE/U_e^2*, Current Study (Left) and Kuhl's Study (Right)

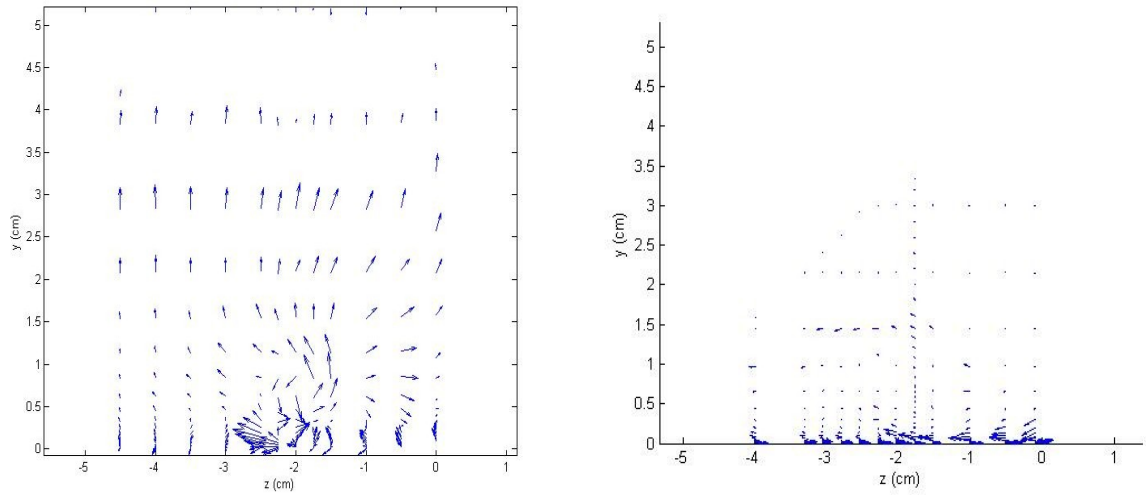

Figure 3.2.14 Dimensional *TKE* transport vectors, *m/s*, Current Study (Left), Kuhl's Study (Right)

The TKE transport vectors, $\left(Trans_{TKE_z}/U_e\right)\vec{j} + \left(Trans_{TKE_y}/U_e\right)\vec{k} = \left(\left(\overline{u^2w} + \overline{v^2w} + \overline{w^3}\right)/(TKE * U_e)\right)\vec{j} + \left(\left(\overline{u^2v} + \overline{vw^2} + \overline{v^3}\right)/(TKE * U_e)\right)\vec{k}$, show jitter, or low frequency, large scale movement, in the flow field. The current study demonstrates significantly higher jitter than Kuhl's study. There is an area of high transport, and therefore high jitter, near z = -2.5 cm not present in Kuhl's work. This is most likely due to the large scale motion of the induced flow

from the vortex as it impinges on, and then moves away from, the wall. This may not have been evident in the previous work due to the difference in vortex strength and stronger, more energetic boundary layer of the current study. It should also be noted that the spreading of TKE through the boundary layer as shown in Figure 3.2.13 can be seen in the vectors of Figure 3.2.14. This may contribute to the breakdown of the vortex as will be seen at the 44.5 cm plane.

3.2.4 Shear Stresses

The $\overline{uv}$ shear stress and $\overline{vw}$ shear stress demonstrate an alternating behavior. In the region roughly below the vortex core, $\overline{uv}$ peaks and is straddled by regions of low $\overline{vw}$, while the reverse is true above the core. As was noted by Kuhl, this study also shows a similar increase in $\overline{vw}$ production near the wall and then spikes near the vortex core due to production and diffusion. Focus should be given to the $\overline{uw}$ stress, as this term indicates the region of boundary layer thickening mentioned above and an area where the vortex has intense interaction with the wall.

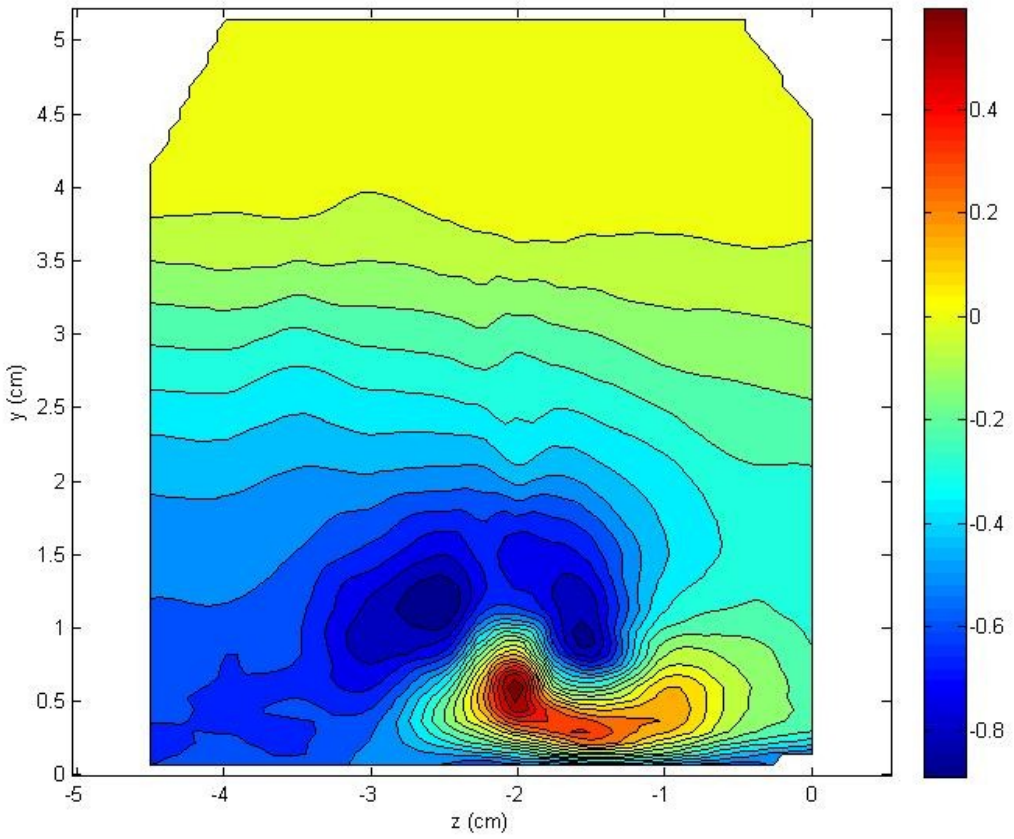

Figure 3.2.15 Mean *uv* shear stress, m^2/s^2

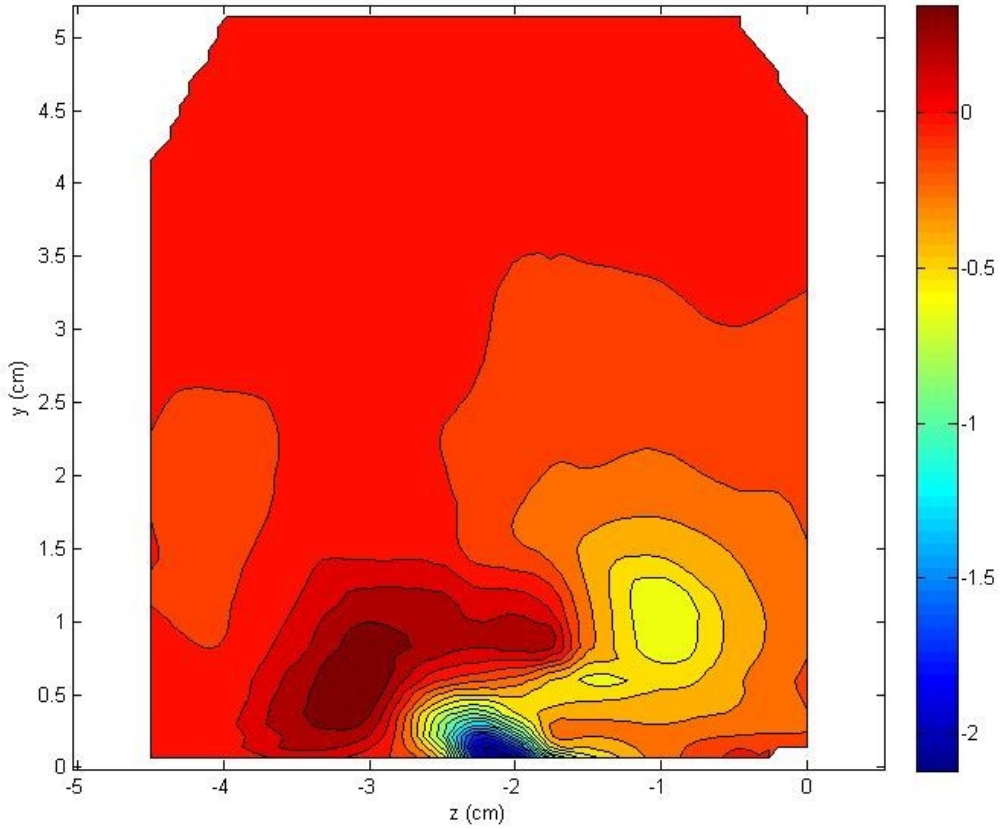

Figure 3.2.16 Mean *uw* shear stress, m^2/s^2

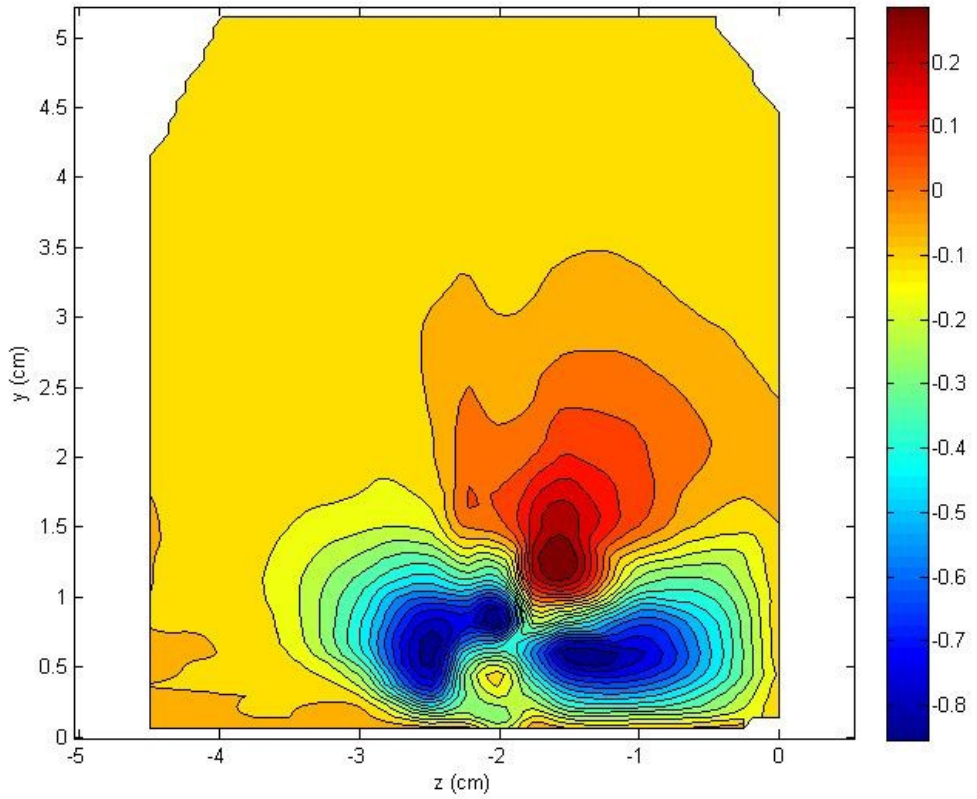

Figure 3.2.17 Mean *vw* shear stress, m^2/s^2

3.2.5 Reynolds Stress Correlations

Several algebraic relationships were used to examine the Reynolds stresses. The parameter $\frac{-\overline{uv}}{\sqrt{\overline{u^2}\overline{v^2}}}$ is shown in Figure 3.2.18. Both the current study and Kuhl's study show similar behavior; a region of negative correlation beneath the core, positive correlation outboard, and zero correlation away from the wall.

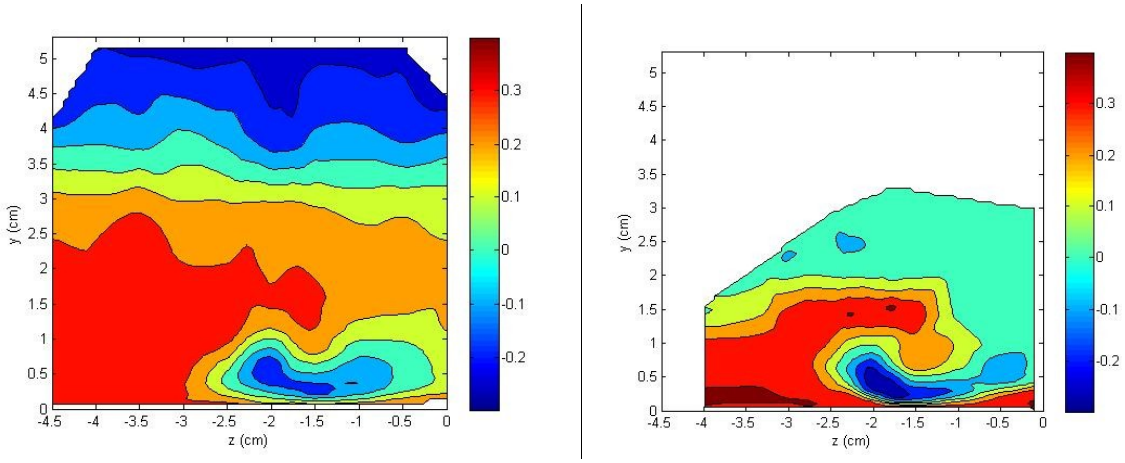

Figure 3.2.18 $\frac{-\overline{uv}}{\sqrt{\overline{u^2}\overline{v^2}}}$ Parameter, Current Study (Left) and Kuhl's Study (Right)

The 1/S parameter, defined by Simpson [1995] to be $1/S = |\tau/\rho| / \overline{v^2}$, is shown in Figure 3.2.19 for the current study and Kuhl's study.

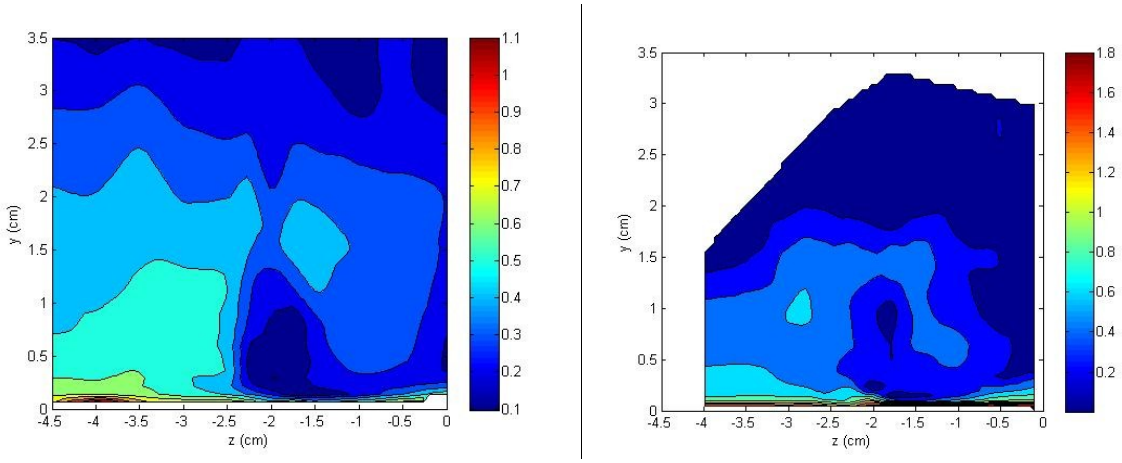

Figure 3.2.19 *1/S* Parameter, Current Study (Left) and Kuhl's Study (Right)

Both studies show a similar behavior, with the parameter reducing to zero with increasing y. Kuhl's work shows a higher peak value, although this is most likely due to better spatial resolution near the wall. In both cases, there are regions of approximately constant 1/S of 0.3 to 0.4 which correspond to the log region.

The three-dimensional parameters derived by Ölçmen and Simpson [1995], and based on the work of Nagano and Tagawa [1990, 1991], are presented below. Figures 3.2.20 through 3.2.22 show each parameter formulated as RHS-LHS; the current study does not show a strong correlation through the boundary layer, although there are some regions in the log layer that demonstrate agreement.

$$I \qquad \frac{\overline{uv^2}}{\overline{v^2}\sqrt{\overline{u^2}}} = \frac{\overline{u^2 v}}{\overline{u^2}\sqrt{\overline{v^2}}}$$

$$II \qquad \frac{\overline{v^3}}{\overline{v^2}^{1.5}} = B\frac{\overline{u^2 v}}{\overline{u^2}\sqrt{\overline{v^2}}} \qquad B = -1.33$$

$$III \qquad \frac{\overline{vw^2}}{\overline{w^2}\sqrt{\overline{v^2}}} = \frac{1}{3}\frac{\overline{u^3}}{\overline{u^2}^{1.5}} + \frac{1}{B}\frac{\overline{v^3}}{\overline{v^2}^{1.5}} - \frac{\overline{uw^2}}{\overline{w^2}\sqrt{\overline{u^2}}}$$

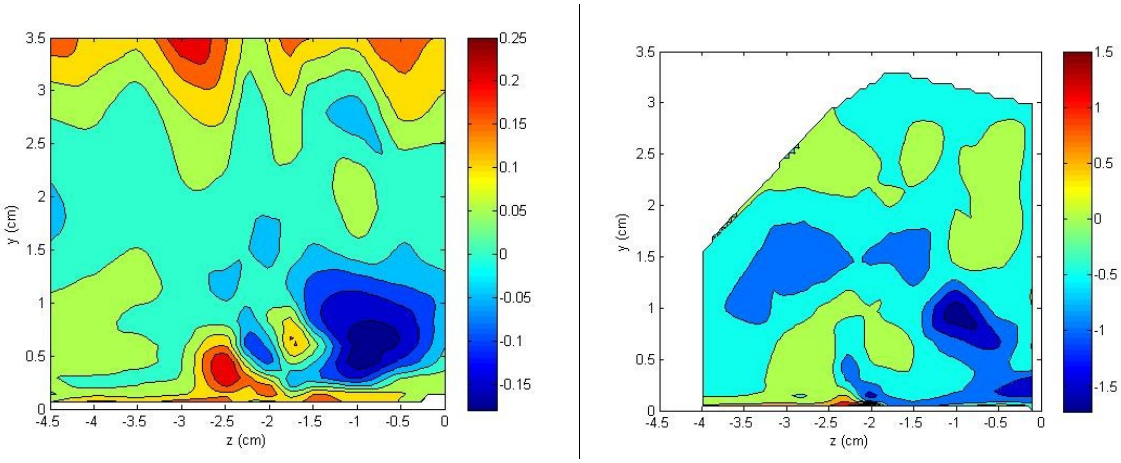

Figure 3.2.20 Parameter *I*, Current Study (Left) and Kuhl's Study (Right)

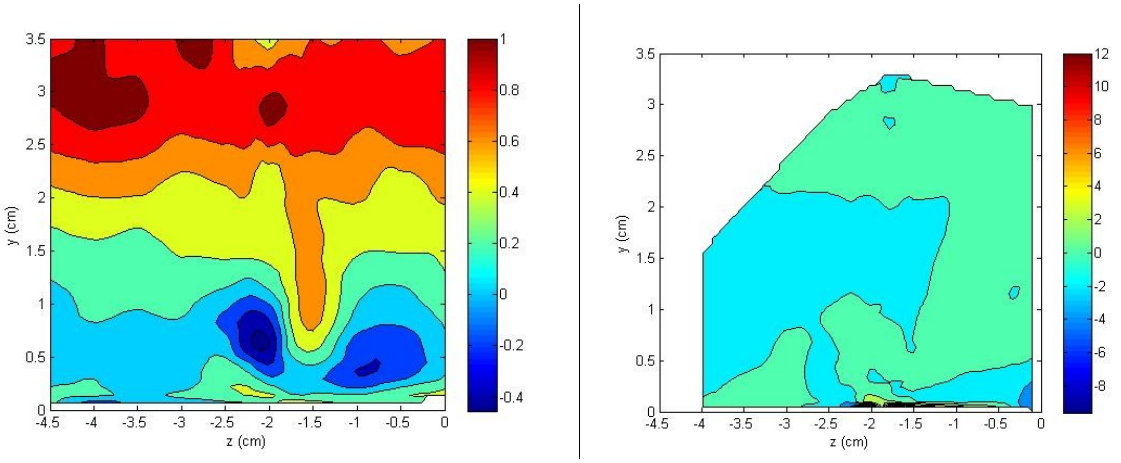

Figure 3.2.21 Parameter *II*, Current Study (Left) and Kuhl's Study (Right)

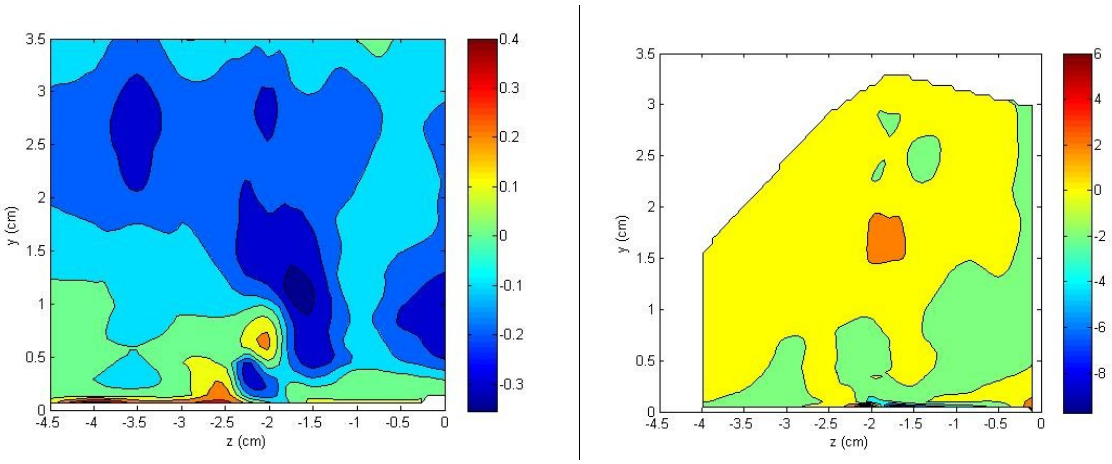

Figure 3.2.22 Parameter *III*, Current Study (Left) and Kuhl's Study (Right)

3.2.6 Triple Product Correlations

Several triple product correlations were studied, focused on the $\overline{v^3}$, $\overline{uv^2}$, and $\overline{v^2w}$ triple products. The importance of these particular triple products come from Simpson [1995], where they are used for turbulent transport equations to account for lag.

The B_2 parameter is given by $B_2 = \overline{v^3}/\sqrt{\overline{uv^2}^2 + \overline{v^2w}^2}$. The correlation is approximately 1 to 1.5 throughout much of the flow field for the current study, however there are sharp peaks on either side of the vortex core and near the outboard wall. Kuhl's work does not demonstrate the sharp peaks near the vortex core, and there is an abnormally strong negative value near the centerline and tunnel wall, possibly due to non-converged triple products.

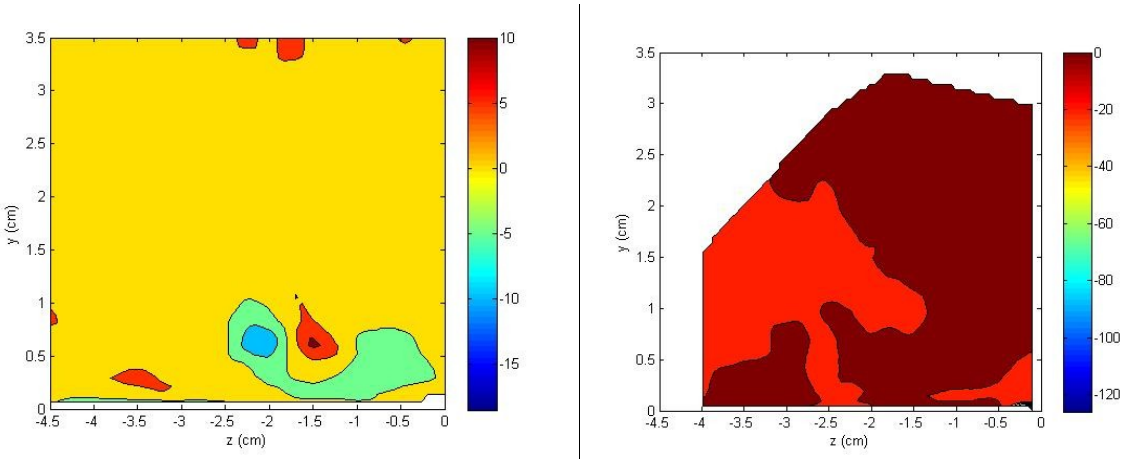

Figure 3.2.23 B_2 Parameter, Current Study (Left) and Kuhl's Study (Right)

The $\overline{vq^2} = \left(\overline{u^2v} + \overline{v^3} + \overline{vw^2}\right)$, or *vTKE*, parameter, specifically the normalized $\overline{vq^2}$ form given by $\overline{v^3}/\overline{vq^2}$ and described by Ciochetto [1997] were also studied. The color bars in Figure 3.2.24 are slightly misleading, Kuhl's work shows much greater peak values, although both studies are show values of approximately 0.3 to 0.4 away from the vortex and wall, which agrees with Ciochetto's findings.

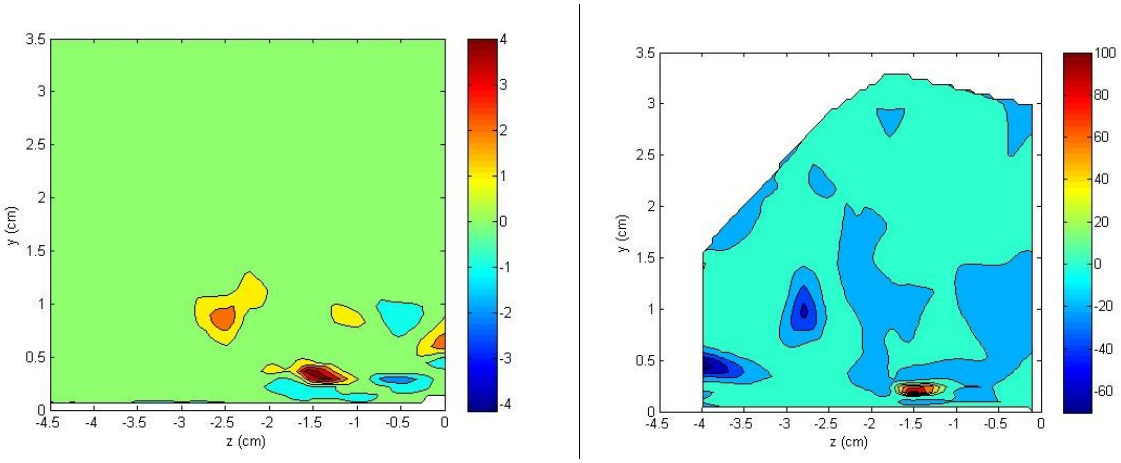

Figure 3.2.24 Normalized mean vq^2 Parameter, Current Study (Left) and Kuhl's Study (Right)

3.3Results at x = 44.5 cm Plane

3.3.1 Mean Velocities

At the 44.5 cm plane, the mean velocity contours and secondary flow vectors show a much more diffuse vortex. The vortex core has moved farther away from the wall and tunnel centerline, as expected, to a position of roughly z = -2.75 cm and y = 1.3 cm. Figure 3.3.1 shows that the thinning affect the vortex has on the tunnel centerline has decreased, and this will be discussed further in Section 3.4. At this point, the *U* velocity defect near the vortex core is essentially nonexistent, and the circulation has decreased to -0.0151 m^2/s, which is weaker than the vortex studied by Kuhl at 0.0156 m^2/s. This is a change in circulation of approximately 40% compared to the upstream value as opposed to the 33% drop of the previous study. This is not surprising as the 44.5 cm plane is approximately 17 chord lengths downstream. According to Lin [2002], most vortex generators are meant to locally affect the flow field within approximately 10 chord lengths downstream. It appears that the thicker boundary layer, with higher edge velocity, of the current study has disrupted the vortex structure at this far downstream location, as seen in Figures 3.3.4 and 3.3.5.

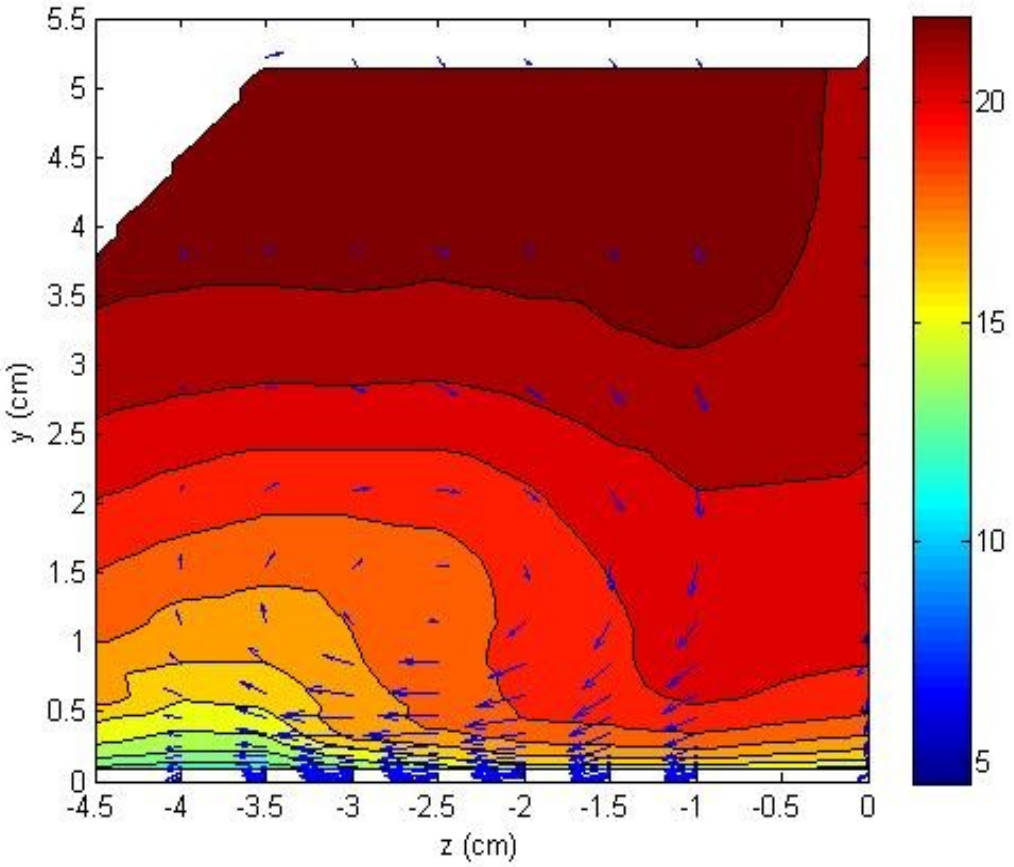

Figure 3.3.1 Dimensional *U*, *m/s*, with overlay of secondary (*VW*) flow vectors

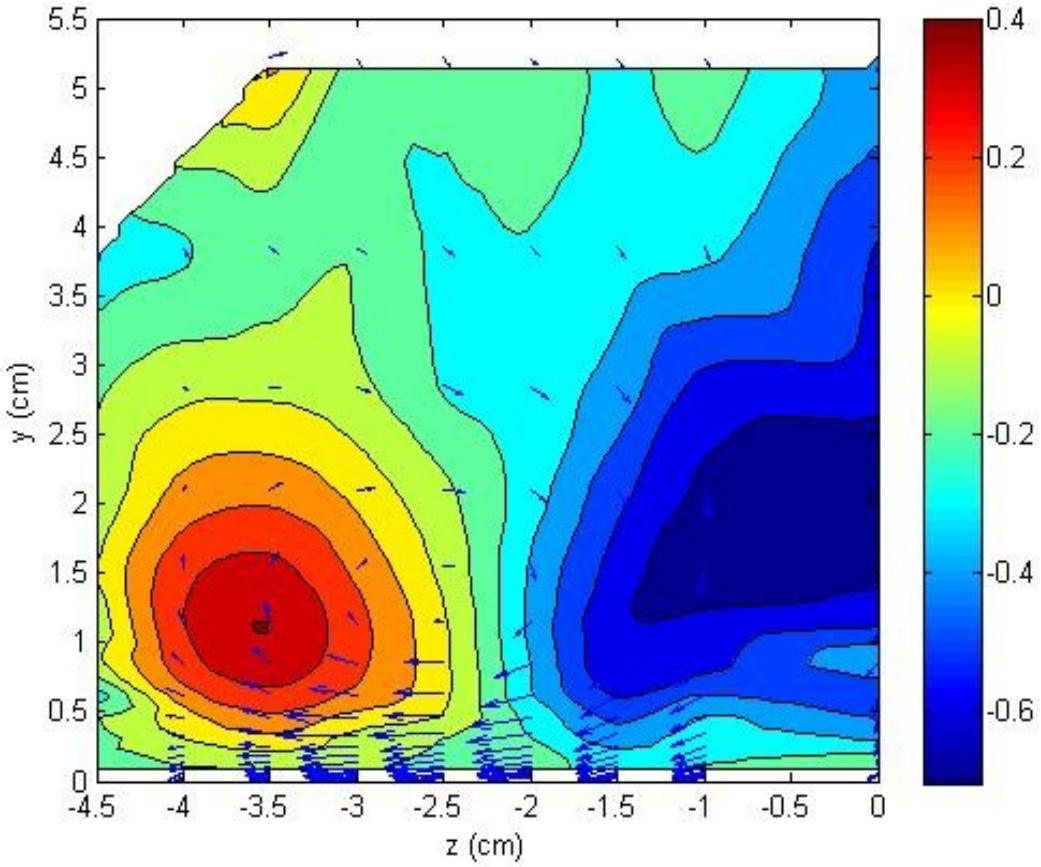

Figure 3.3.2 Dimensional *V*, *m/s*, with overlay of secondary (*VW*) flow vectors

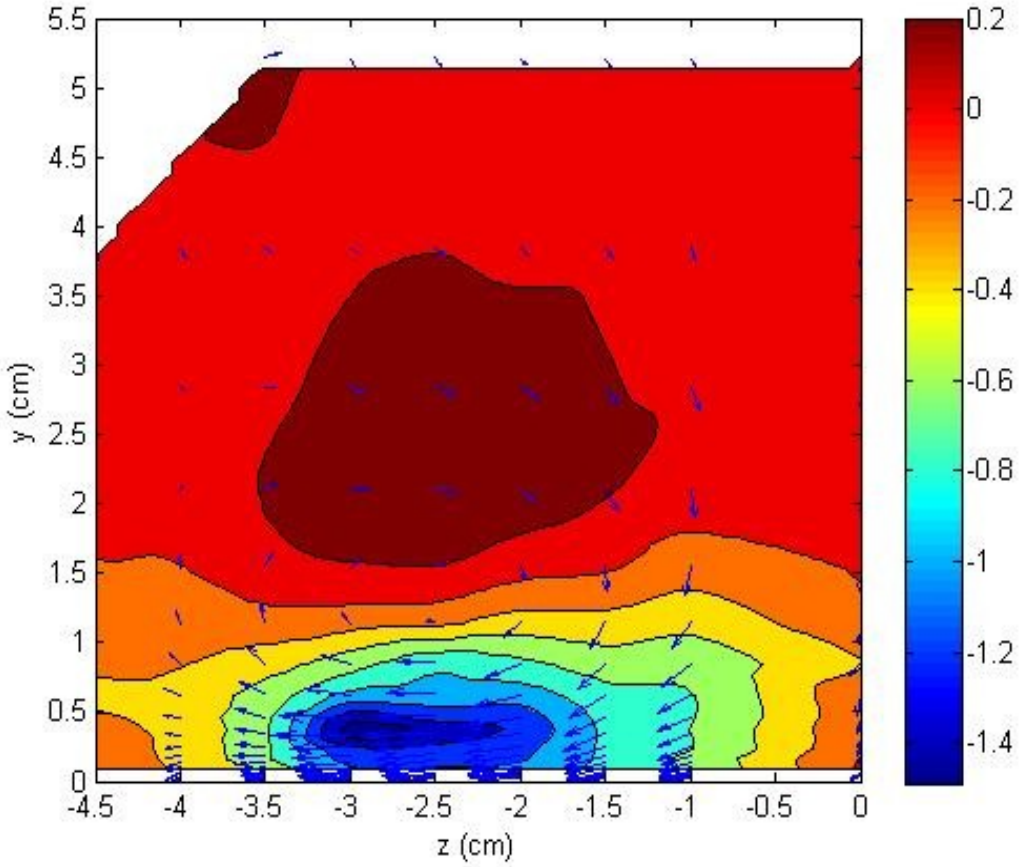

Figure 3.3.3 Dimensional *W*, *m/s*, with overlay of secondary (*VW*) flow vectors

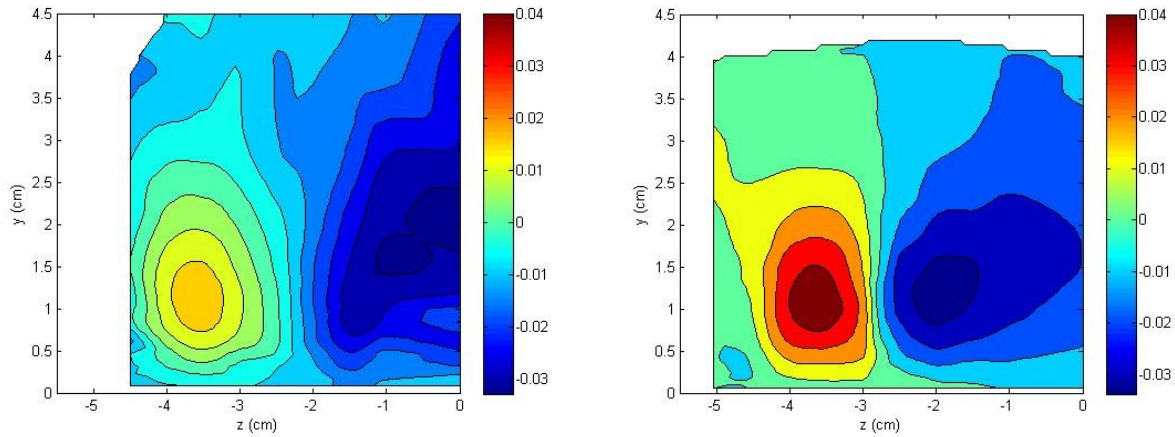

Figure 3.3.4 V/U_e for the Current Study (Left) and Kuhl's Study (Right)

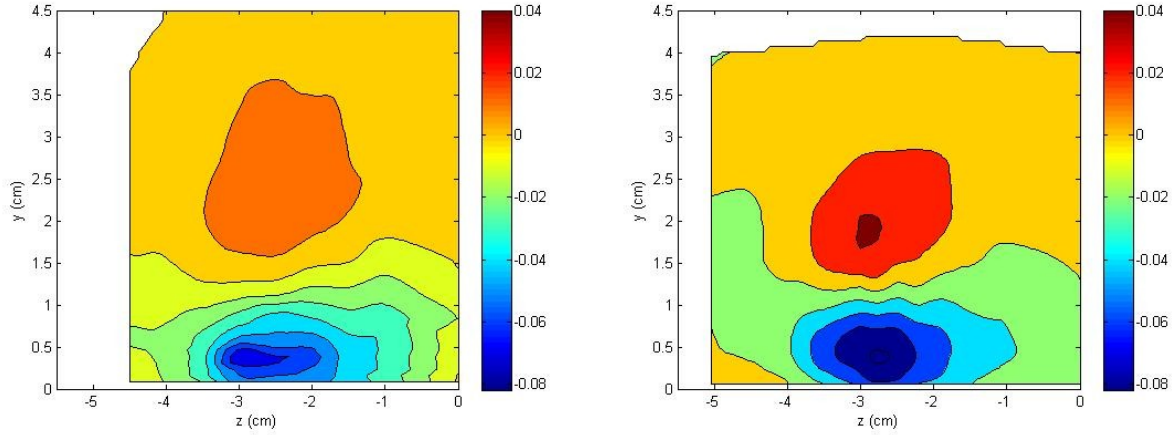

Figure 3.3.5 W/U_e for the Current Study (Left) and Kuhl's Study (Right)

3.3.2 Normal Stresses

The normal stresses exhibit similar behavior to the data at the upstream plane, but note that the scales are equal in order to better demonstrate the relative magnitudes. The peak in $\overline{v^2}$ at the center of the vortex is now more diffuse, but still isolated to the vortex core, which further justifies the value of $\overline{v^2}$ as an indicator of vorticity, but $\overline{w^2}$ now peaks in the inboard region near the tunnel wall. The $\overline{u^2}$ normal stress shows peaks near the wall; this is similar to a two-dimensional boundary layer, but the peak shared with $\overline{w^2}$ is much diminished.

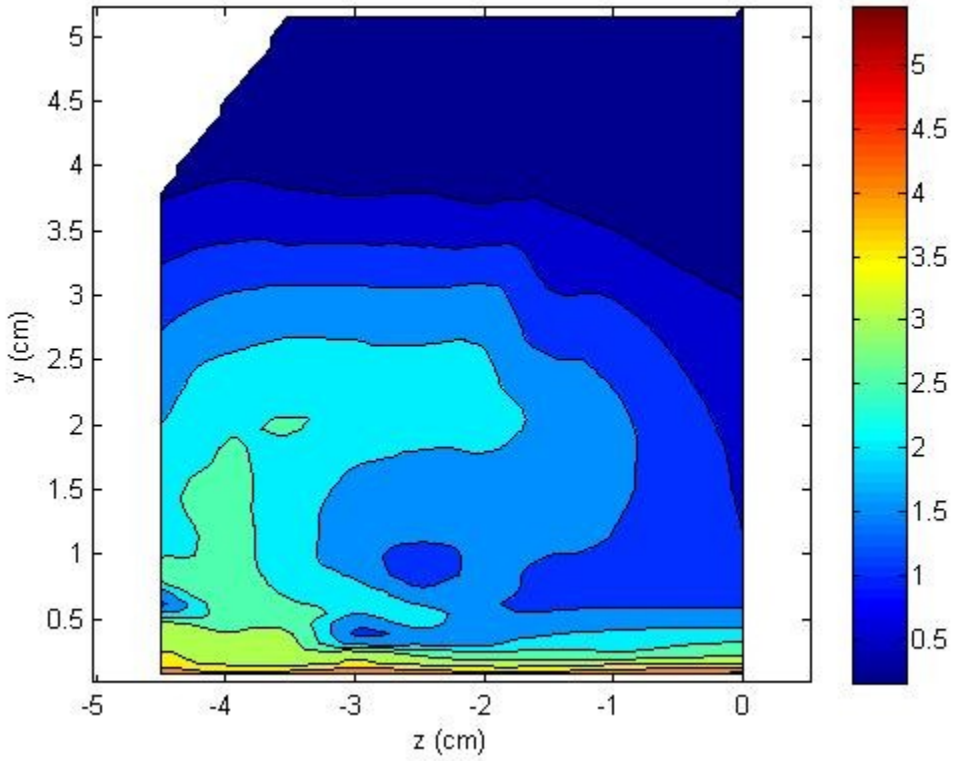

Figure 3.3.6 Mean u^2 normal stress, m^2/s^2

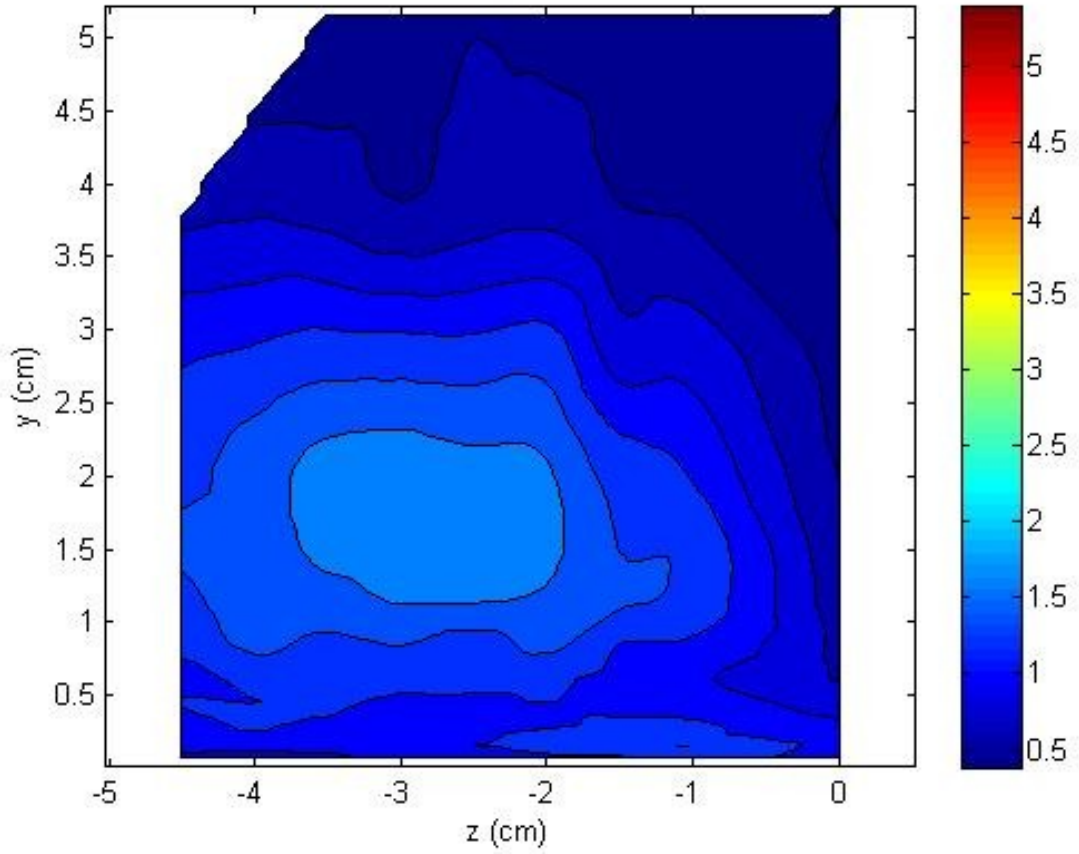

Figure 3.3.7 Mean v^2 normal stress, m^2/s^2

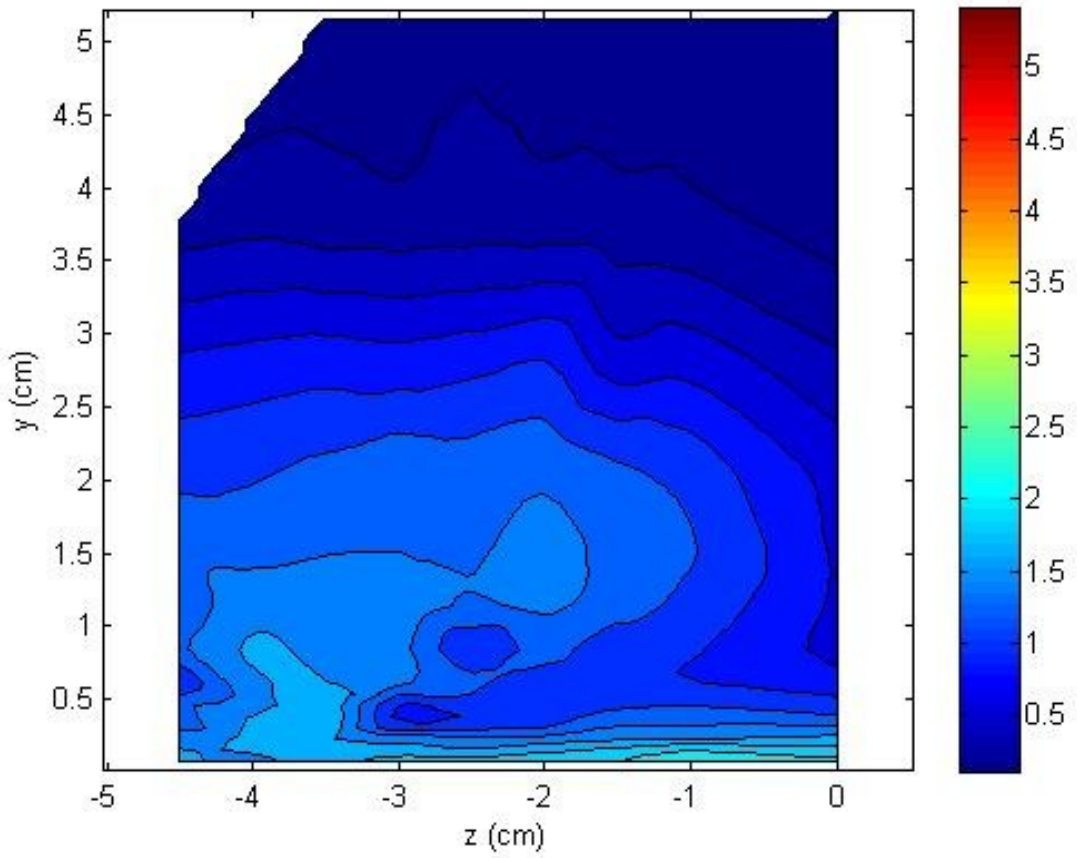

Figure 3.3.8 Mean w^2 normal stress, m^2/s^2

The non-dimensional normal stress comparisons, Figures 3.3.7 through Figure 3.3.9, truly demonstrate the more diffuse nature of the vortex and the thicker boundary layer of the current study. Note the different scales between the normal stresses, the $\overline{u^2}/U_e^2$ term has the greatest magnitude. Also note that $\overline{v^2}/U_e^2$ show much different behavior between the current study and Kuhl's study; the vortex in the current study appears to wander slightly more, most likely caused by the more energetic inflow boundary layer.

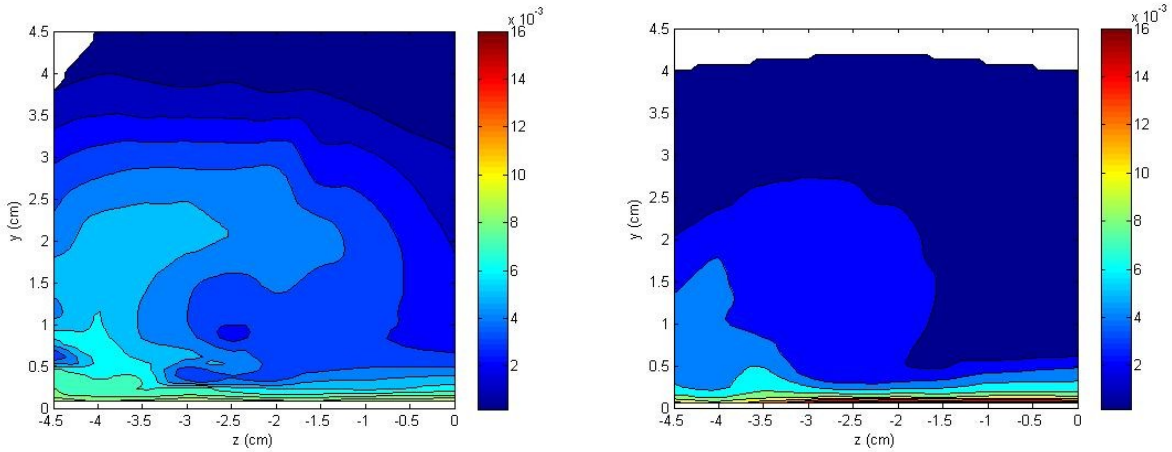

Figure 3.3.9 Non-dimensional mean u^2/U_e^2 normal stress, Current Study (Left) and Kuhl's Study (Right)

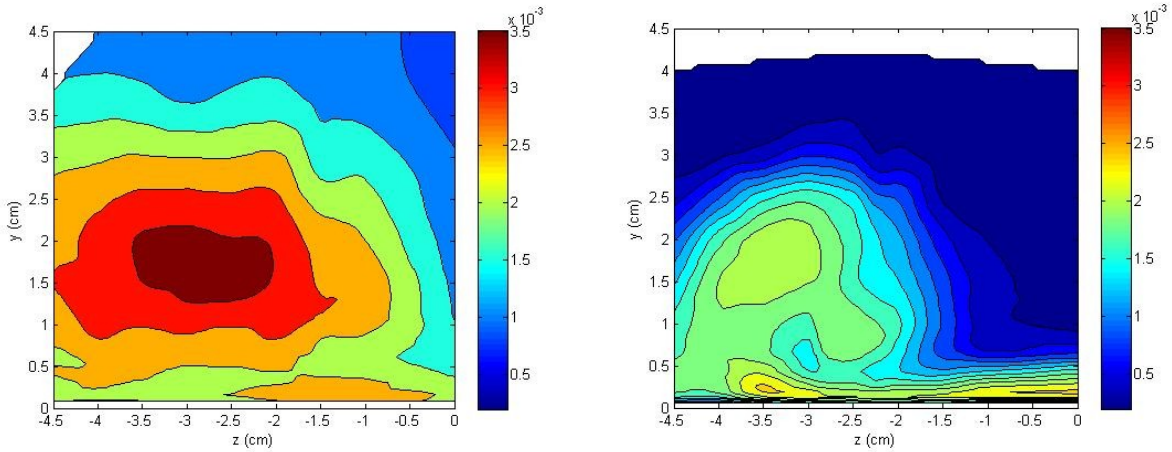

Figure 3.3.10 Non-dimensional mean v^2/U_e^2 normal stress, Current Study (Left) and Kuhl's Study (Right)

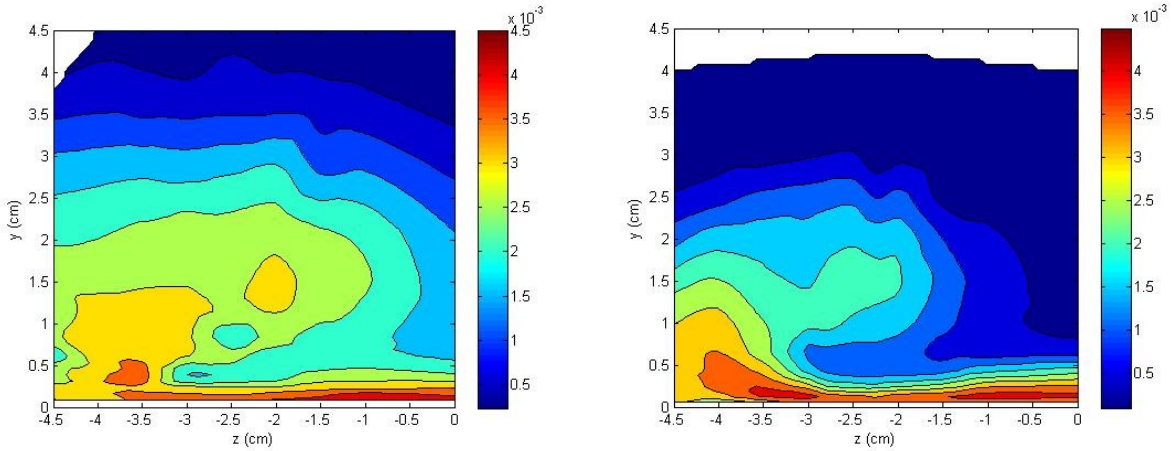

Figure 3.3.11 Non-dimensional mean w^2/U_e^2 normal stress, Current Study (Left) and Kuhl's Study (Right)

3.3.3 Turbulent Kinetic Energy

Once again, the more diffuse nature of the vortex in the current study is apparent. Both the current study and Kuhl's work show that the TKE peaks near the wall, although the presence of the vortex core is still apparent, and is mostly due to the $\overline{v^2}$stress.

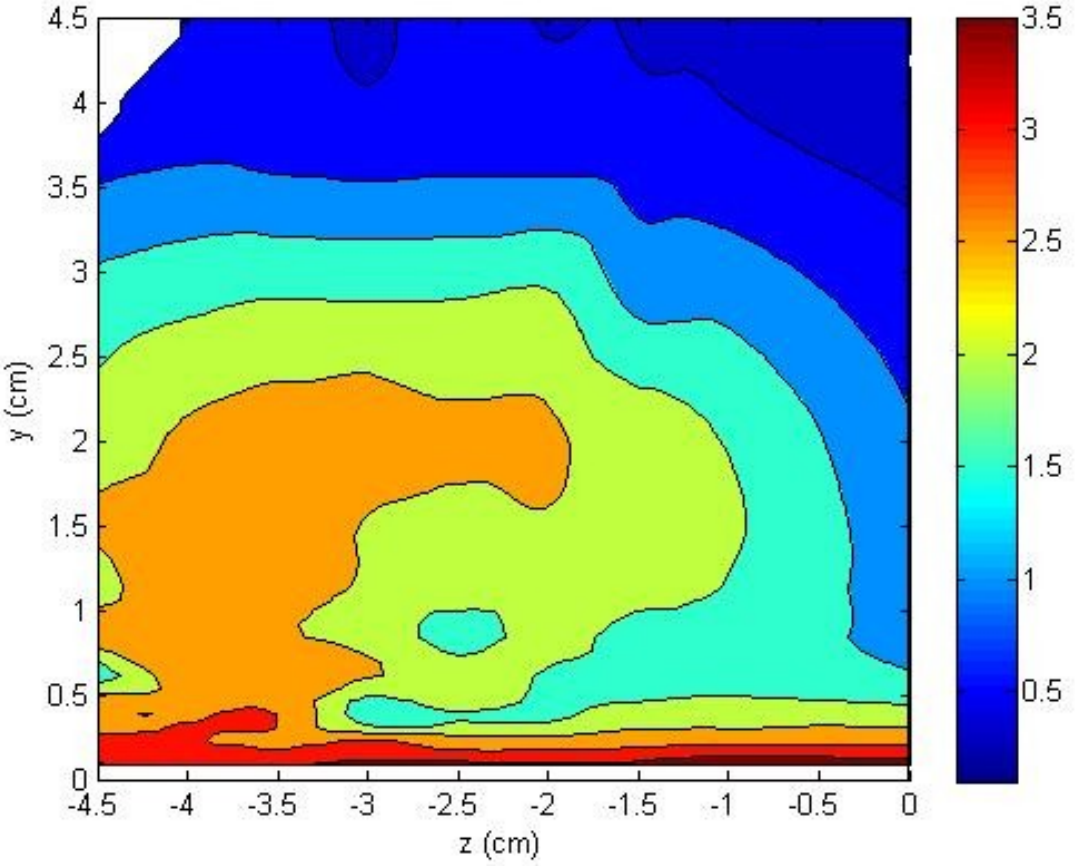

Figure 3.3.12 Dimensional *TKE*, m^2/s^2

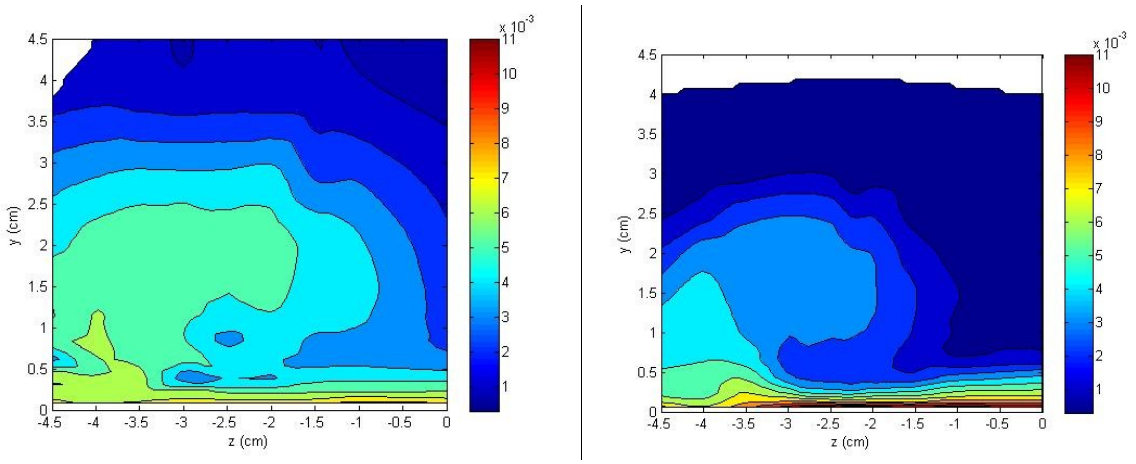

Figure 3.3.13 Non-dimensional TKE/U_e^2, Current Study (Left) and Kuhl's Study (Right)

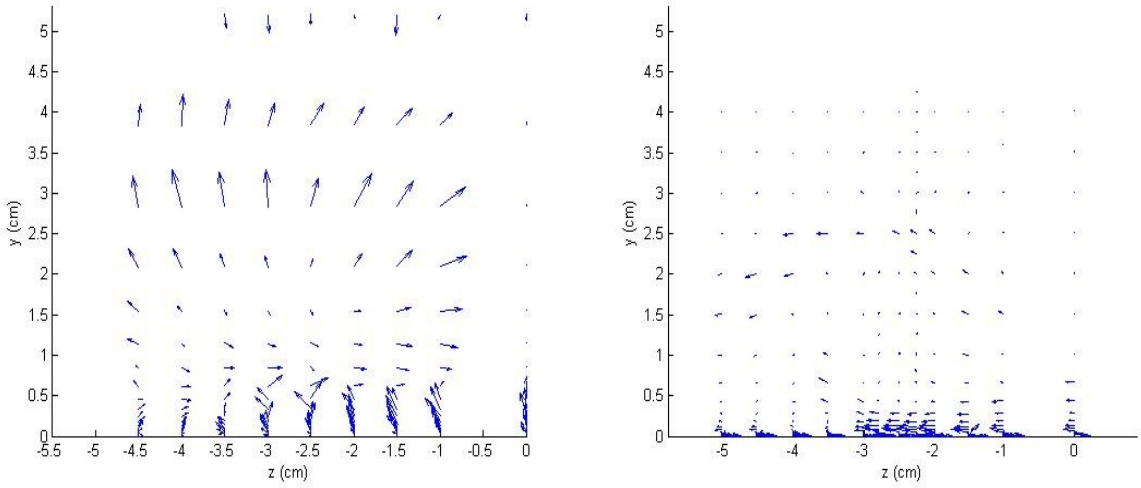

Figure 3.3.14 Dimensional *TKE* transport vectors, *m/s*, Current Study (Left), Kuhl's Study (Right)

The TKE transport vectors of the current study show more jitter than Kuhl's. With the larger, more diffuse vortex at this location, it is not surprising that the jitter has increased. Both studies still show similar behavior near the wall.

3.3.4 Shear Stresses

The shear stresses all show a similar behavior and structure as the upstream plane, but they have convected with the vortex and are much more diffuse and of much weaker intensity. Note that there is a strange peak in $\overline{uw}$ at z = -3.0 cm; this could be due to a low data rate noticed for this particular point.

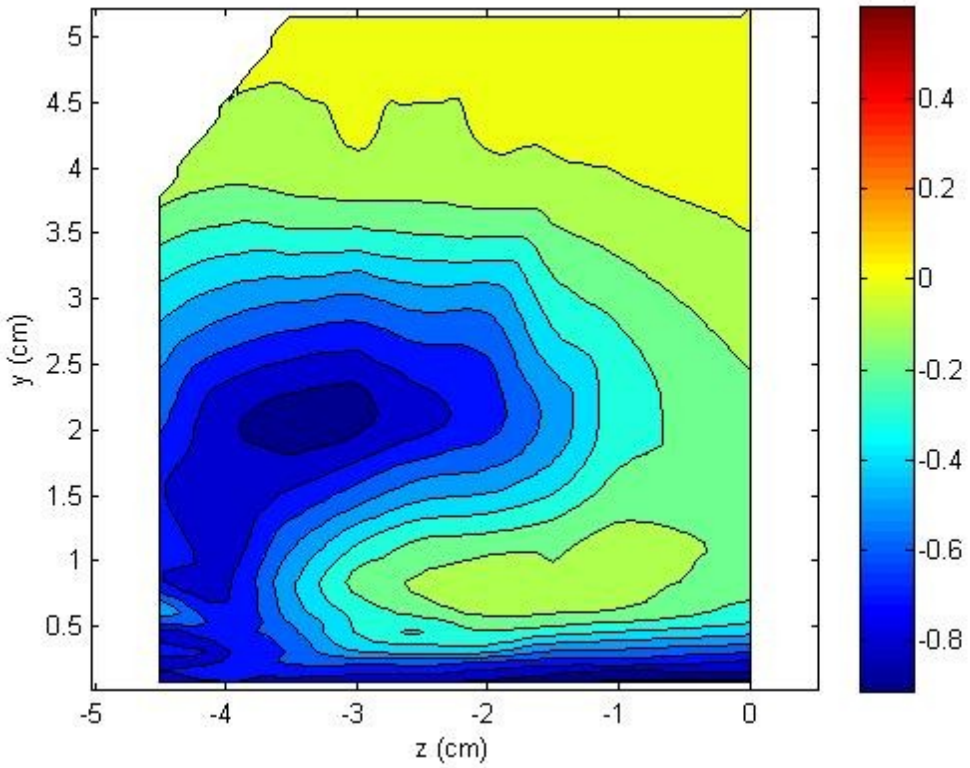

Figure 3.3.15 Mean *uv* normal stress, m^2/s^2

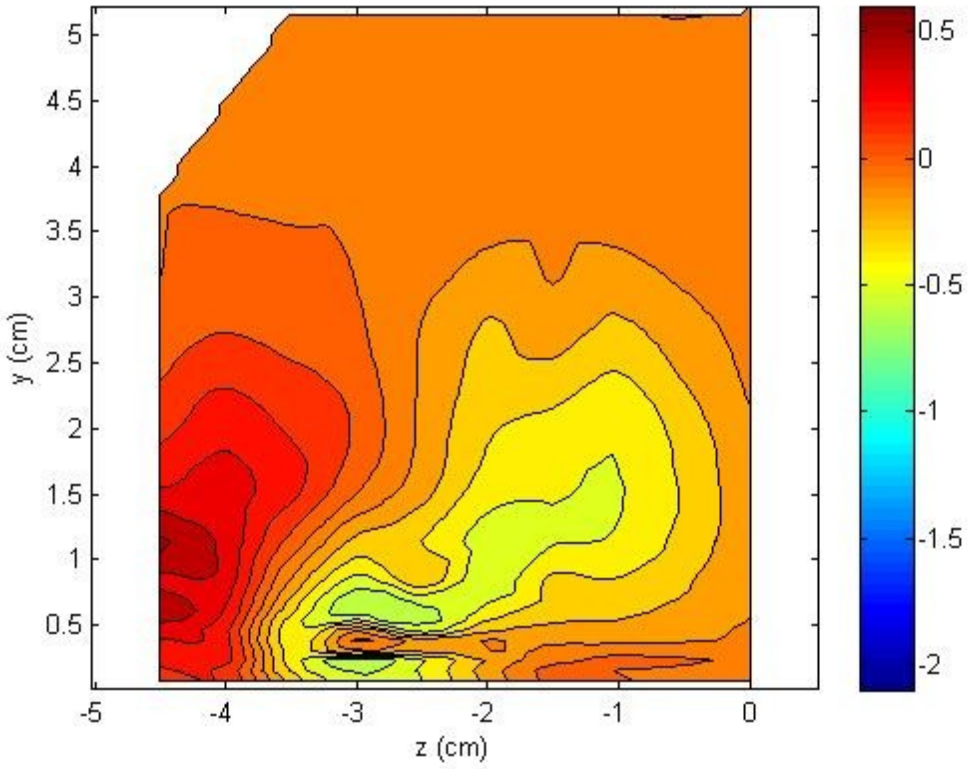

Figure 3.3.16 Mean *uw* normal stress, m^2/s^2

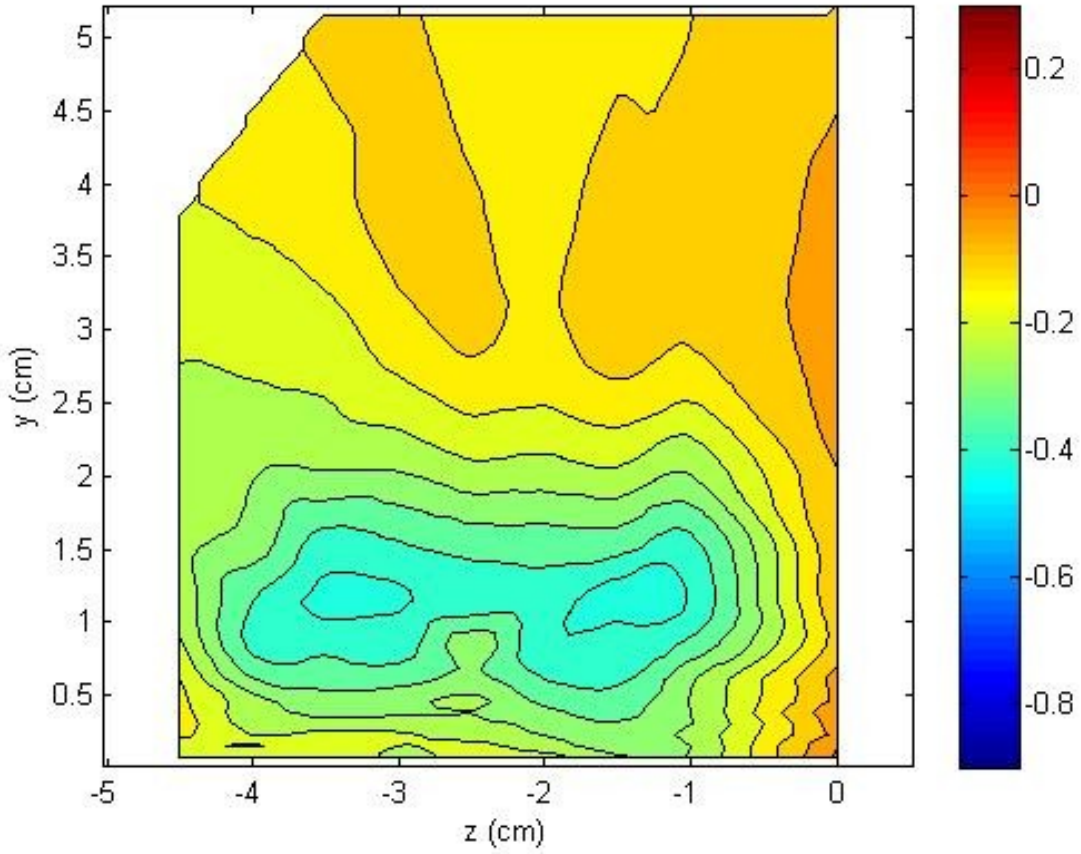

Figure 3.3.17 Mean *vw* normal stress, m^2/s^2

3.3.5 Reynolds Stress Correlations

This section discusses the same correlations as Section 3.2.5. The parameter $\frac{-\overline{uv}}{\sqrt{\overline{u^2}\overline{v^2}}}$ is shown in Figure 3.3.18. Both the current study and Kuhl's study show similar behavior; a region of negative correlation beneath the core, positive correlation outboard, and zero correlation away from the wall. The correlation values retain the same magnitudes between the 10.5 cm and 44.5 cm planes, see Figure 3.2.18, the vortex cores have simply become more diffuse and the correlation has spread in a similar manner.

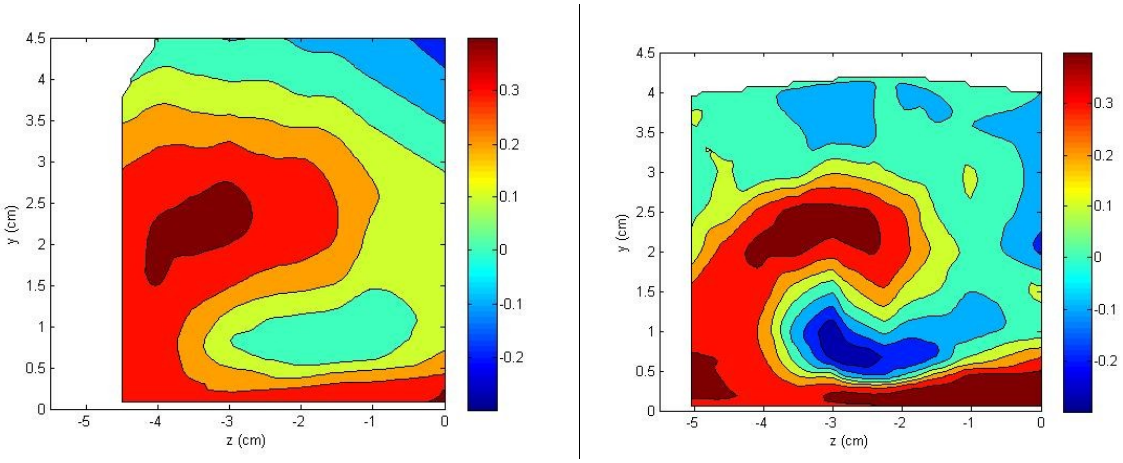

Figure 3.3.18 $\frac{-\overline{uv}}{\sqrt{\overline{u^2}\overline{v^2}}}$ Parameter, Current Study (Left) and Kuhl's Study (Right)

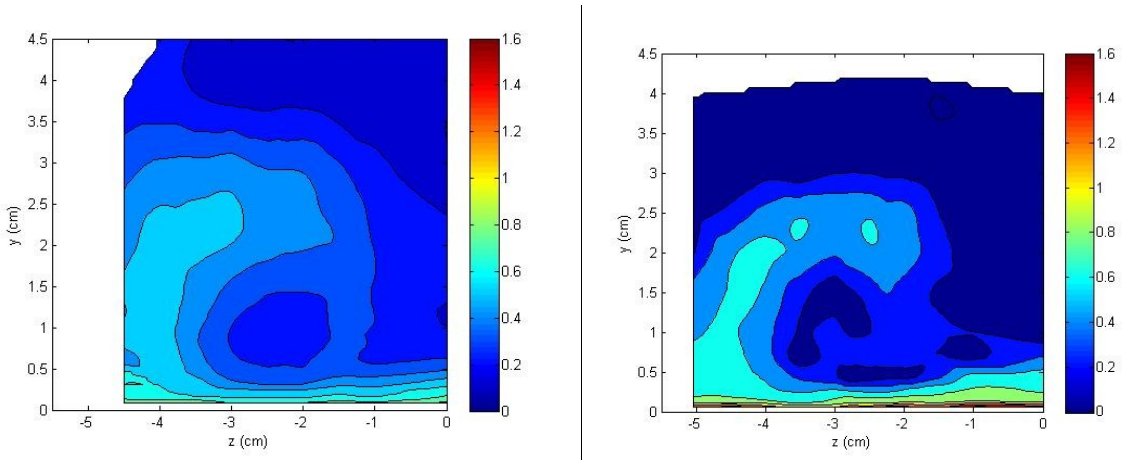

Figure 3.3.19 *I/S* Parameter, Current Study (Left) and Kuhl's Study (Right)

The 1/S parameter is shown in Figure 3.3.19. Once again, both studies show a similar behavior, with the parameter reducing to zero with increasing y. Kuhl's work shows a higher peak value, although this is most likely due to better spatial resolution near the wall. In both cases, there are regions of approximately constant 1/S of 0.3 to 0.4 which correspond to the log region..

Figures 3.3.20 through 3.3.22 show Ölçmen parameters defined in Section 3.2.5, with each parameter formulated as RHS-LHS. Once again, the current study does not show a strong correlation through the boundary layer, although there are some regions in the log layer that demonstrate agreement for Parameter I.

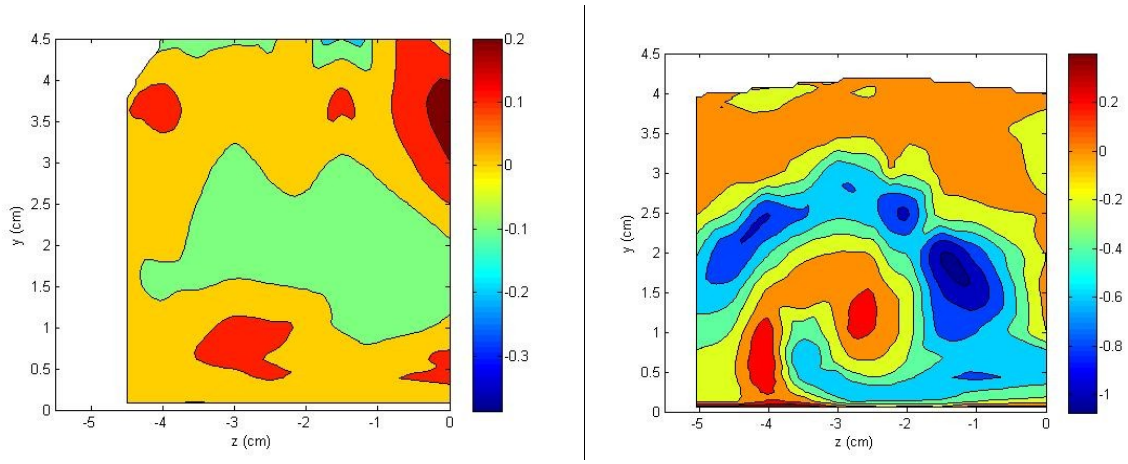

Figure 3.3.20 Parameter *I*, Current Study (Left) and Kuhl's Study (Right)

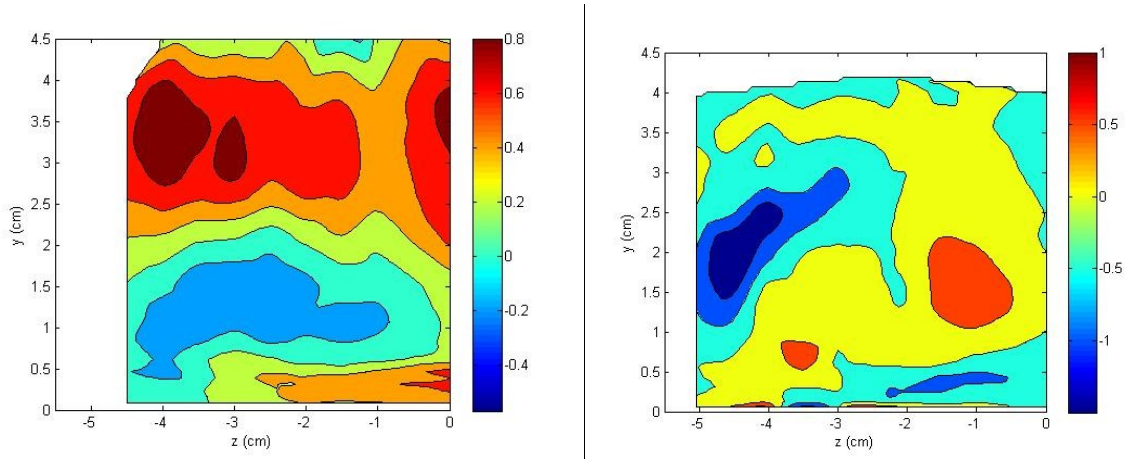

Figure 3.3.21 Parameter *II*, Current Study (Left) and Kuhl's Study (Right)

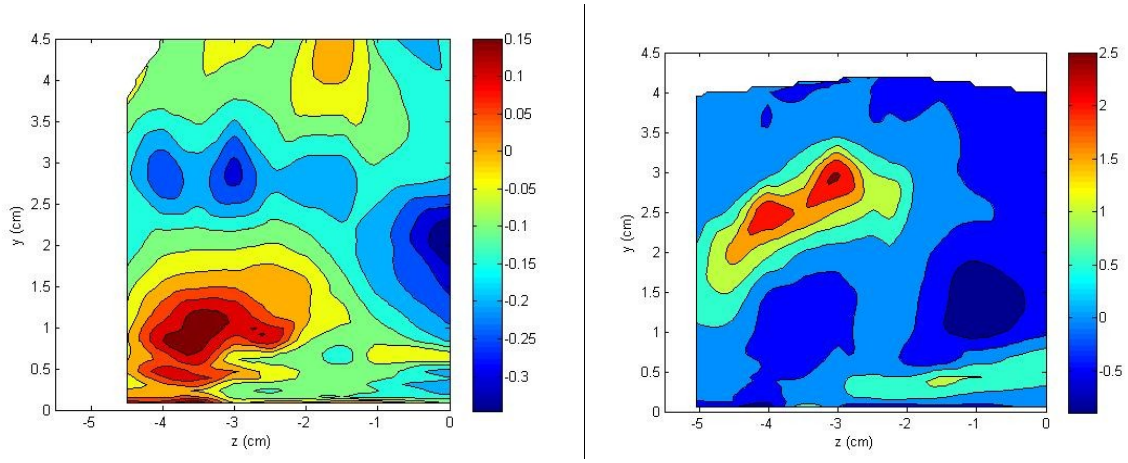

Figure 3.3.22 Parameter *III*, Current Study (Left) and Kuhl's Study (Right)

3.3.6 Triple Product Correlations

This section discusses the same correlations as Section 3.2.6. The B_2 parameter is shown below in Figure 3.3.23. As with the 10.5 cm plane, the correlation is approximately 1 to 1.5 throughout much of the flow field for the current study, however the peaks near the vortex core are not evident as they were at the 10.5 cm plane. Kuhl's work is harder to discuss, there seems to be more of a spread in features. Overall, the B_2 does not necessarily show a strong correlation for this flow.

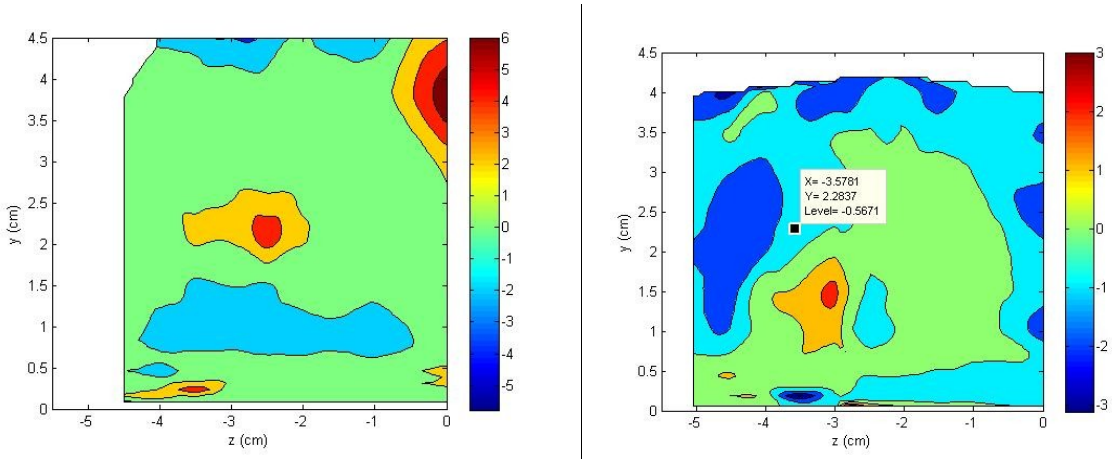

Figure 3.3.23 B_2 Parameter, Current Study (Left) and Kuhl's Study (Right)

The normalized $\overline{vq^2}$ parameter is shown in Figure 3.2.24. Kuhl's study does not show the same peak near the centerline, but does show more scatter. The current study, with it more diffuse vortex, has values of approximately 0.3 to 0.5 away from the vortex and wall, which agrees with Ciochetto's findings.

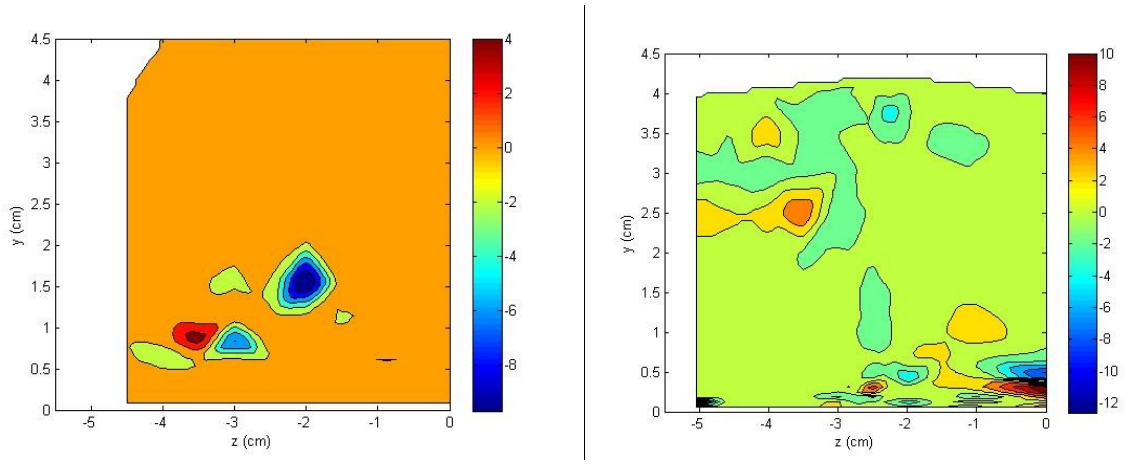

Figure 3.3.24 Normalized mean vq^2 Parameter, Current Study (Left) and Kuhl's Study (Right)

3.4 Wall Shear Stress

The variance in wall friction velocity, $u_\tau = \sqrt{\tau_w/\rho}$, along the spanwise direction is shown in Figure 3.4.1 and Figure 3.4.2. These plots demonstrate how the vortices have increased the friction velocity in the inboard region under the vortex core and decreased the friction velocity outside the core as expected. At the measurement location upstream of the vortex generators the friction velocity was approximately 077 m/s.

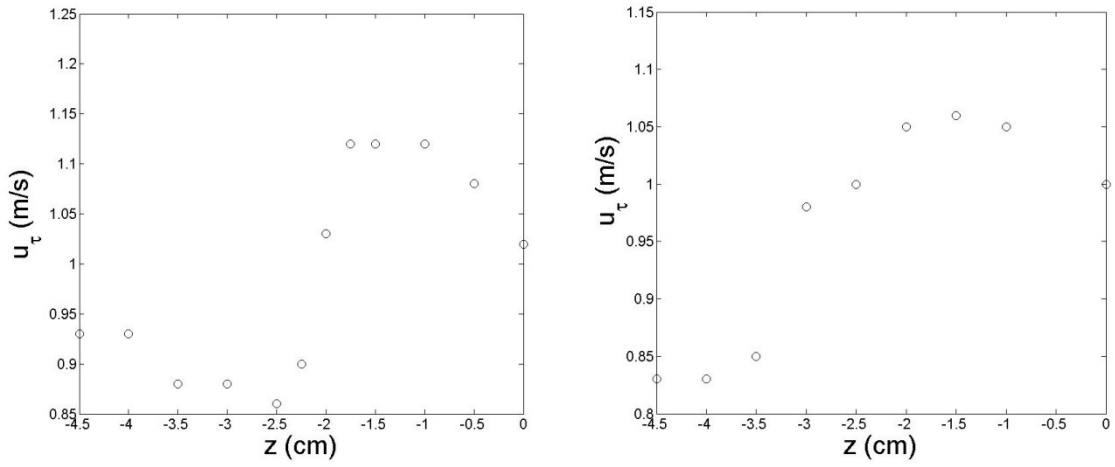

Figure 3.4.1 Friction Velocity, *m/s*, vs. Spanwise Location, x = 10.5 cm (Left) and 44.5 cm (Right) Planes

3.5 Flow Angle

The flow angle, $FA = \arctan(W/U)$, shows the directionality of the flow. The vortex has a much stronger effect on the directionality beneath the vortex core due to the presence of the wall, increasing the angularity by a factor of 3 to 4 as compared to above the vortex core. At the 44.5 cm location, the vortex has become much weaker, the peak flow angle being approximately three times less than the 10.5 cm location.

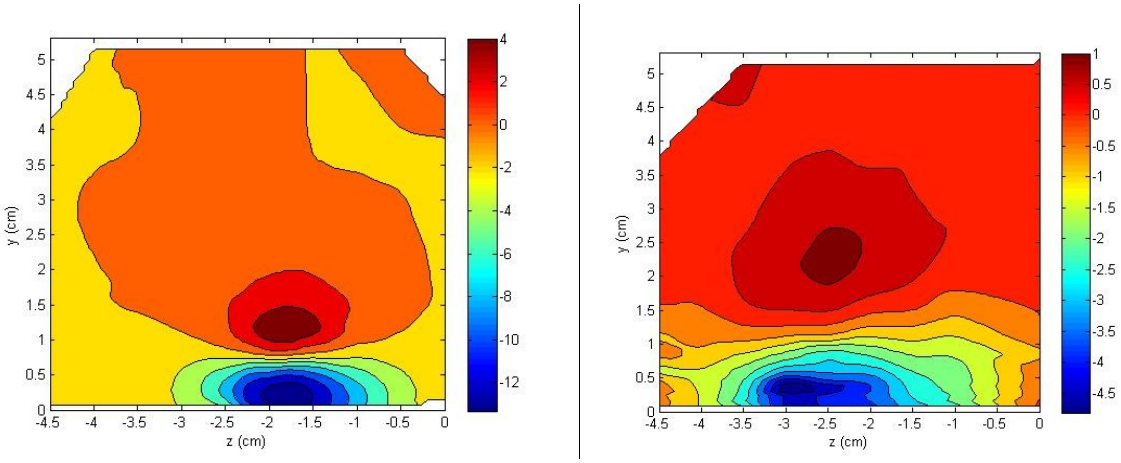

Figure 3.6.1 Flow Angle, in degrees, x = 10.5 cm plane (Left) and x = 44.5 cm plane (Right)

3.6 Streamwise Vorticity and Helicity

The non-dimensional streamwise vorticity, $\omega_x = \frac{h*(dW/dy - dV/dz)}{U_e}$, where h is the vortex generator height, was calculated at each downstream plane. As compared to Kuhl's study, the peak vorticity of the current study, at the 10.5 cm plane, is approximately 60% higher. At the 44.5 cm plane, the peak vorticity is much weaker, the structure of the vortex has become larger and more diffuse, even demonstrating a bimodal peak, and there appears to be a strong counter-acting vorticity peak below the vortex core.

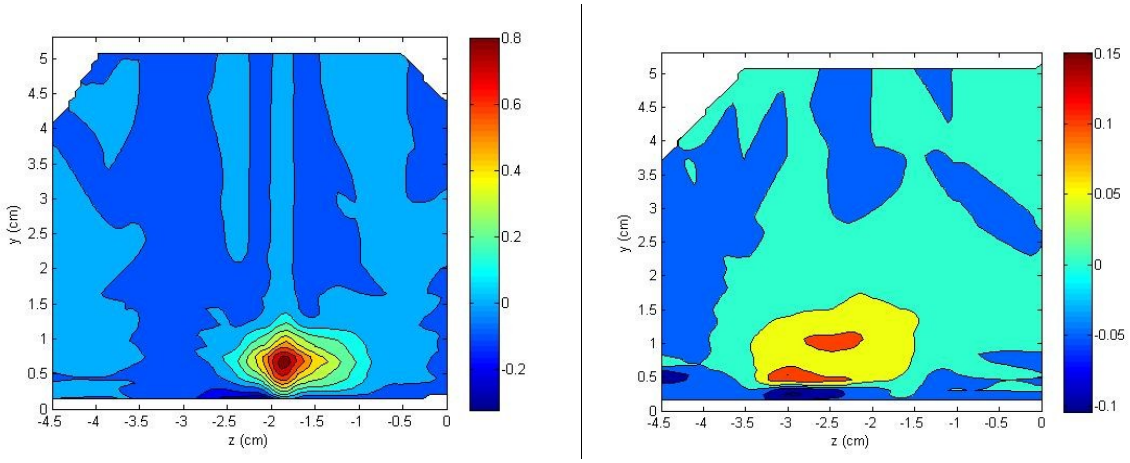

Figure 3.6.1 Streamwise Vorticity ω_x, x = 10.5 cm plane (Left) and x = 44.5 cm plane (Right)

The non-dimensional streamwise helicity, $H_x = \frac{\omega_x U}{U_e}$, and a measure of solid body motion, is shown in Figure 3.6.2. The positive values at the vortex core show the strong clockwise rotation of the common flow down vortex. There appears to be a much weaker, opposing rotation feature beneath the vortex core at the both measurement planes. This contra-rotating vortex may be the prime contributor to the $\overline{u^2}$and $\overline{w^2}$peaks noticed earlier.

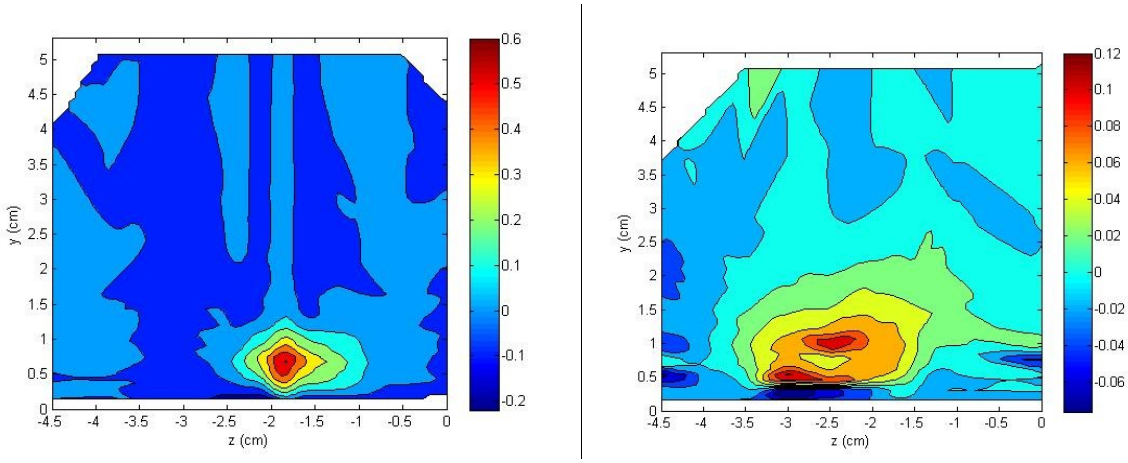

Figure 3.6.2 Streamwise Helicity H_x, x = 10.5 cm plane (Left) and x = 44.5 cm plane (Right)

Chapter 4. Conclusions and Future Work

4.1 Conclusions

This work presents non-intrusive, near-wall velocity and turbulence statistics for a complex three-dimensional flow driven by two contra-rotating vortices. Comparisons with previous, non-intrusive, work show a similar vortical structure, but with features of greater magnitude at the measurement plane nearest the vortex generators due to the increased momentum of the incoming flow of this study. Despite different inflow boundary layers and edge velocities, the turbulence quantities non-dimensionalized on edge velocity show good agreement between Kuhl's work and the current study. This implies that the vortex is an inertial process, more dependent on the inviscid flow field. However, the higher edge velocity and more energetic incoming boundary layer caused the vortex of the current study to diffuse much more quickly than in the work of Kuhl.

A jump in friction velocity in between the paired vortices indicates the energizing presence of the vortex generators, and is indicated by the $\overline{uw}$ peaks. Additionally, the $\overline{v^2}$ indicated areas of high vorticity, demonstrating how important this term is to properly model turbulence in simulations, the assumption of isotropic contributions to TKE in the off-wall turbulent structure does not seem to apply. Unlike previous work, it was found that peak TKE was confined mainly to the vortex core, with lower magnitudes near the centerline, most likely due to the higher circulation of the vortex in this study.

Comparisons of correlation coefficients were made between the current study and Kuhl's work. The most promising correlation appears to be the 1/S parameter for stresses and normalized $\overline{vq^2}$ parameter for triple products.

While issues have been found with the lab facilities that made data acquisition difficult, several suggestions have been made that should increase year round productivity. In addition, further reductions in data acquisition time can be made due to new developments in computer technology, such as solid state hard drives, which should further boost productivity.

A redesign of the probe head to eliminate some degrees of freedom would help to eliminate some sources of uncertainty in the fringe gradient calculations and improve probe stability.

4.2 Future Work

Based off the current study, the addition of a higher edge velocity study, possibly around 28 m/s, would aid in a parametric examination of the vortex flow. Due to how most vortex generators are used to locally improve the flow field within 10 chord lengths, adding a measurement plane at x = 25 cm may be beneficial.

If possible, measurements should be made as close to, and at the same height of the vortex generator tip in order to determine if a better collapse could be found on an 'incoming' velocity rather than edge velocity.

References

Allan, B.G., Yao, Chung-Sheng, and Lin, J.C., "Numerical Simulations of Vortex Generator Vanes and Jets on a Flat Plate," 1st Flow Control Conference, St. Louis, MO, June 24-26 2002, AIAA-2002-3160.

Bennington, J.L., "Effects of Various Shaped Roughness Elements in Two-Dimensional High Reynolds Number Turbulent Boundary Layers," Master's Thesis, VPI&SU, August 24, 2004.

Bragg, M.B., and Gregorek, G.M., "Experimental Study of Airfoil Performance with Vortex Generators," Journal of Aircraft, Vol.24 No. 5 pp. 305-309, May 1987.

Bttner, L. and Czarske, J., "A multmode-fibre laser-doppler anemometer for highly spatially resolved velocity measurements using low-coherence light," Measurement Science and Technology, vol. 12, pp. 1891-1903, 9 October 2001.

Bttner, L. and Czarske, J., "Spatial resolving laser Doppler velocity sensor using slightly tilted fringe systems and phase evaluation," Measurement Science and Technology, vol. 14, pp. 2111-2120, 9 October 2003.

Bttner, L. and Czarske, J., "Determination of the axial velocity component by a laser-Doppler velocity profile sensor," Journal of the Optical Society of America, vol. 23, pp. 444-454, February 2006.

Chiochetto, D.S., "Analysis of Three Dimensional Turbulent Shear Flow Experiments with Respect to Algebraic Modeling Parameters," Master's Thesis, VPI&SU, May 7, 1997.

Cutler, A.D., and Bradshaw, P., “The Interactions Between a Strong Longitudinal Vortex and a Turbulent Boundary Layer,” AIAA/ASME 4th Fluid Mechanics, Plasma Dynamics and Lasers Conference, AIAA-86-1071, May 1986.

Cutler, A.D., and Bradshaw, P., “Vortex/Boundary-Layer Interactions,” 27th Aerospace Sciences Meeting, Reno, NV, AIAA-89-0083, January 9-12 1989.

Czarske, J. "Laser Doppler velocity profile sensor using a chromatic coding," Measurement Science and Technology, vol. 12, no. 1, pp. 52-57, 2001.

Czarske, J., Bttner, L., Razik, ,T., and Muller, H., "Boundary layer velocity measurements by a laser Doppler profile sensor with micrometre spatial resolution," Measurement Science and Technology, vol. 13, pp. 1979-1989, November 2002.

Dudek, J.C., “An Empirical Model for Vane-type Vortex Generators in a Navier-Stokes Code,” 42nd Aerospace Sciences Meeting and Exhibit, Reno, NV, AIAA-2005-1003, January 10-13 2005.

Echols, W.H. and Young, J.A., “Studies of Portable Air-Operated Aerosol Generatiors,” U.S. Naval Research Laboratory, NRL Report #5929, July 26, 1963.

Hopkins, A.M. R., "Fluid Dynamics and Surface Pressure Fluctuations of Turbulent Boundary Layers Over Densely Distributed Roughness," PhD Thesis, VPI&SU, 2010.

Jirasek, A., “A Vortex Generator Model and its Application to Flow Control,” 22nd Applied Aerodynamics Conference and Exhibit, Providence, RI, AIAA-2004-4965, August 16-19 2004.

Kuhl, D.D., "Near Wall Investigation of Three Dimensional Turbulent Boundary Layers," Master's Thesis, VPI&SU, August 22, 2001.

Lehmann, B., Nobach, H., and Tropea, C., "Measurement of acceleration using the laser Doppler technique," Measurement Science and Technology, vol. 13, pp. 1367-1381, July 2002.

Lin, J.C., “Review of Research on Low-Profile Vortex Generators to Control Boundary-Layer Separation,” Progress in Aerospace Sciences, vol. 38, pp.389-420, 2002.

Liu, B., Whitby, K., and Yu, H., "A Condensation Aerosol Generator for Producing Monodispersed Aerosols in the Size Range, 0.036μ to 1.3μ," Journal de Recherches Atmospheriques, vol. 2, pp. 397-406, 1966.

Lowe, K.T., "Design and Application of a Novel Laser Doppler Velocimeter for Turbulence Structural Measurements in Turbulent Boundary Layers," PhD Thesis, VPI&SU, 2006.

Madden, M.M., "Octant Analysis of the Reynolds Stresses in the Three Dimensional Turbulent Boundary Layer of a Prolate Spheroid" Master's Thesis, VPI&SU, July 24, 1997.

May, N.E., “A New Vortex Generator Model for Use in Complex Configuration CFD Solvers,” 19th Applied Aerodynamics Conference, Anaheim, CA, AIAA-2001-2434, June 11-14 2001.

Mehta, R.D., Shabaka, I.M.M.A, Shibl, A., Bradshaw, P., “Longitudinal Vortices Imbedded in Turbulent Boundary Layers,” AIAA 21st Aerospace Sciences Meeting, AIAA-83-0378, January 1983.

Miles, P.C., “Geometry of the fringe field formed in the intersection of two Gaussian beams,” Appl. Optics, vol. 35, no. 30, pp. 5887-5895, 1996.

Nagano, Y. and Tagawa, M., “Turbulence model for triple velocity and scalar correlations,” Intenational Symposium on Turbulent Shear Flows (7th : 1989 Stanford University) Turbulent shear flows 7 : selected papers from the Seventh International Symposium on Turbulent Shear

Flows, Stanford University, USA, August 21-23, 1989, editors: F.Durst [et al.]. Berlin ; New York : Springer Verlag, 1991.

Nagano, Y. and Tagawa, M., "A structural turbulence model for triple products of velocity and scalar" Journal of Fluid Mechanics, vol. 215, pp. 639-657, 1990.

Oberkampf, W.L. and Aeschliman, D.P., "Joint Computational/Experimental Aerodynamics Research on a Hypersonic Vehicle: Part I, Experimental Results." AIAA Journal, vol. 30, no. 8, pp. 2000-2009, 1992.

Ölçmen, S.M. and Simpson, R.L., "An experimental study of a three-dimensional pressure-driven turbulent boundary layer," Journal of Fluid Mechanics, vol. 290, pp. 225-262, 1995.

Pauley, W.R., and Eaton, J.K., "An Experimental Study of the Development of Longitudinal Vortex Pairs Embedded in a Turbulent Boundary Layer," AIAA 19th Fluid Dynamics, Plasma Dynamics and Lasers Conference, AIAA-87-1309, June 1987.

Pauley, W.R., and Eaton, J.K, "Diverging Boundary Layers with Zero Streamwise Pressure Gradient," 27th Aerospace Sciences Meeting, Reno, NV, AIAA-89-0134, January 9-12, 1989.

Polhamus, E.C., "Application of the Leading-Edge-Suction Analogy of Vortex Lift to the Drag Due to Lift of Sharp-Edge Delta Wings," NASA Technical Note, TN-D-4739, August, 1968.

Simpson, R.L., "Three-dimensional turbulent boundary layers and separation," 33rd Aerospace Sciences Meeting & Exhibit, Reno, NV, AIAA-95-0226, January 9-12, 1995.

Tian, Q., "Near Wall Behavior of Vortical Flow around the Tip of an Axial Pump Rotor Blade", PhD Thesis, VPI&SU, 2006.

Varano, N.D., "Fluid Dynamics and Surface Pressure Fluctuations of Turbulent Boundary Layers Over Sparse Roughness", PhD Thesis, VPI&SU, 2010.

Wendt, B.J., and Hingst, W.R., "Measurements and Modeling of Flow Structure in the Wake of a Low Profile "Wishbone" Vortex Generator," 32th Aerospace Sciences Meeting and Exhibit, Reno, NV, AIAA-94-0620, January 10-13 1994.

Wendt, B.J., and Reichert, B.A., "The Modeling of Symmetric Airfoil Vortex Generators," 34th Aerospace Sciences Meeting and Exhibit, Reno, NV, AIAA-96-0807, January 15-18 1996.

You, D., Wang, M., Mittal, R., and Moin, P., "Large-Eddy Simulations of Longitudinal Vortices Embedded in a Turbulent Boundary Layer," AIAA Journal Vol. 44 No.12 pp. 3032-3039, 2006.

Appendix A. Non-dimensionalized Boundary Layer Profiles

A.1 Introduction

This appendix includes data at the x = 10.5 cm and x = 44.5 cm planes non-dimensionalized on $y^+ = \frac{yu_\tau}{\upsilon}$ and the wall friction velocity, $u_\tau = \sqrt{\frac{\tau_w}{\rho}}$.

.

A.2 Results at x = 10.5 cm Plane

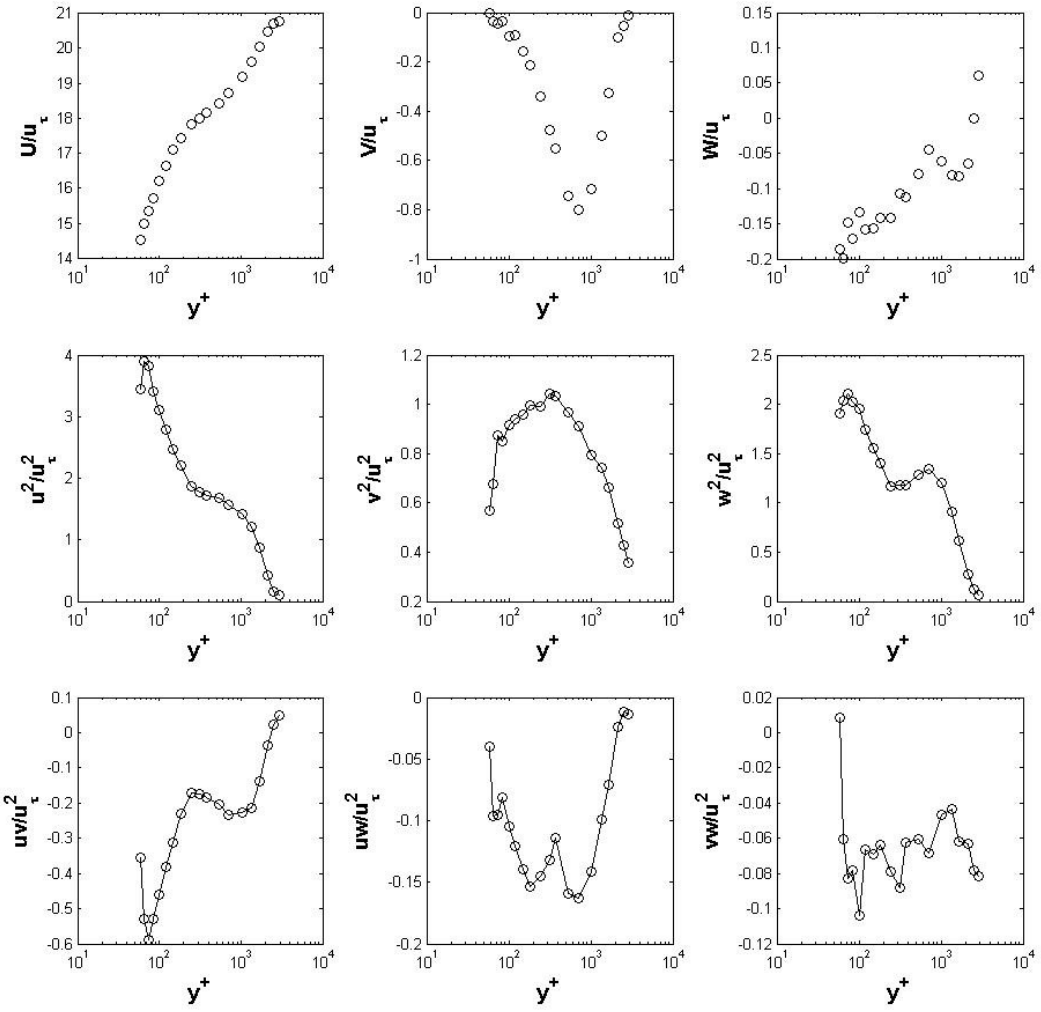

Figure A.2.1 Mean Velocities and Reynolds Stresses, z = 0.0 cm

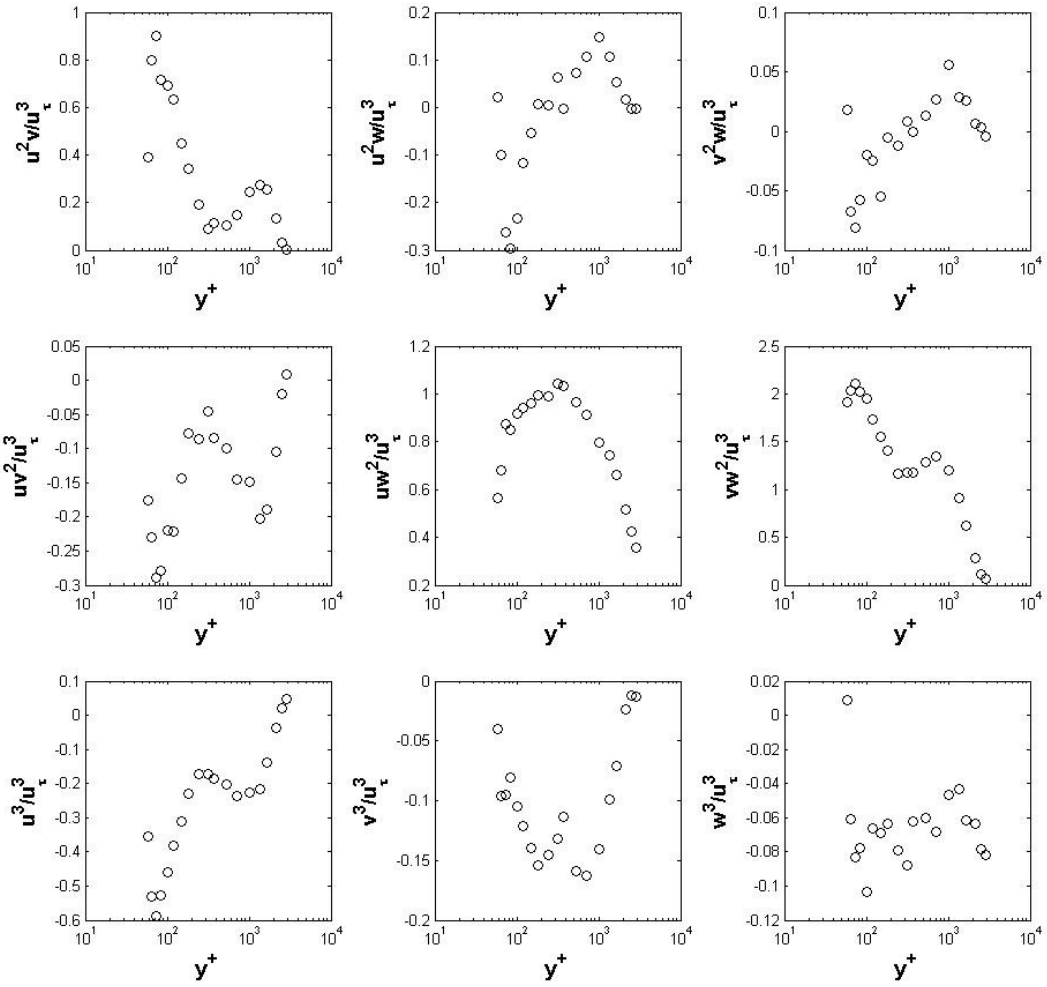

Figure A.2.2 Triple Products, z = 0.0 cm

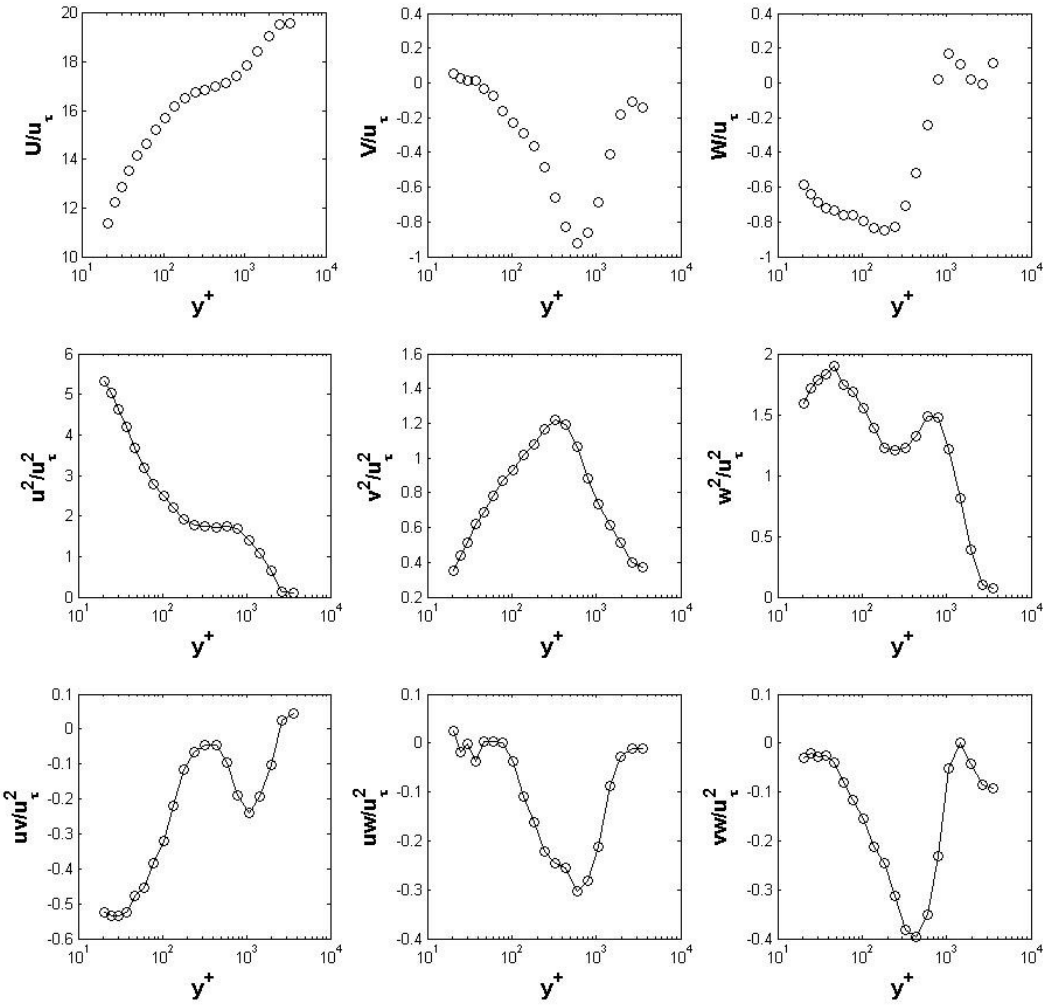

Figure A.2.3 Mean Velocities and Reynolds Stresses, z = 0.5 cm

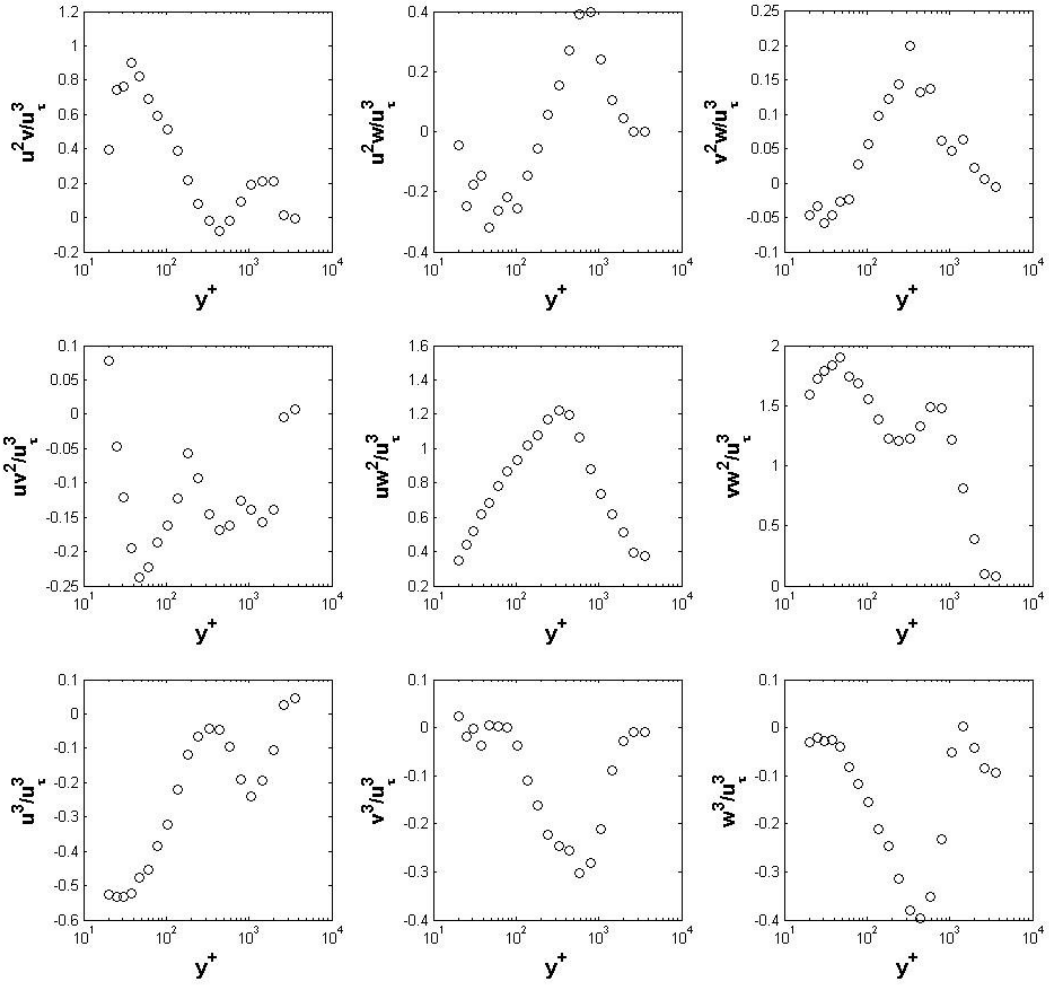

Figure A.2.4 Triple Products, z = 0.5 cm

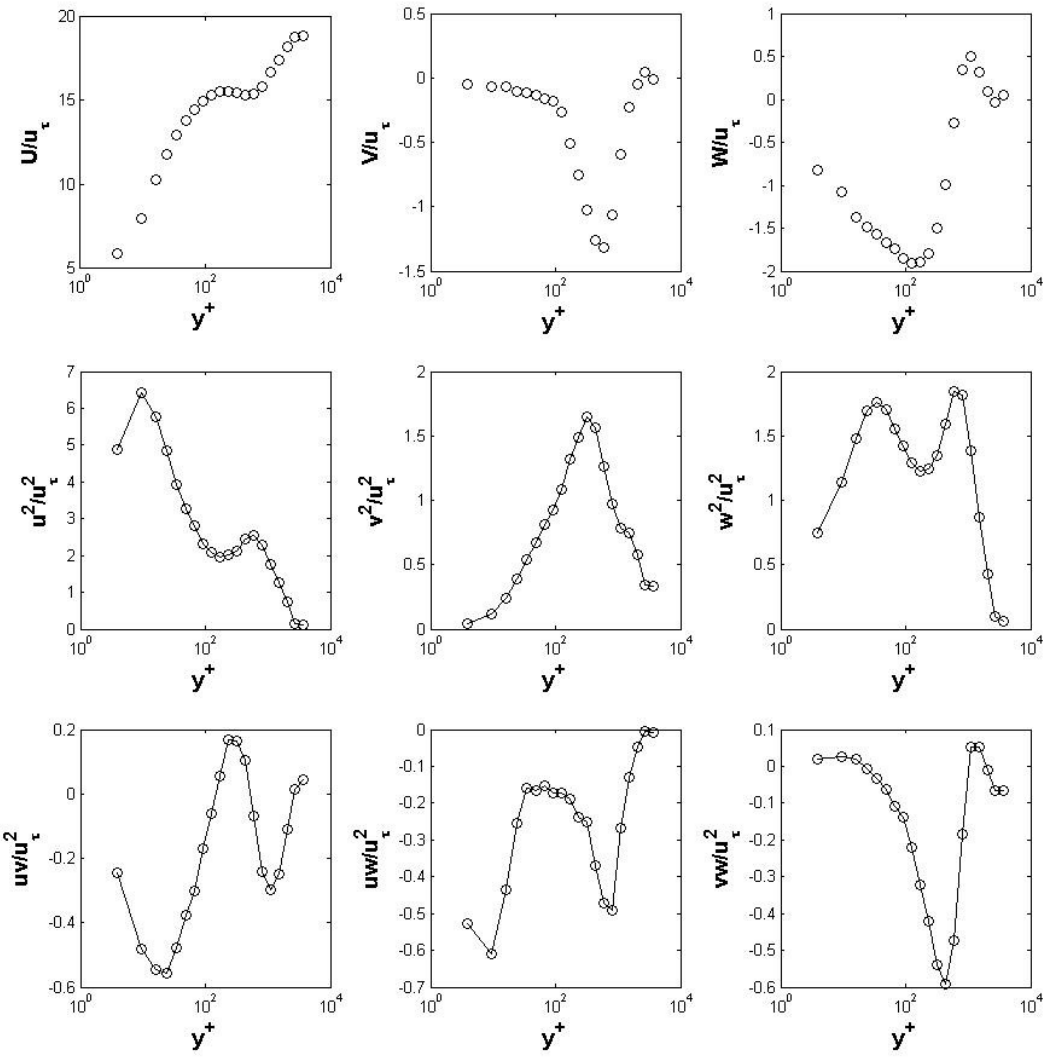

Figure A.2.5 Mean Velocities and Reynolds Stresses, z = 1.0 cm

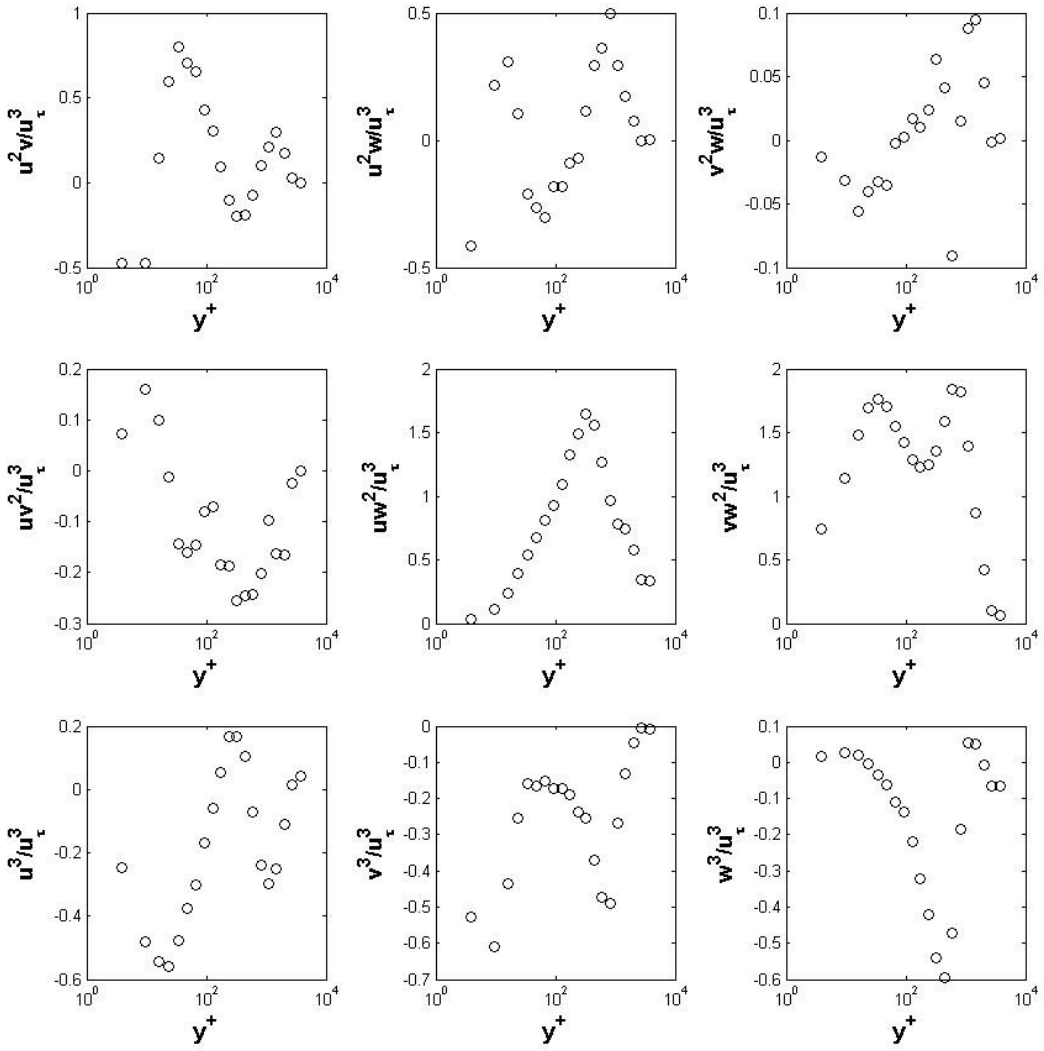

Figure A.2.6 Triple Products, z = 1.0 cm

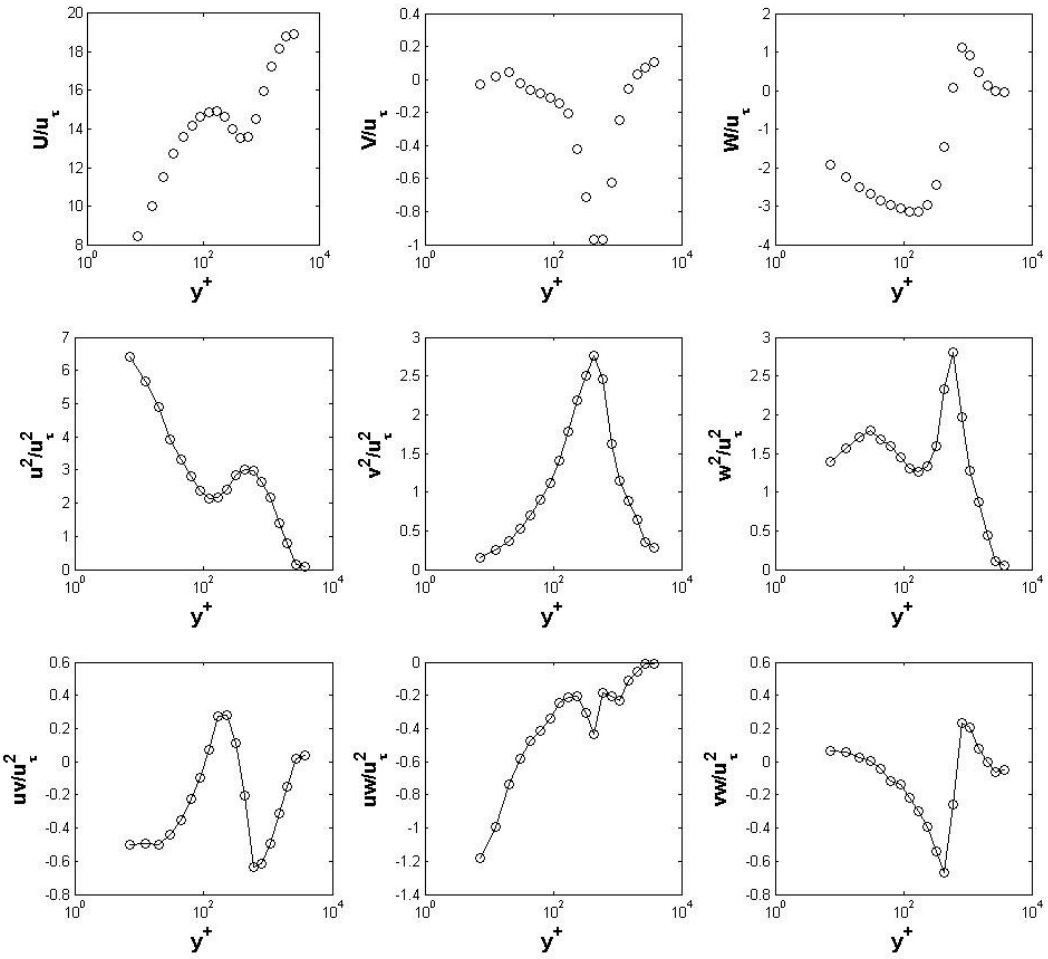

Figure A.2.7 Mean Velocities and Reynolds Stresses, z = 1.5 cm

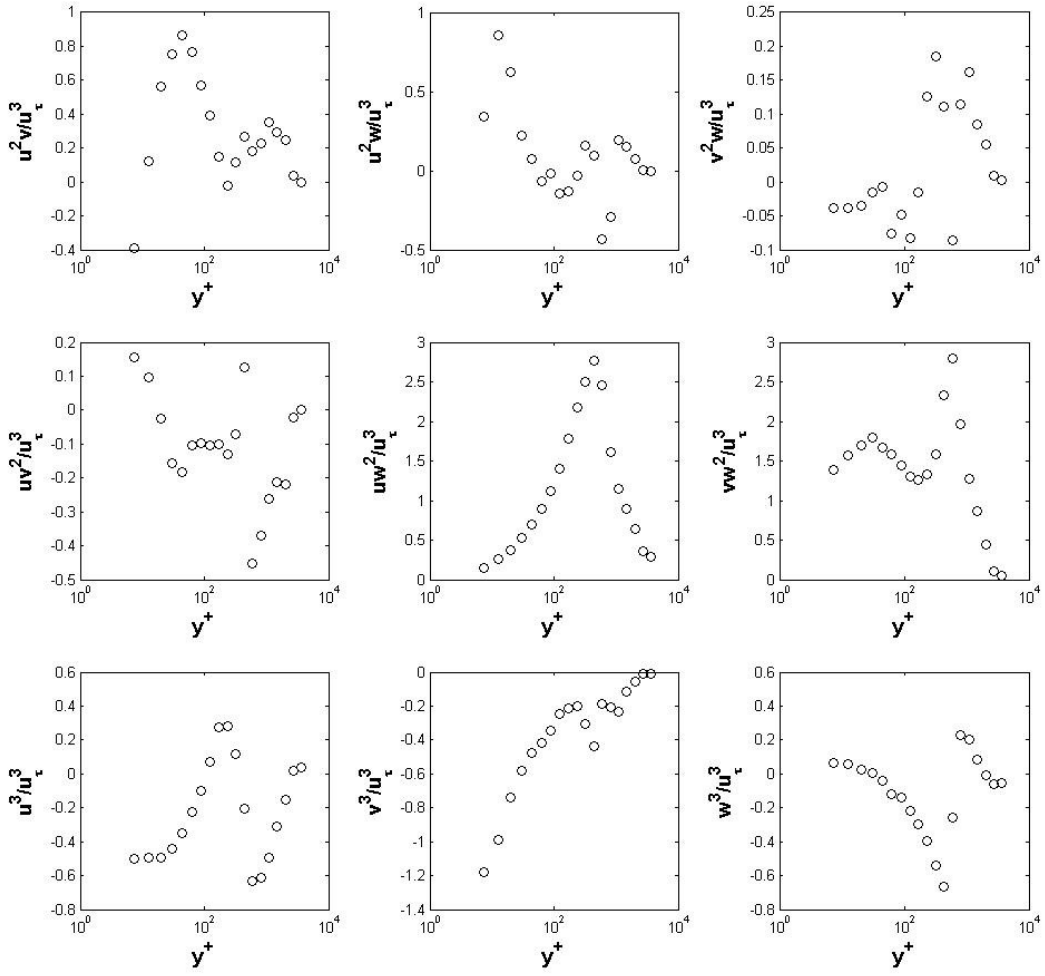

Figure A.2.8 Triple Products, z = 1.5 cm

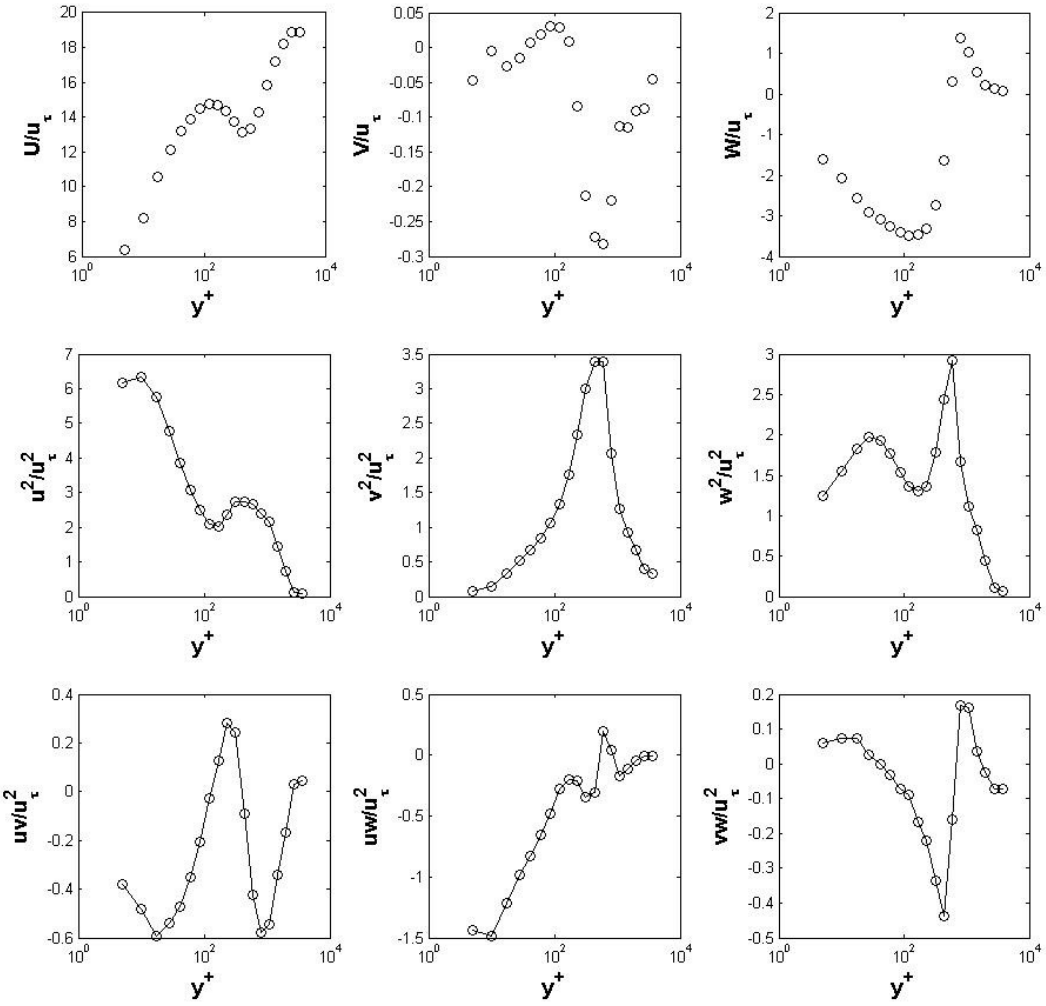

Figure A.2.9 Mean Velocities and Reynolds Stresses, z = 1.75 cm

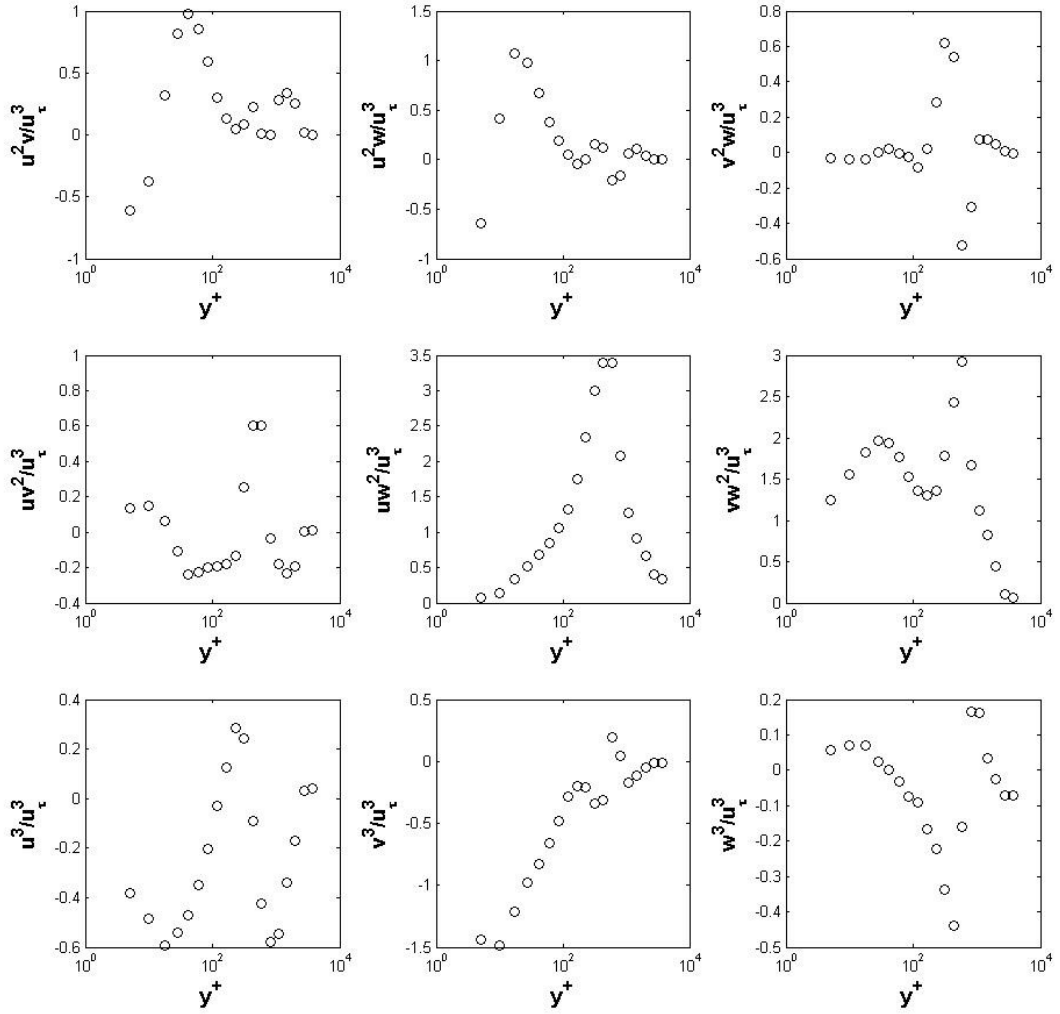

Figure A.2.10 Triple Products, z = 1.75 cm

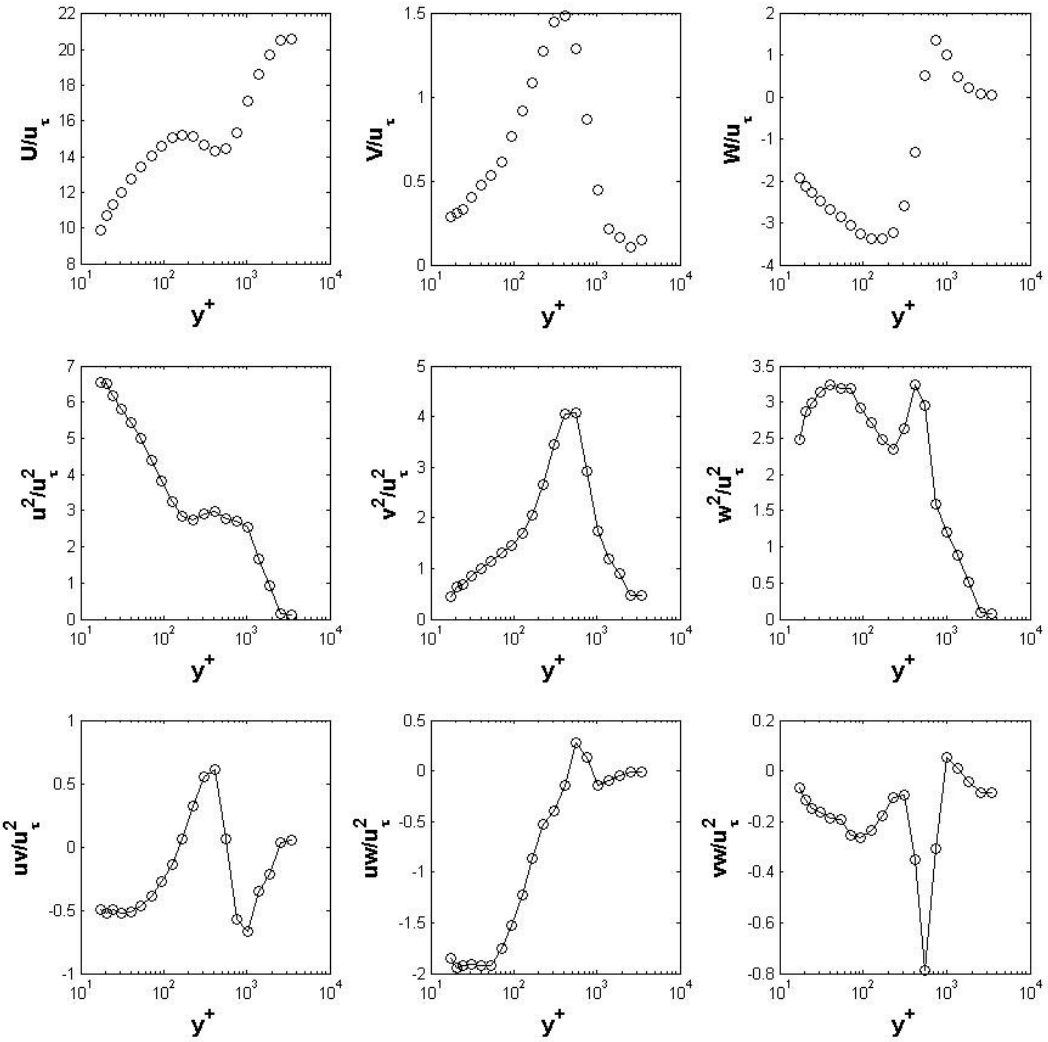

Figure A.2.11 Mean Velocities and Reynolds Stresses, z = 2.0 cm

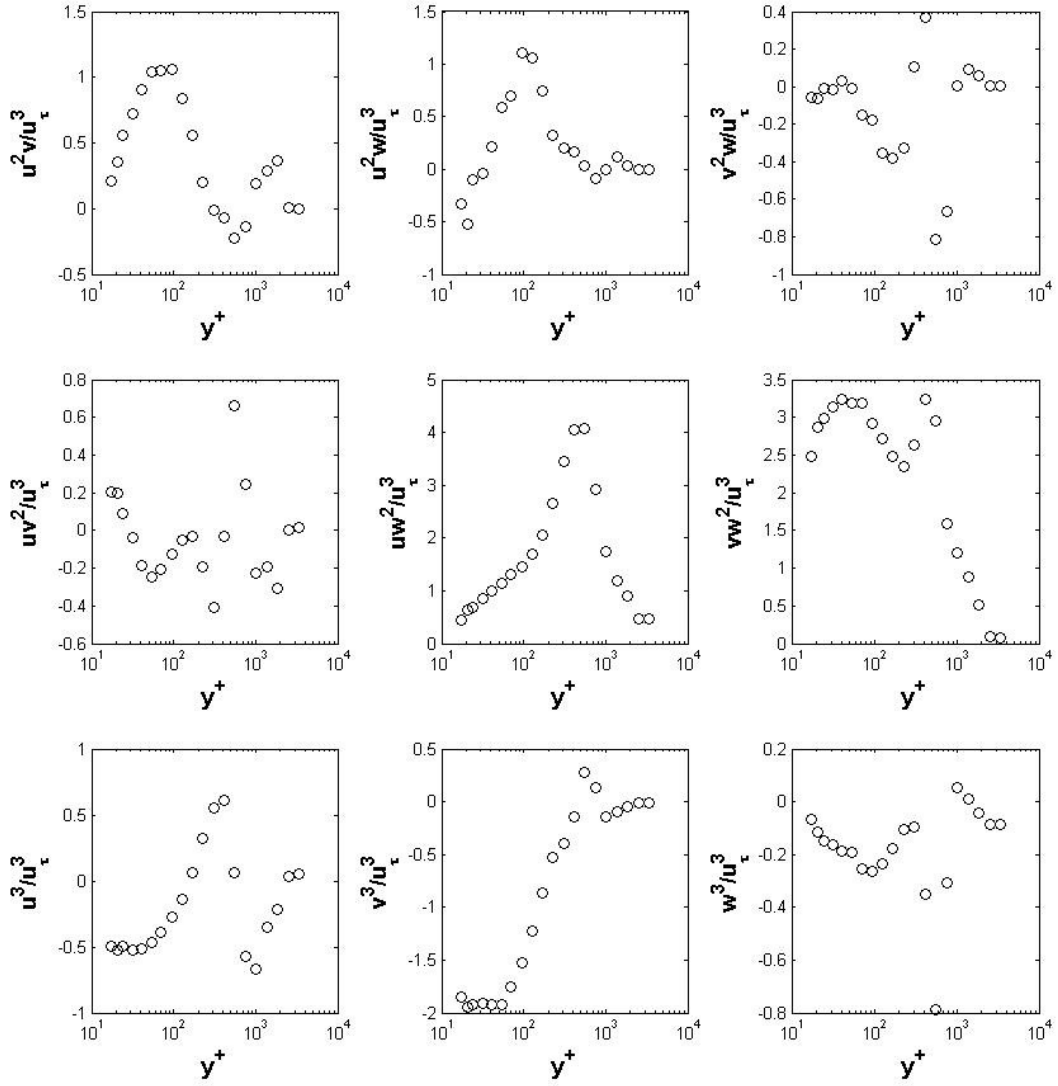

Figure A.2.12 Triple Products, z = 2.0 cm

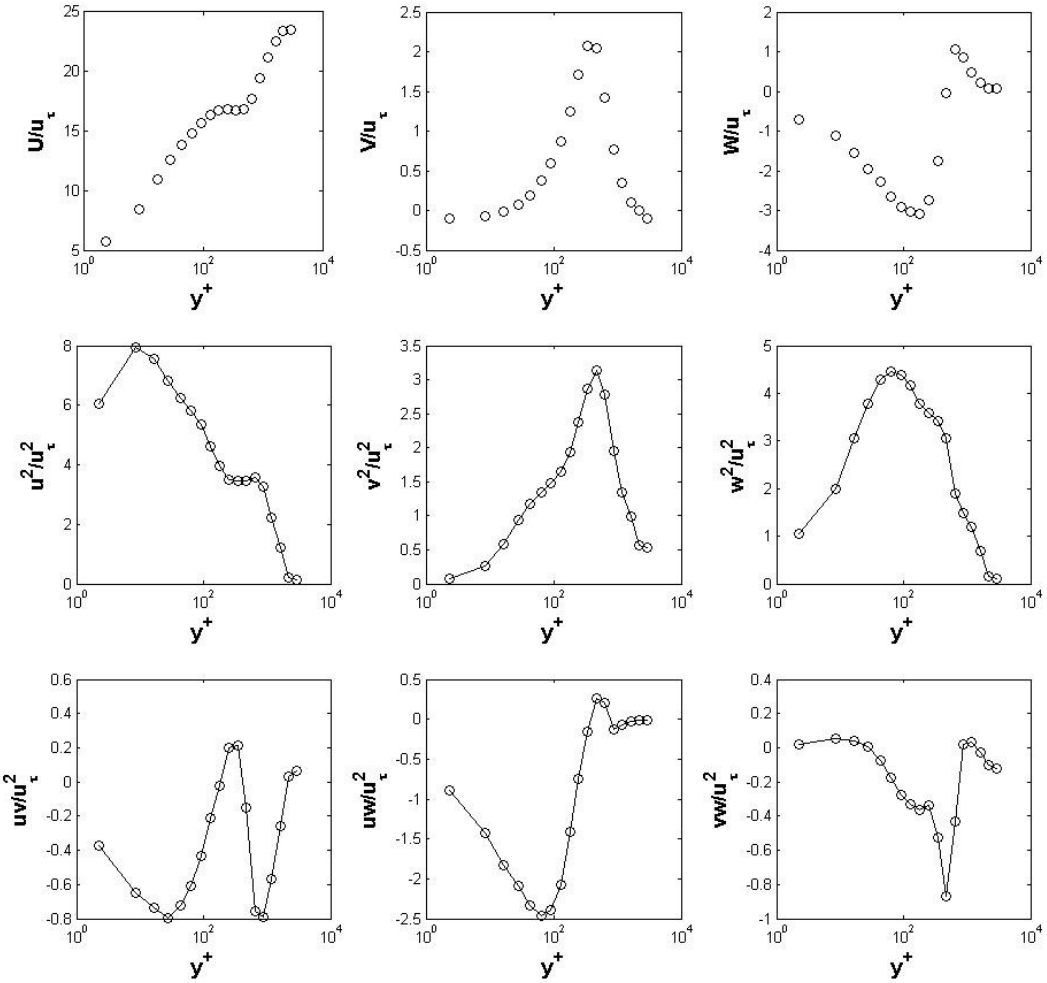

Figure A.2.13 Mean Velocities and Reynolds Stresses, z = 2.25 cm

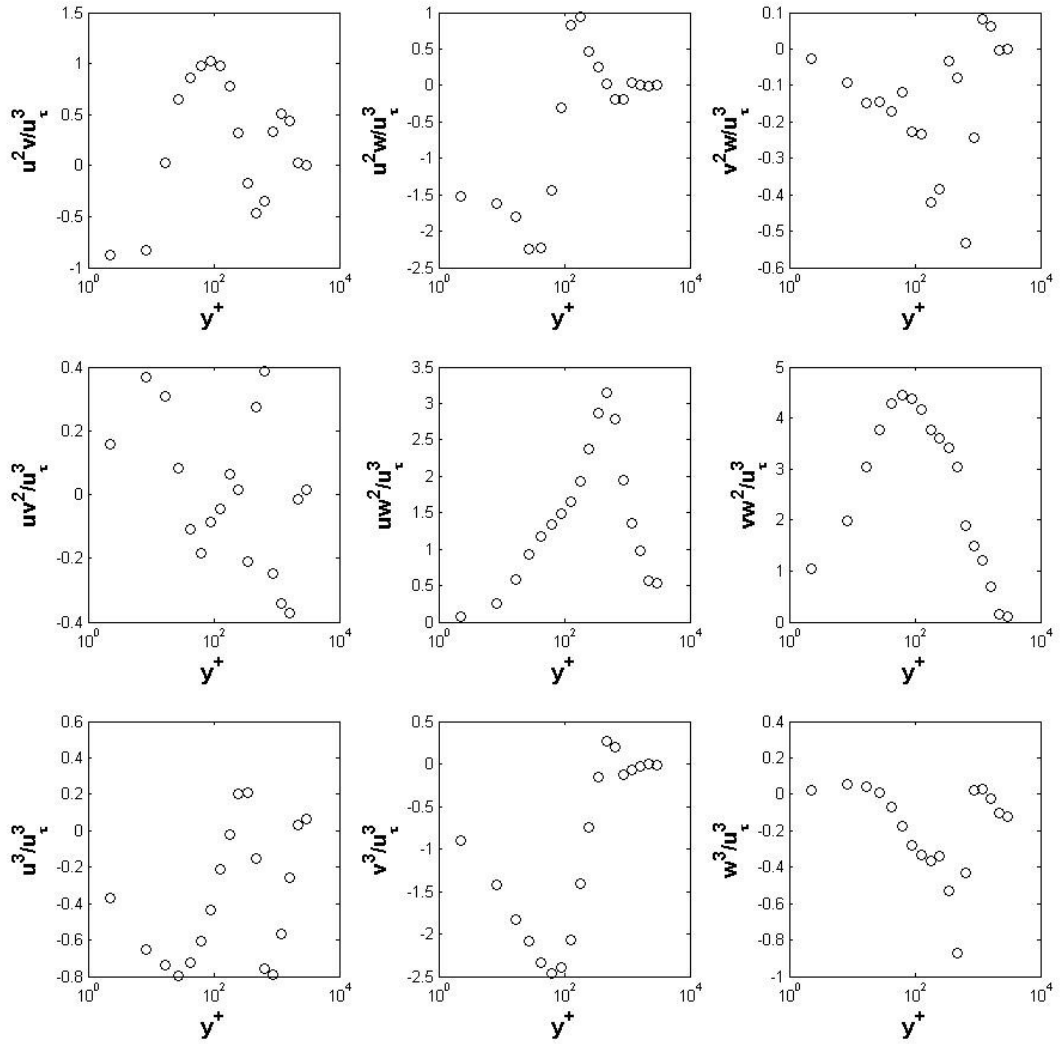

Figure A.2.14 Triple Products, z =2.25 cm

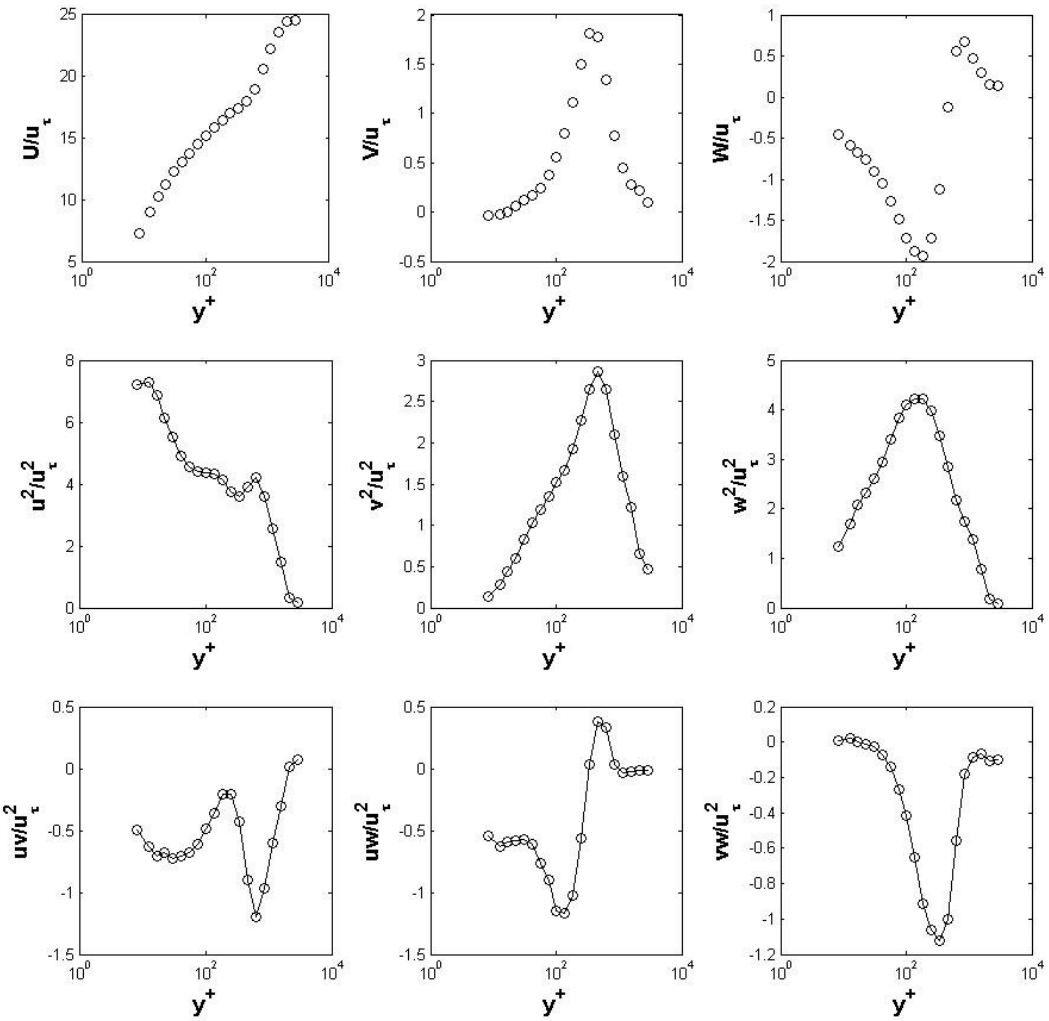

Figure A.2.15 Mean Velocities and Reynolds Stresses, z = 2.5 cm

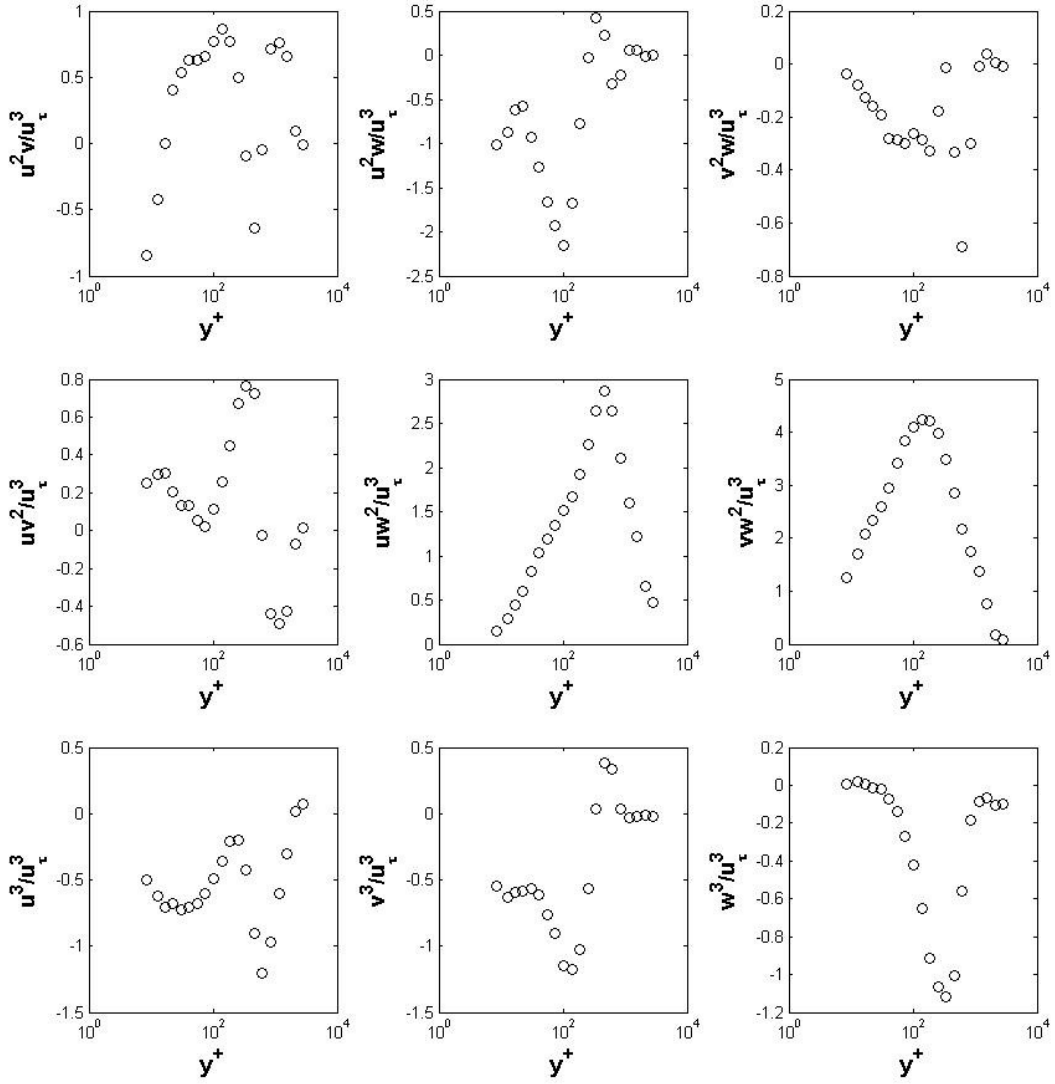

Figure A.2.16 Triple Products, z = 2.5 cm

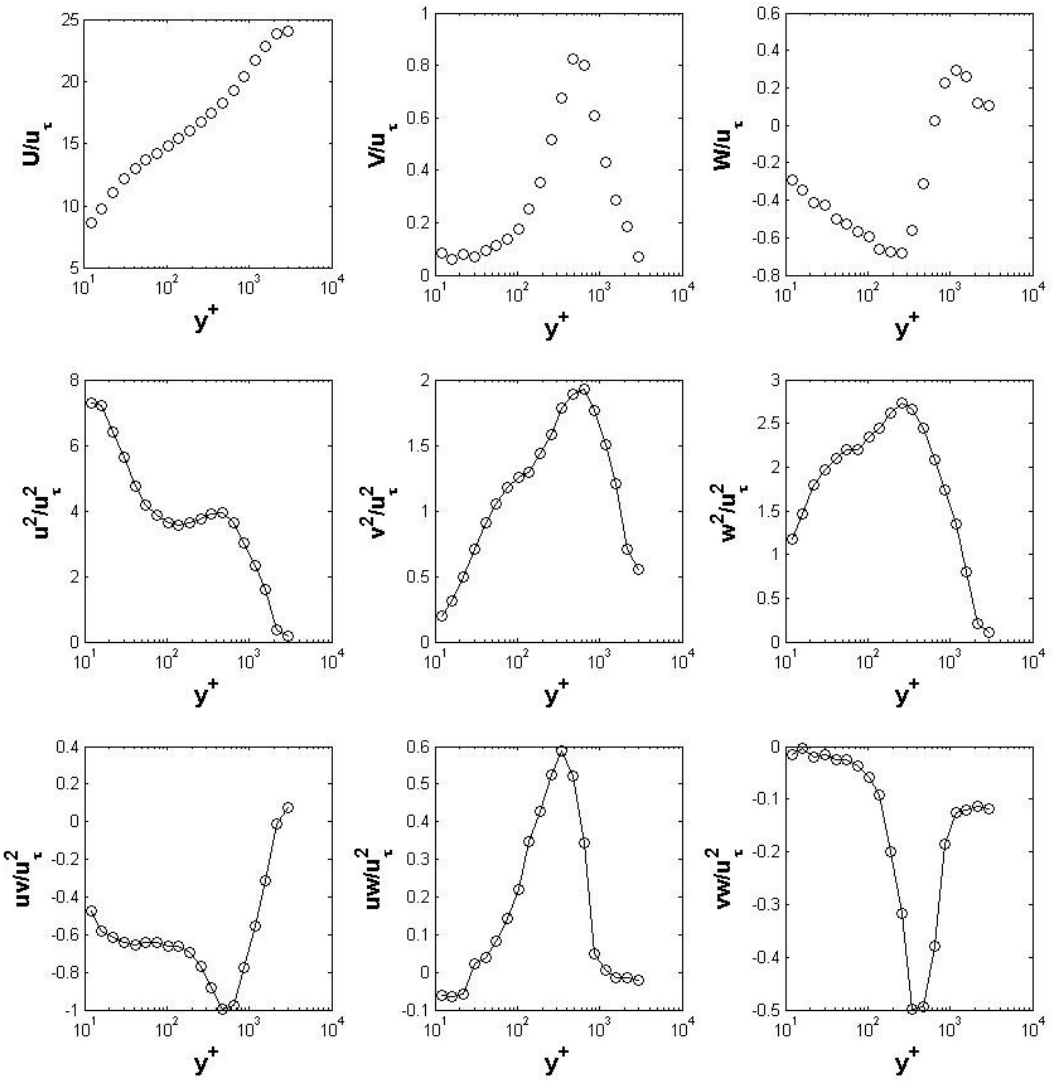

Figure A.2.17 Mean Velocities and Reynolds Stresses, z = 3.0 cm

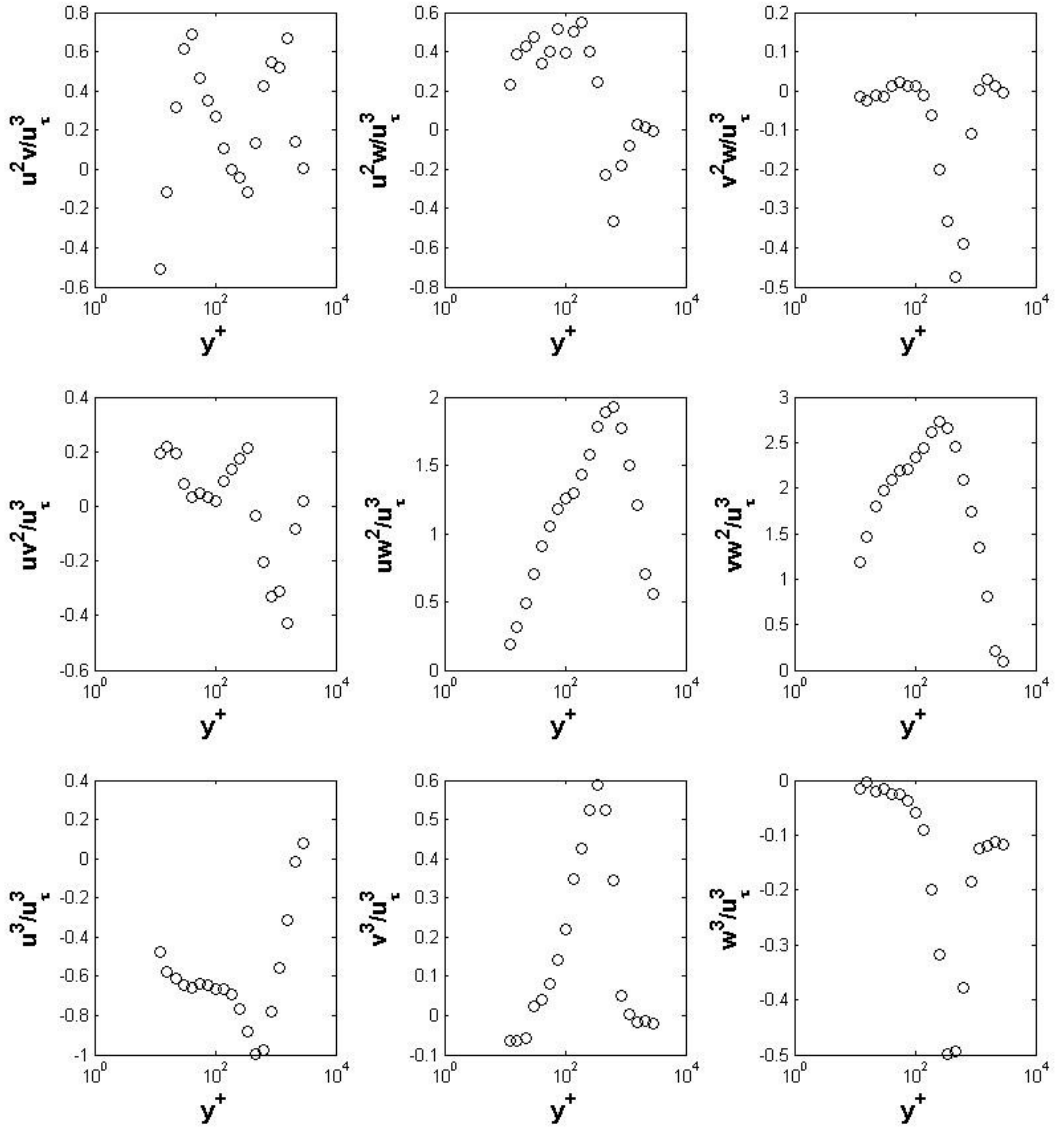

Figure A.2.18 Triple Products, z = 3.0 cm

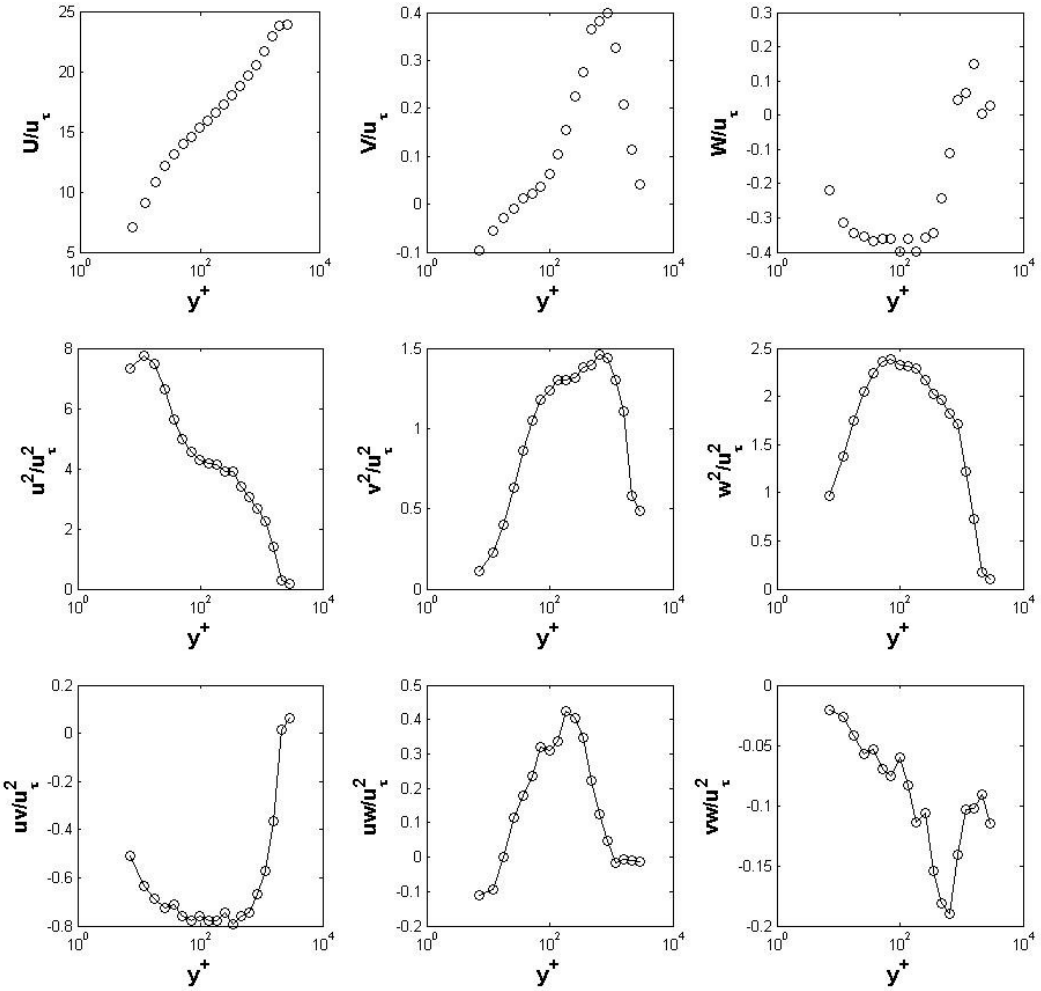

Figure A.2.19 Mean Velocities and Reynolds Stresses, z = 3.5 cm

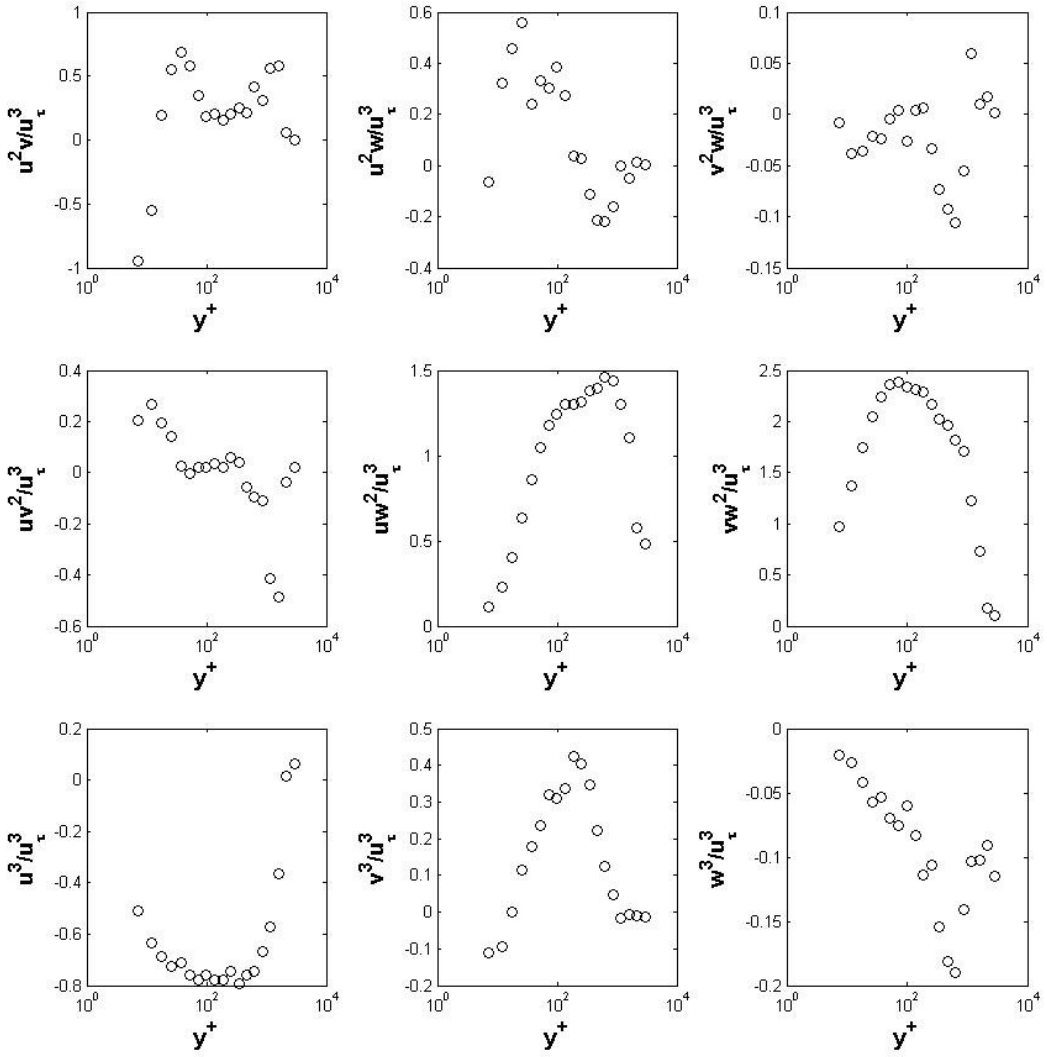

Figure A.2.20 Triple Products, z = 3.5 cm

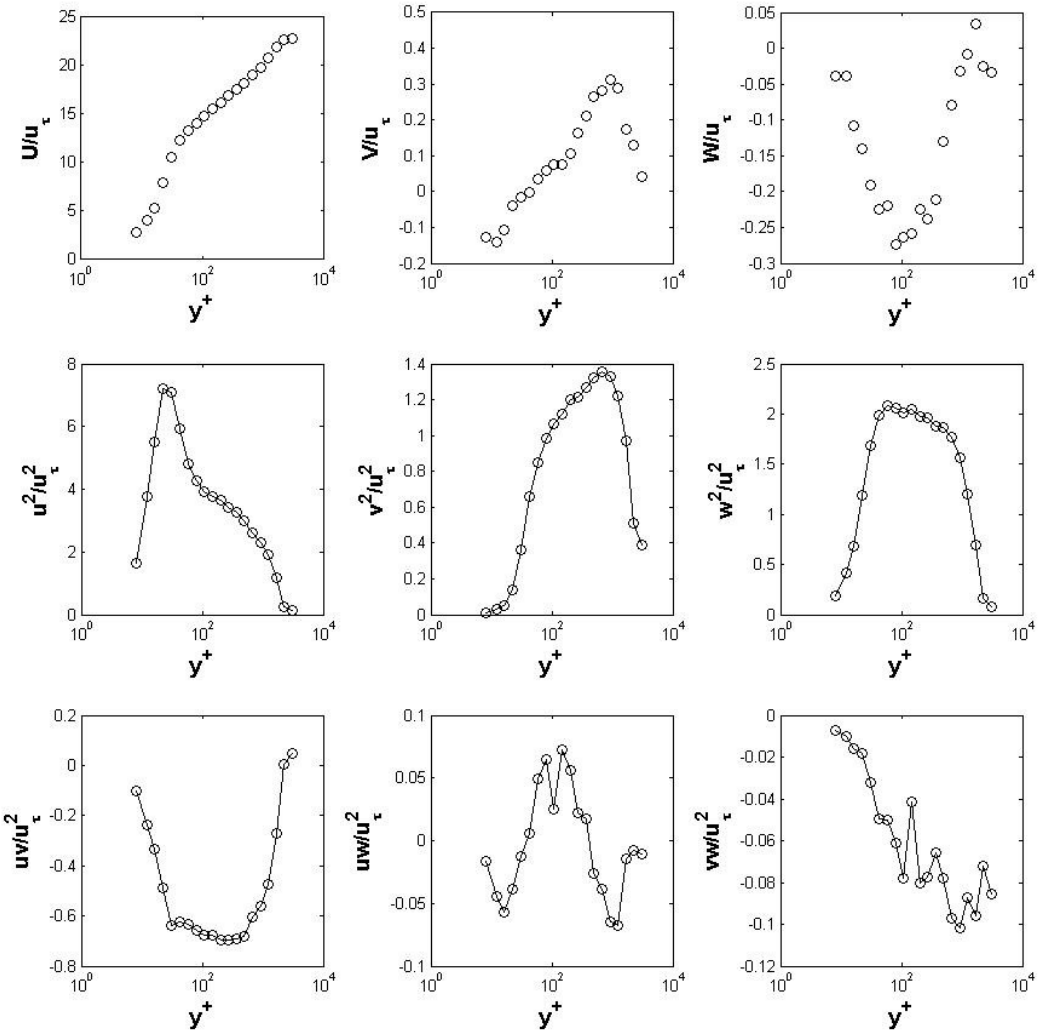

Figure A.2.21 Mean Velocities and Reynolds Stresses, z = 4.0 cm

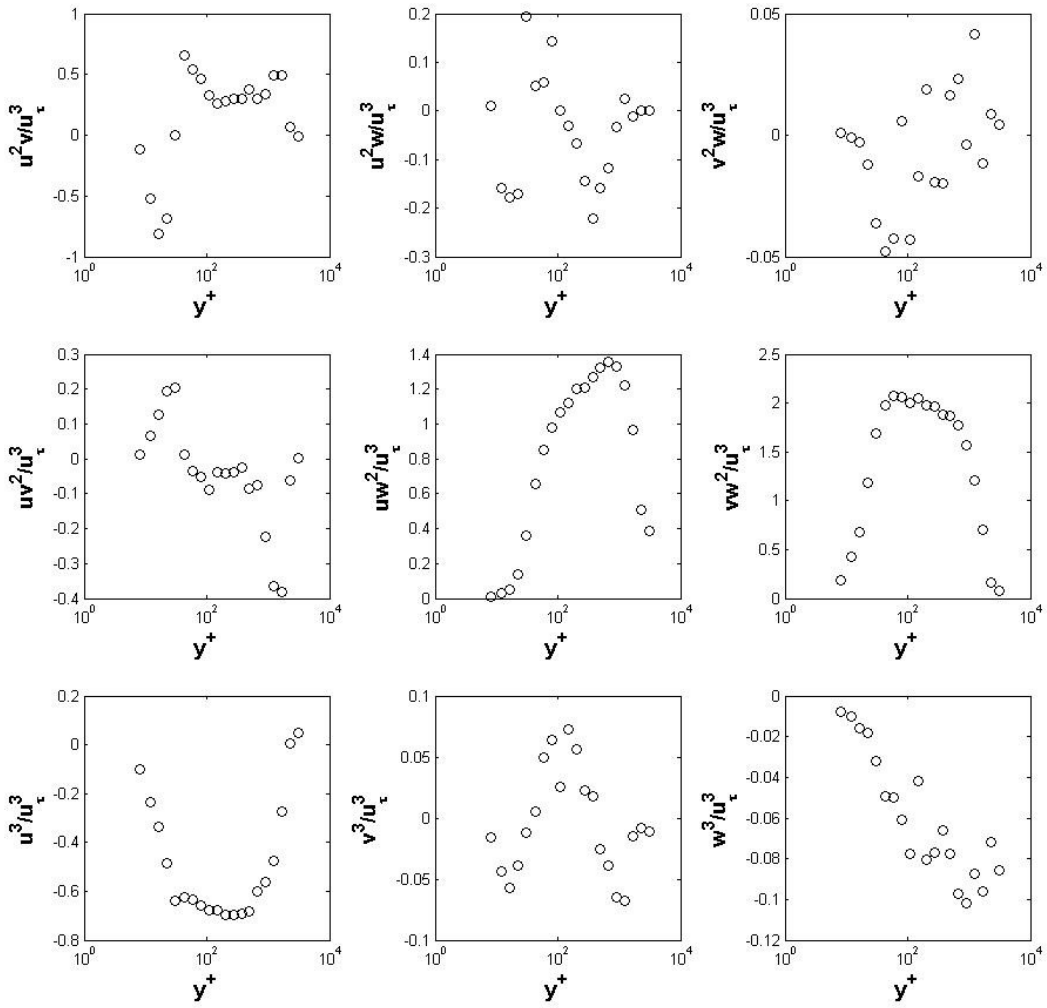

Figure A.2.22 Triple Products, z = 4.0 cm

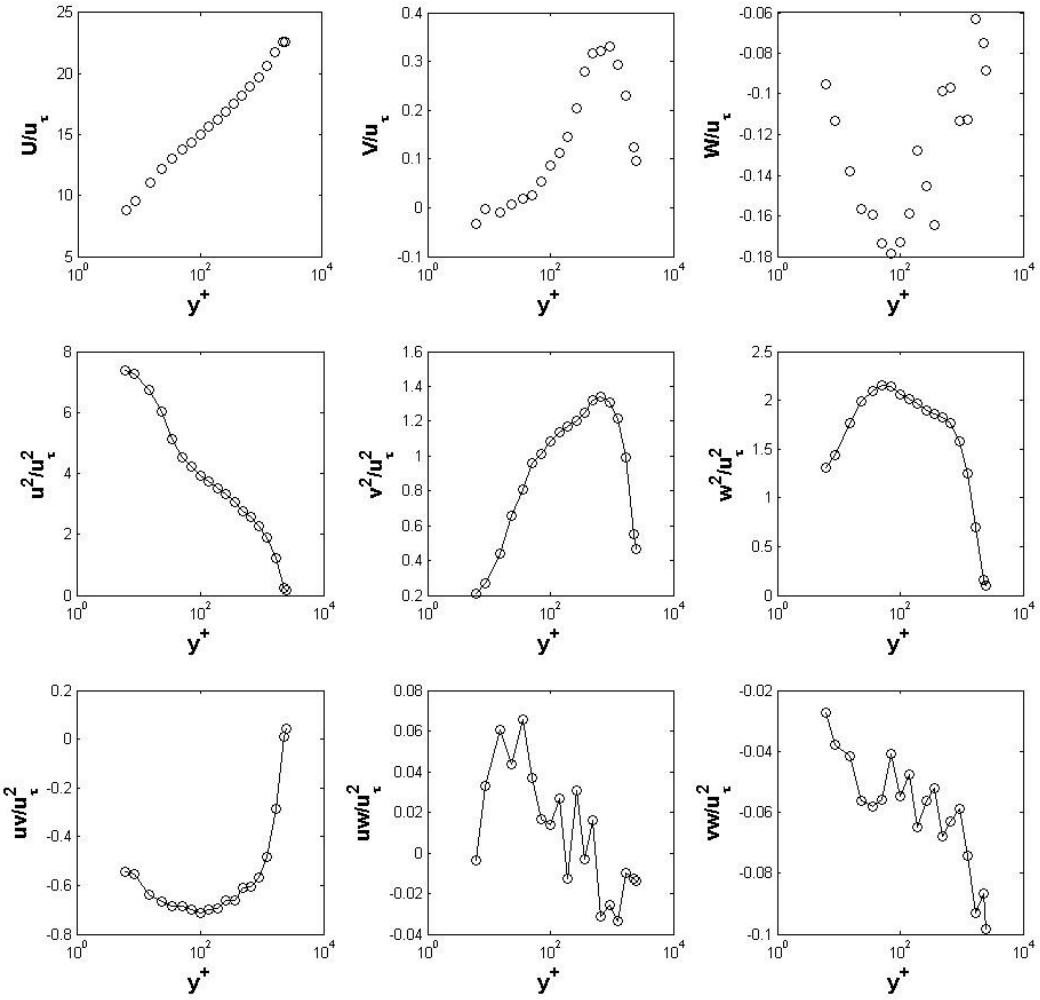

Figure A.2.23 Mean Velocities and Reynolds Stresses, z = 4.5 cm

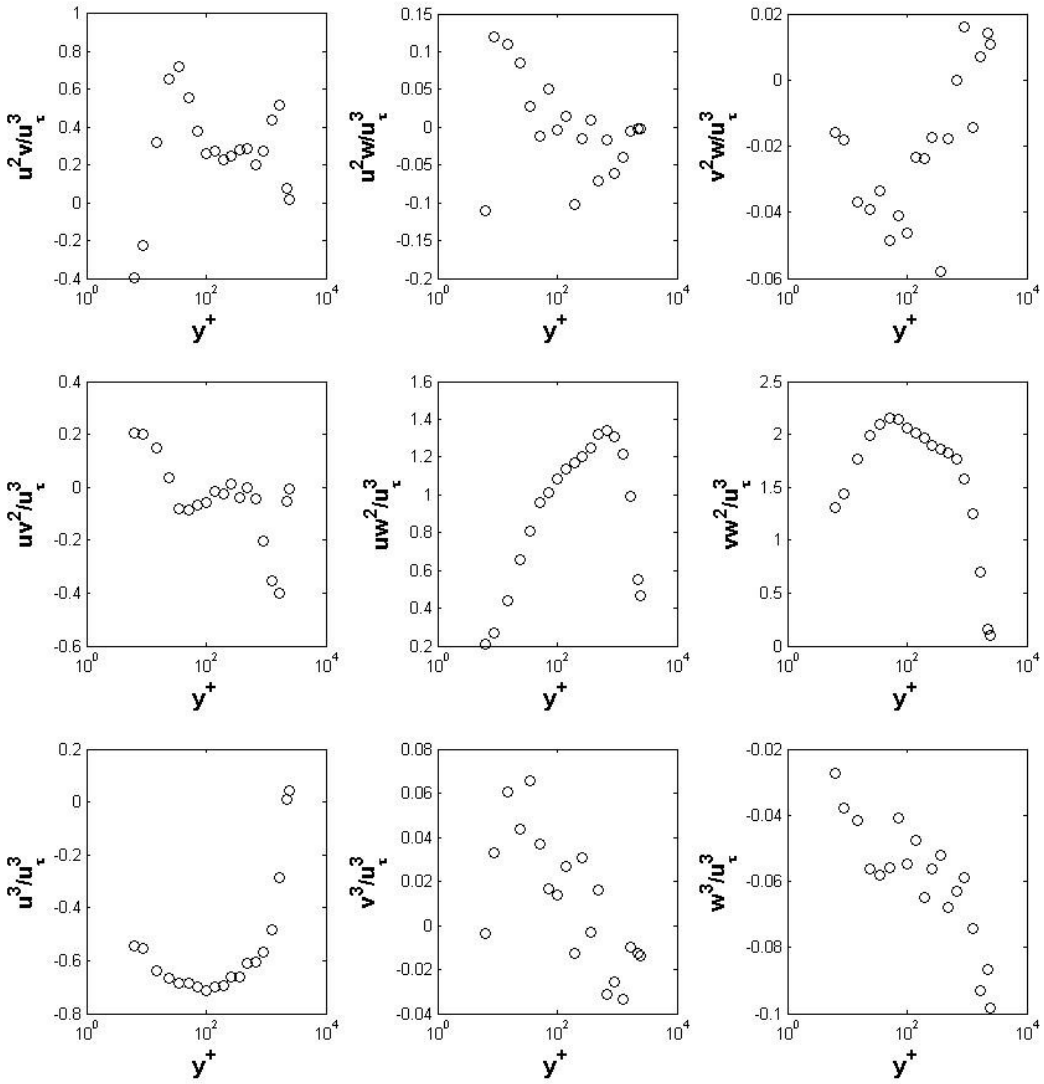

Figure A.2.24 Triple Products, z = 4.5 cm

A.3 Results at x = 44.5 cm Plane

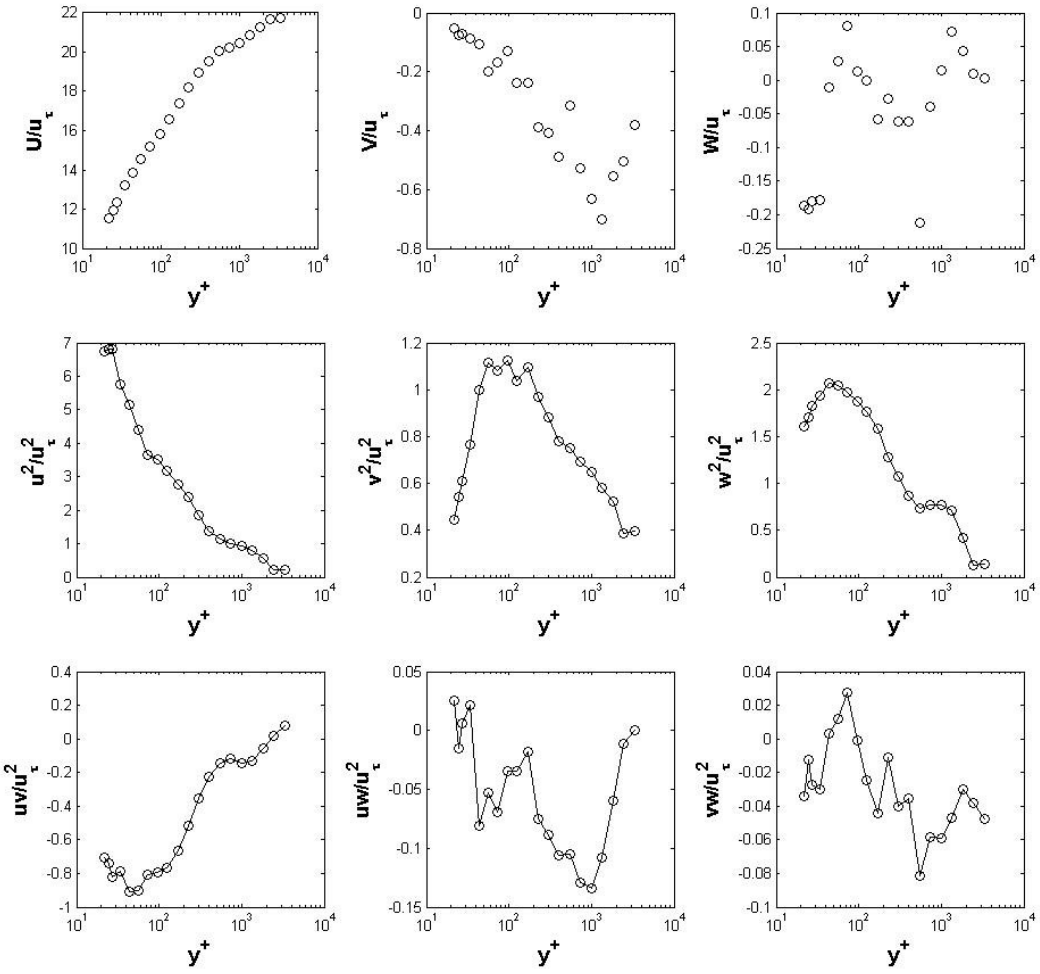

Figure A.3.1 Mean Velocities and Reynolds Stresses, z = 0.0 cm

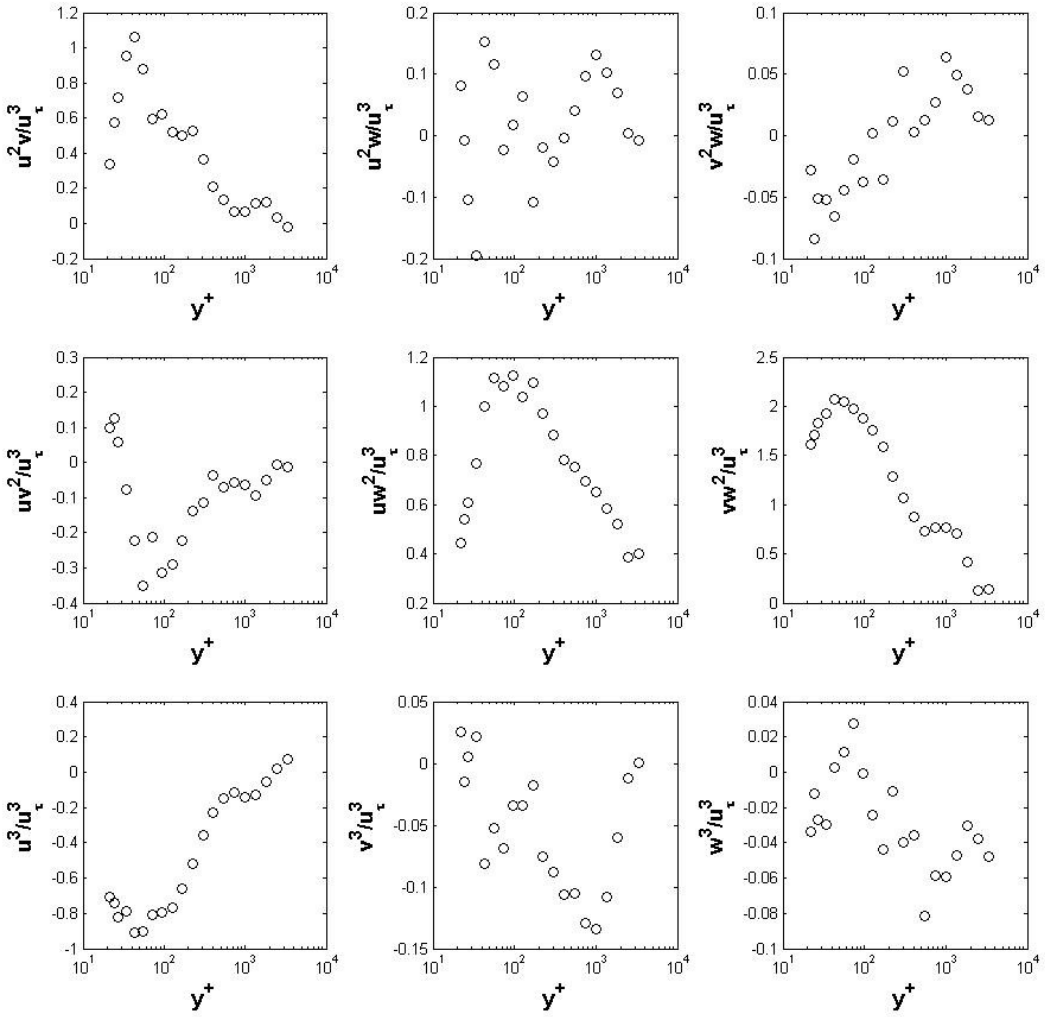

Figure A.3.2 Triple Products, z = 0.0 cm

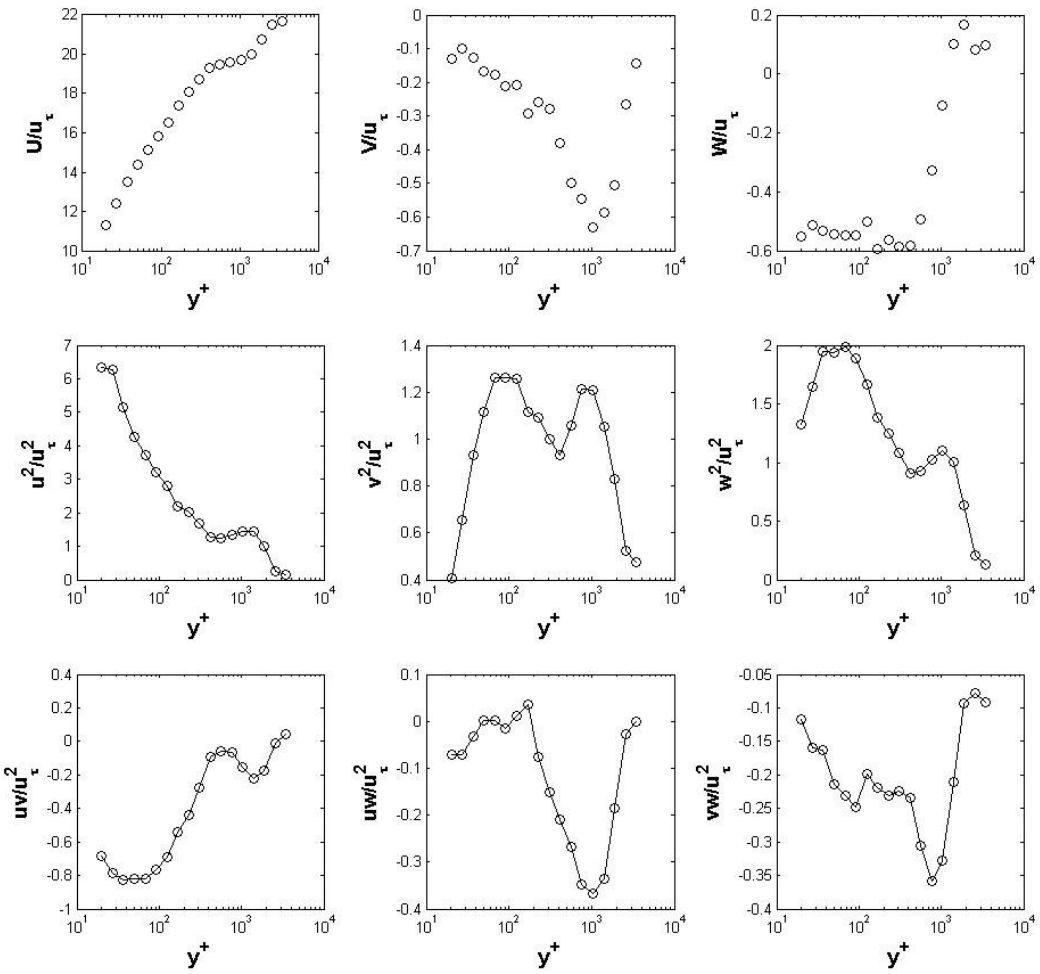

Figure A.3.3 Mean Velocities and Reynolds Stresses, z = 1.0 cm

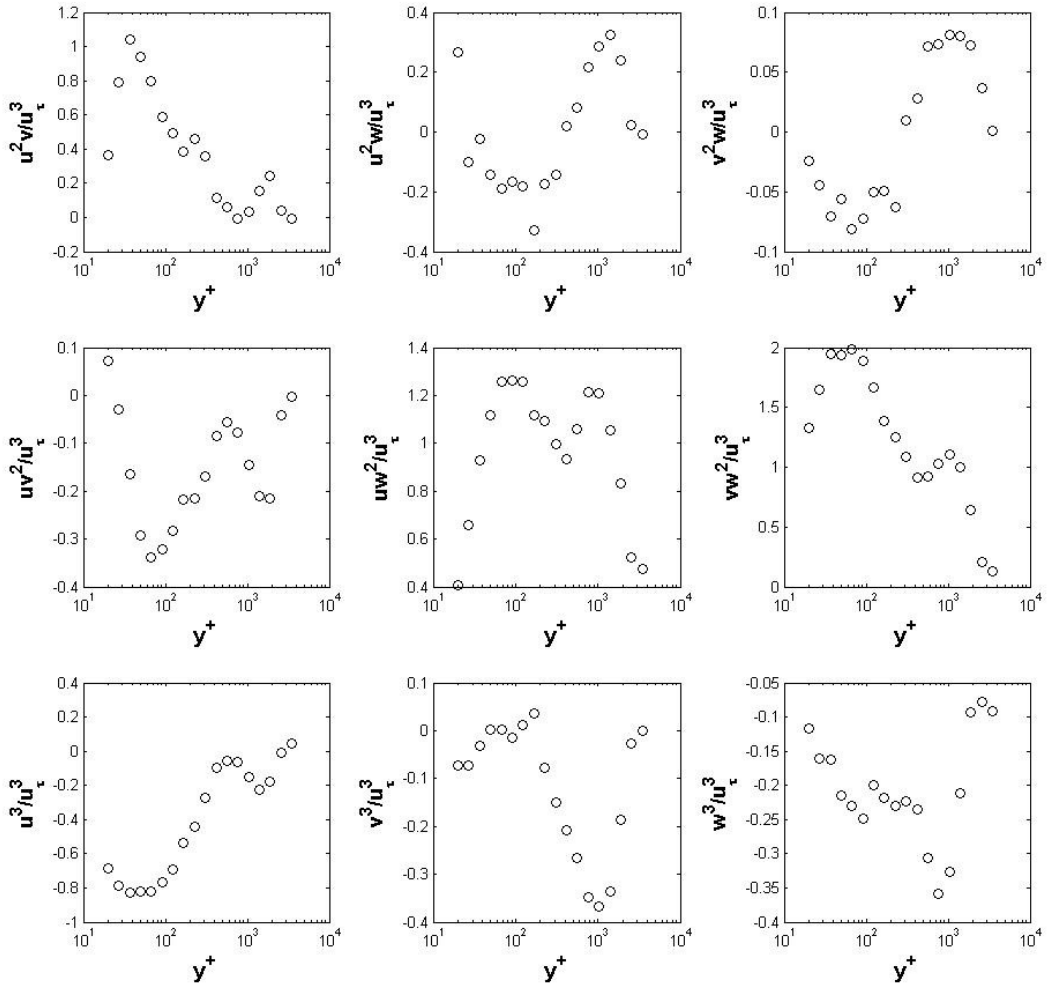

Figure A.3.4 Triple Products, z = 1.0 cm

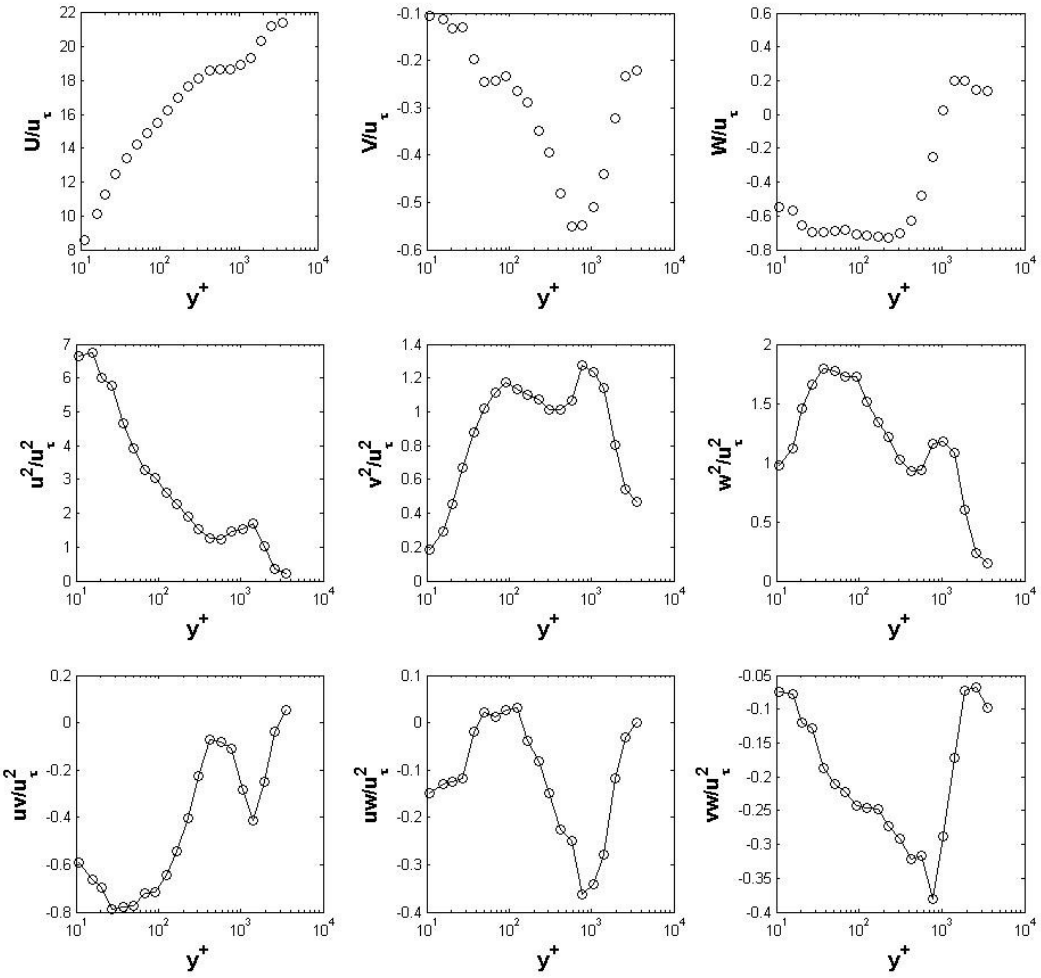

Figure A.3.5 Mean Velocities and Reynolds Stresses, z = 1.5 cm

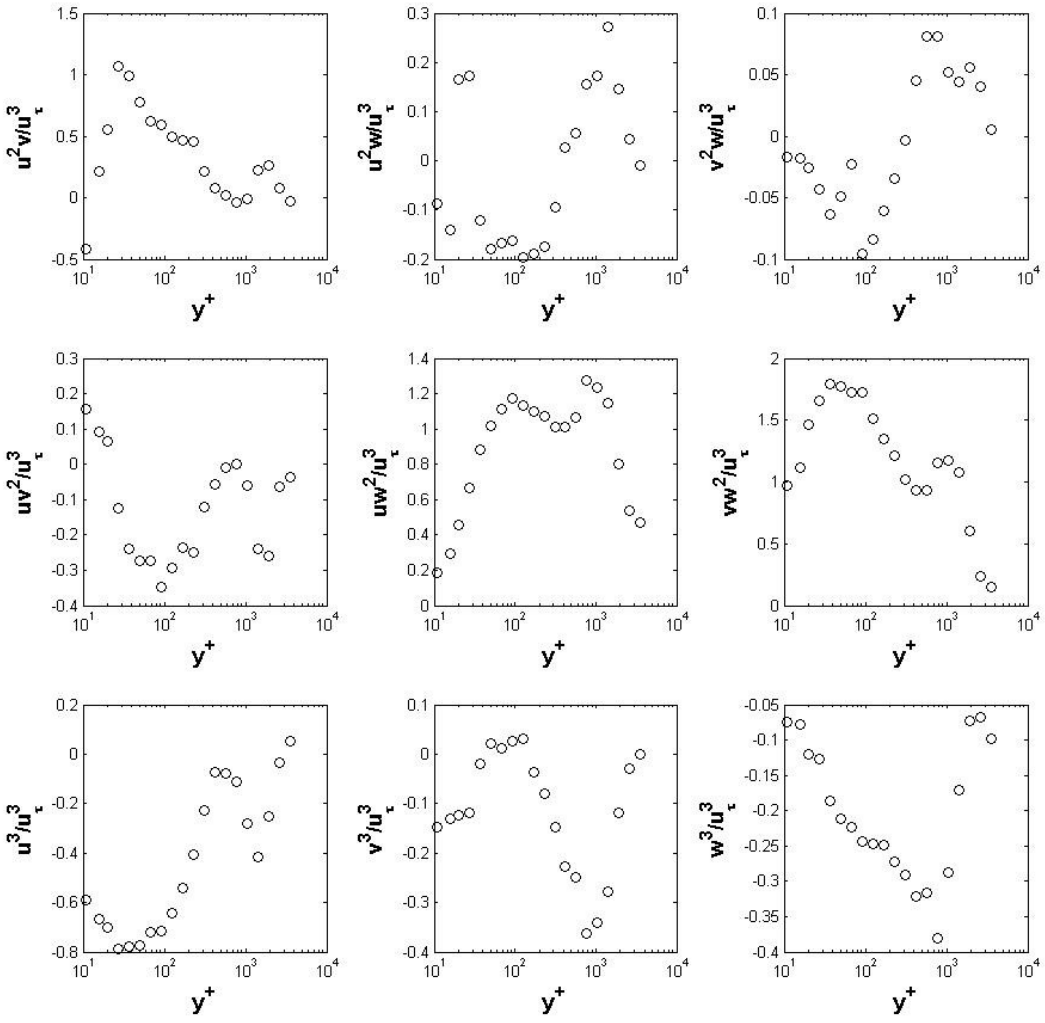

Figure A.3.6 Triple Products, z = 1.5 cm

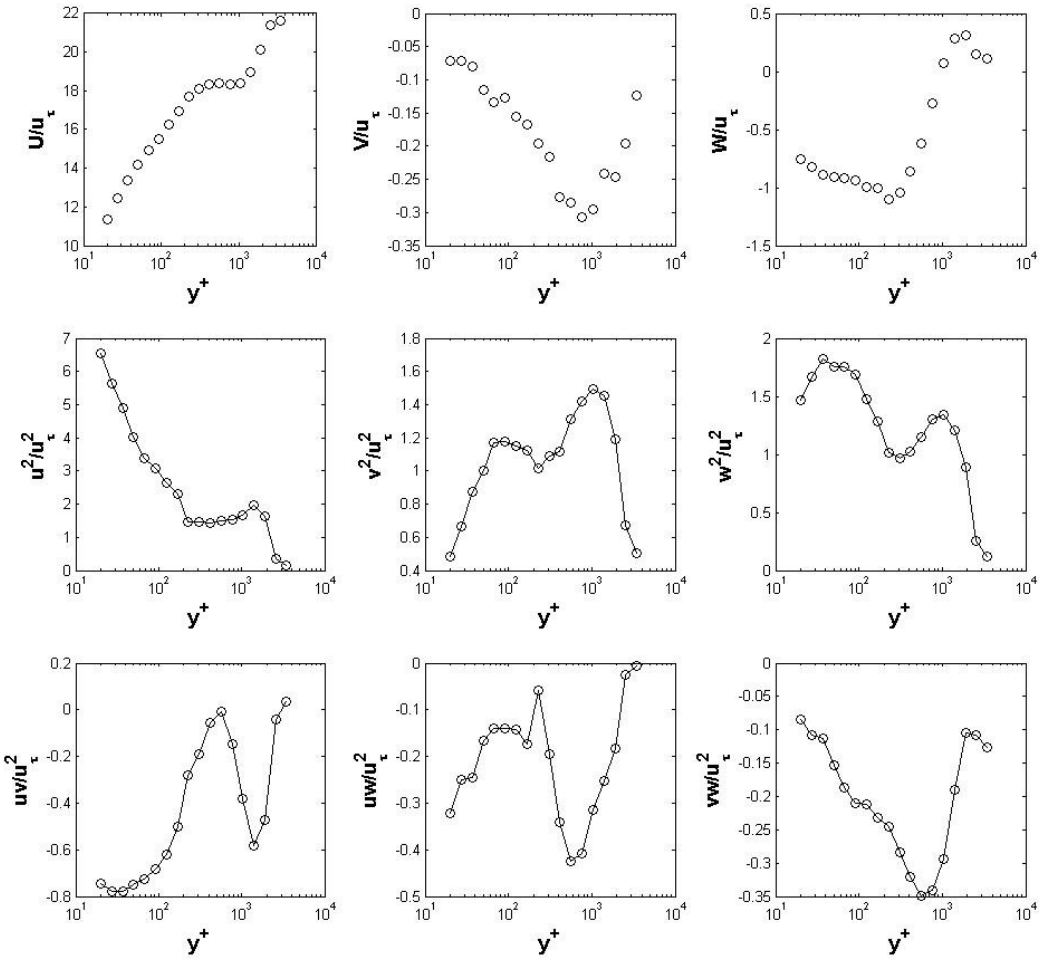

Figure A.3.7 Mean Velocities and Reynolds Stresses, z = 2.0 cm

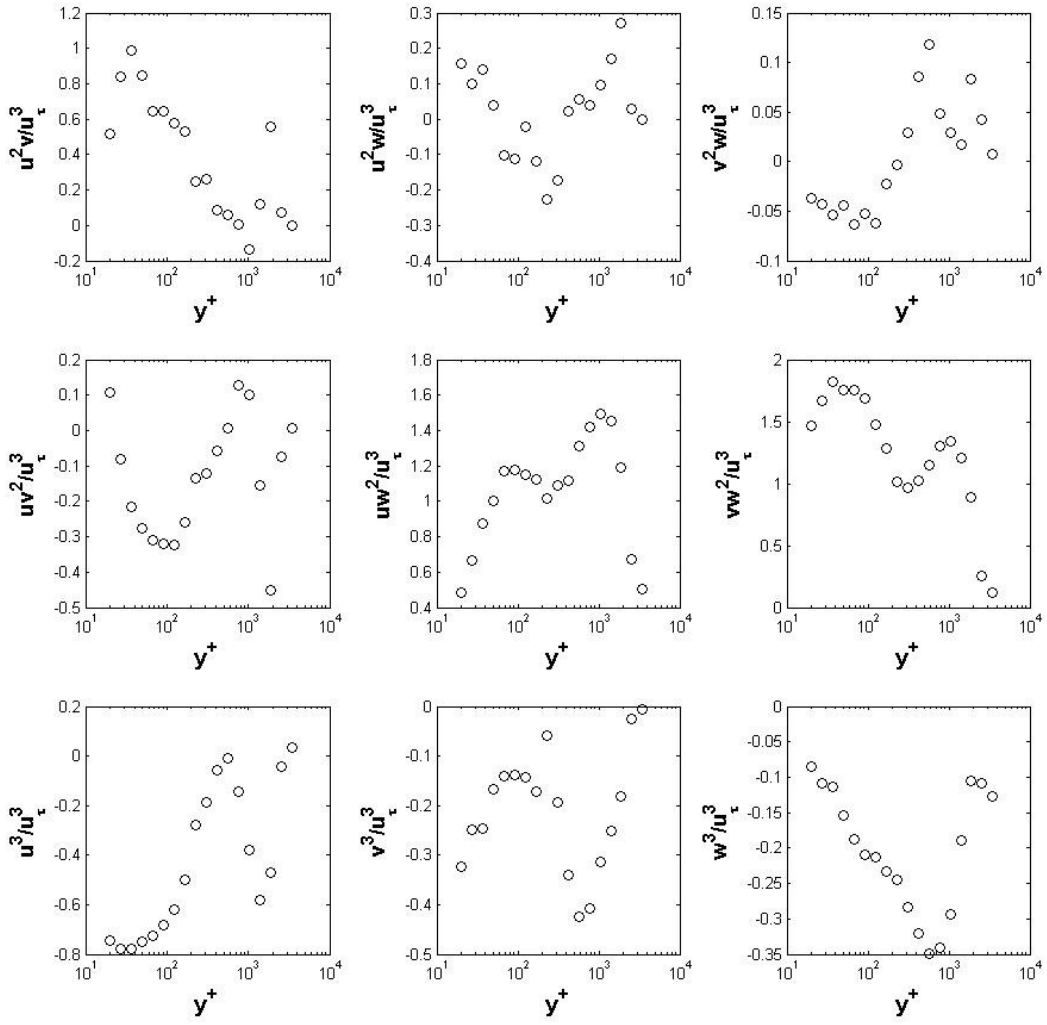

Figure A.3.8 Triple Products, z = 2.0 cm

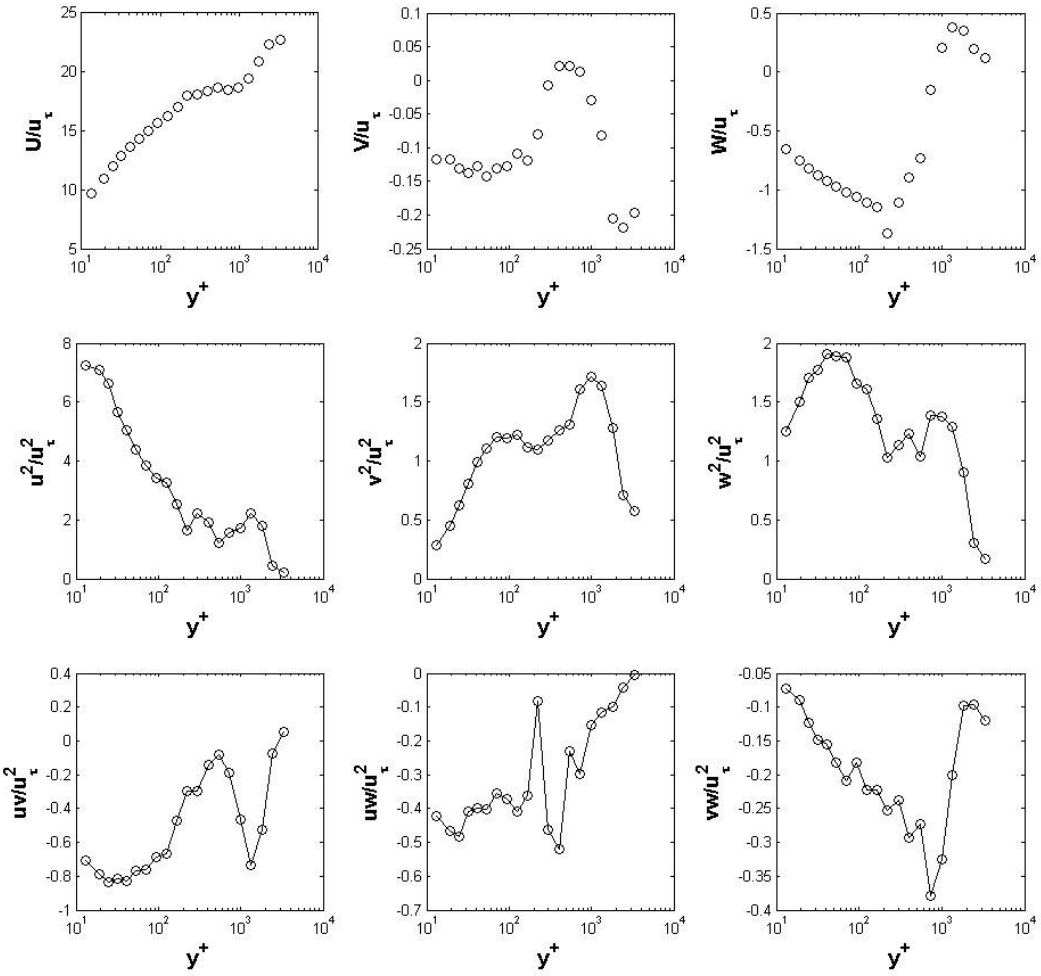

Figure A.3.9 Mean Velocities and Reynolds Stresses, z = 2.5 cm

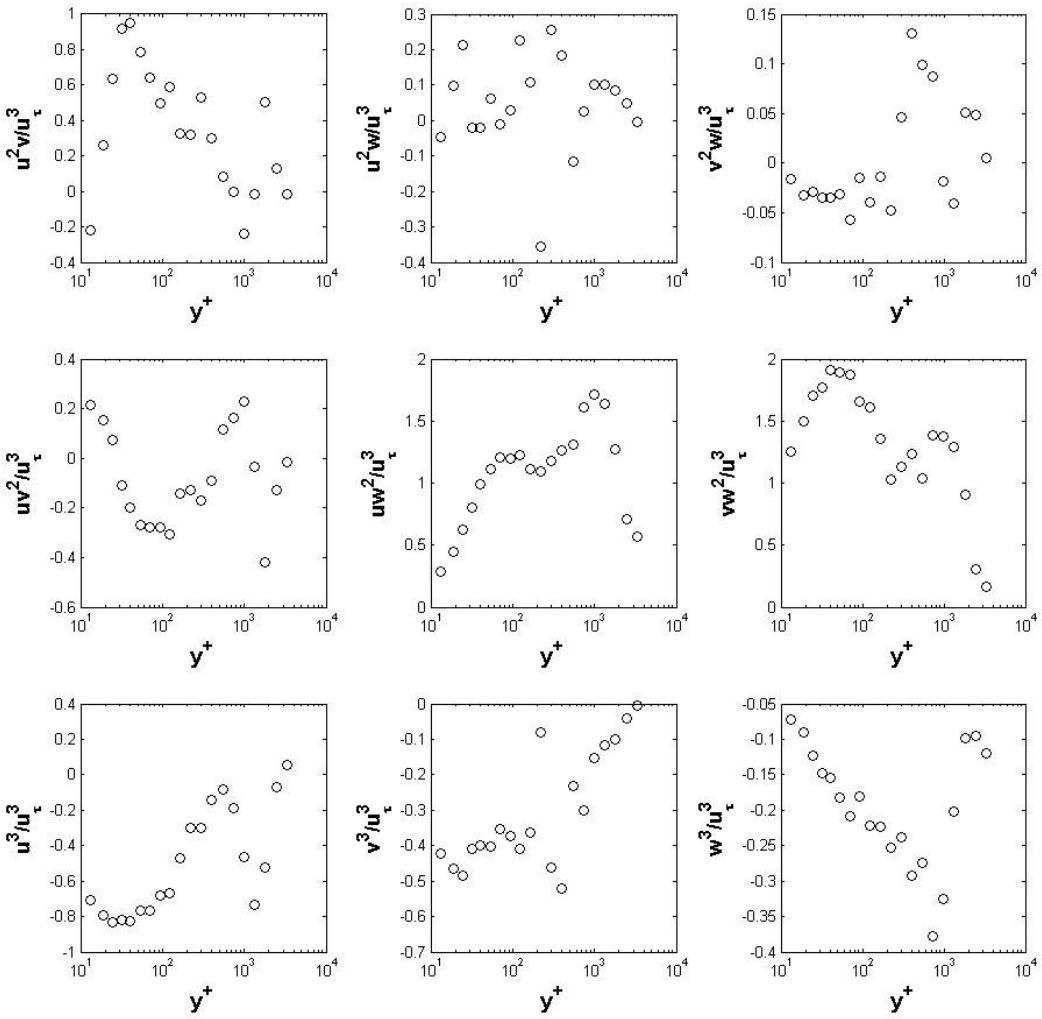

Figure A.3.10 Triple Products, z = 2.5 cm

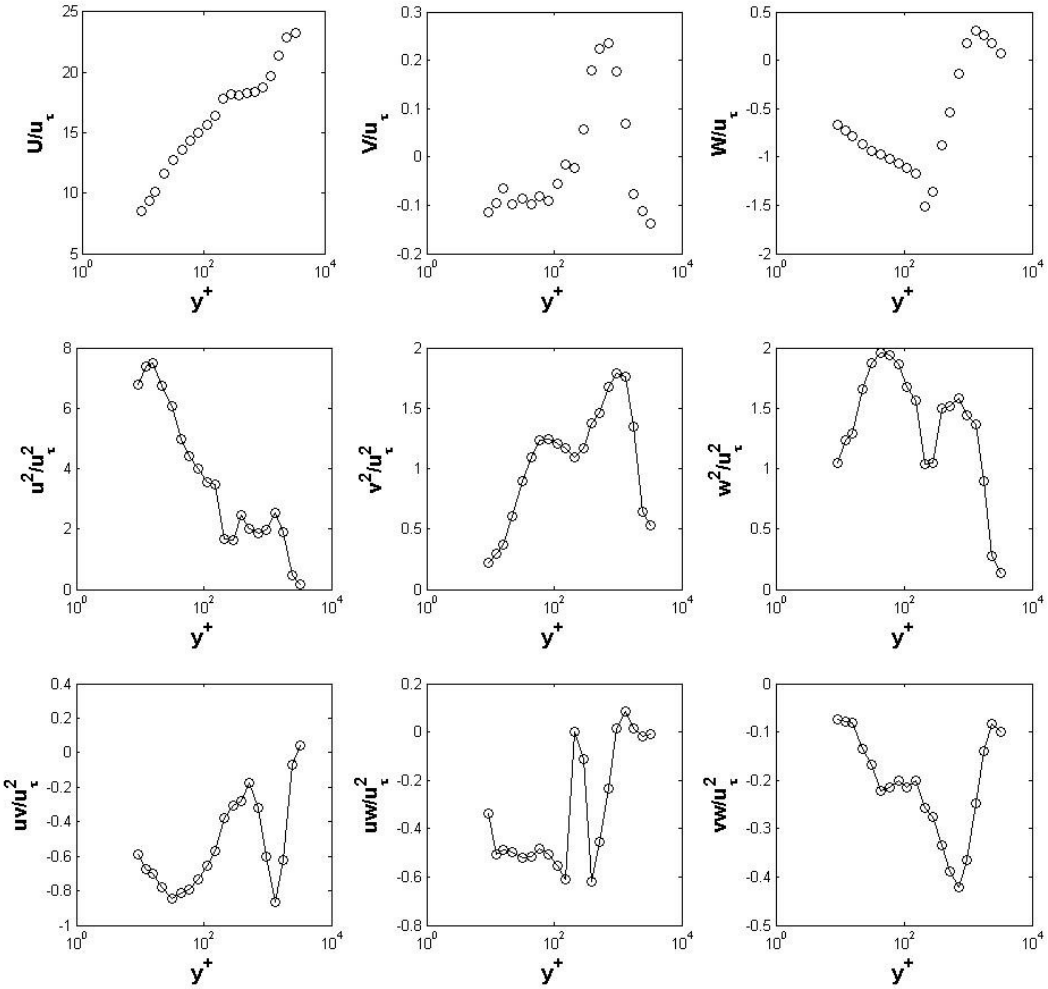

Figure A.3.11 Mean Velocities and Reynolds Stresses, z = 3.0 cm

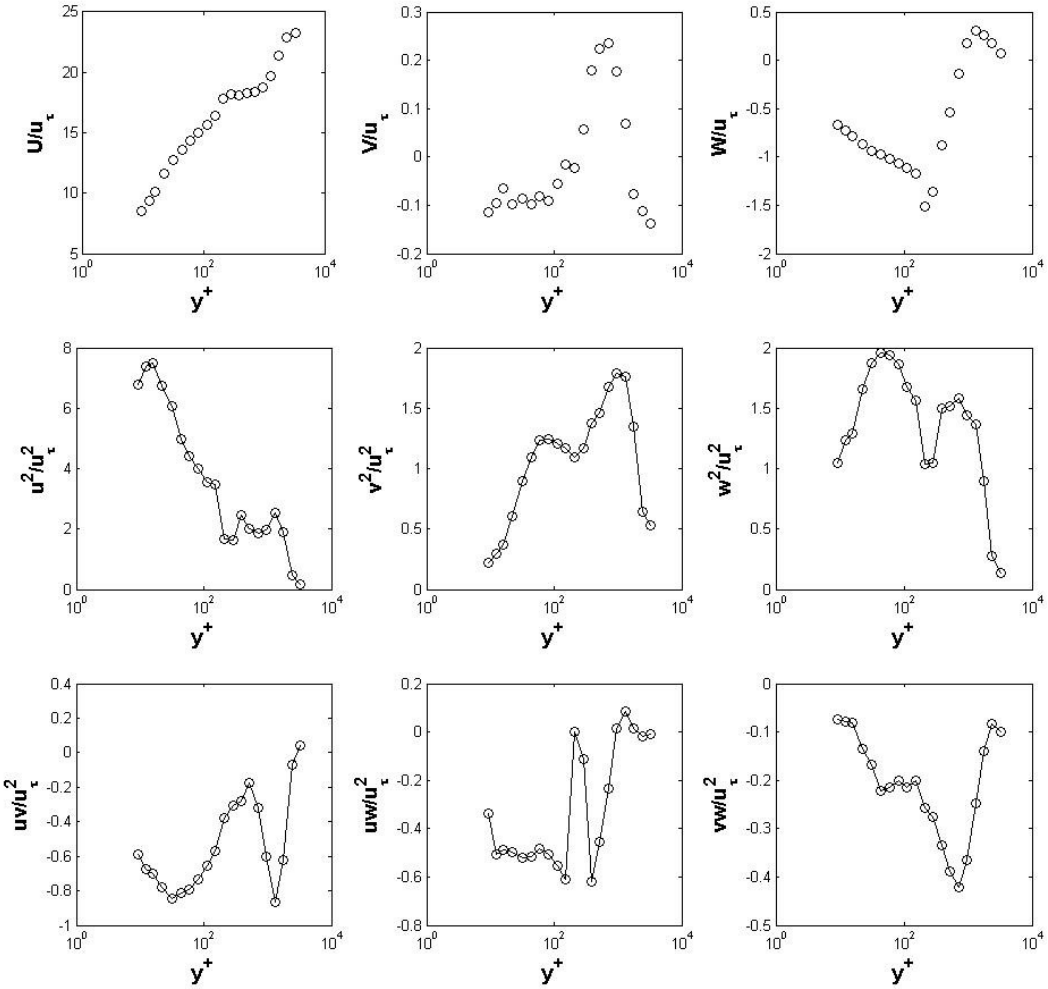

Figure A.3.12 Triple Products, z = 3.0 cm

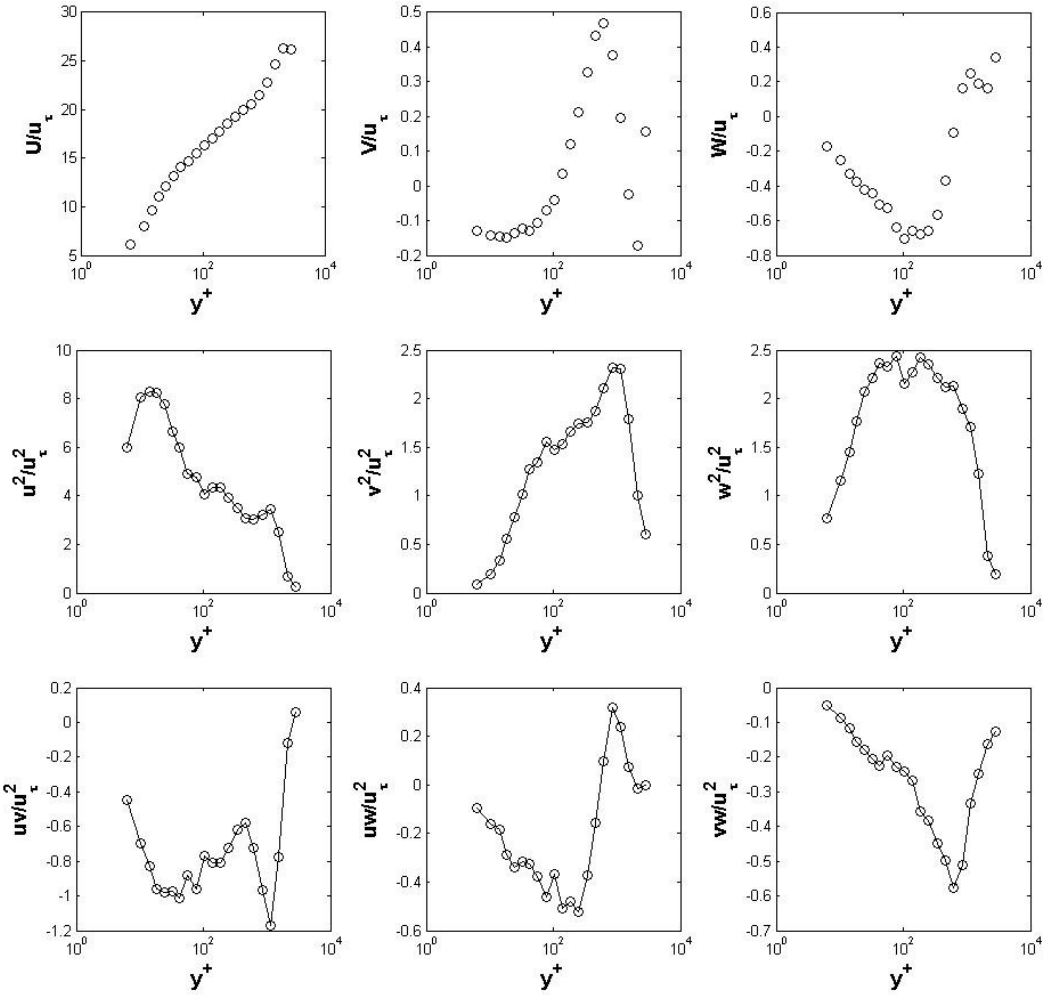

Figure A.3.13 Mean Velocities and Reynolds Stresses, z = 3.5 cm

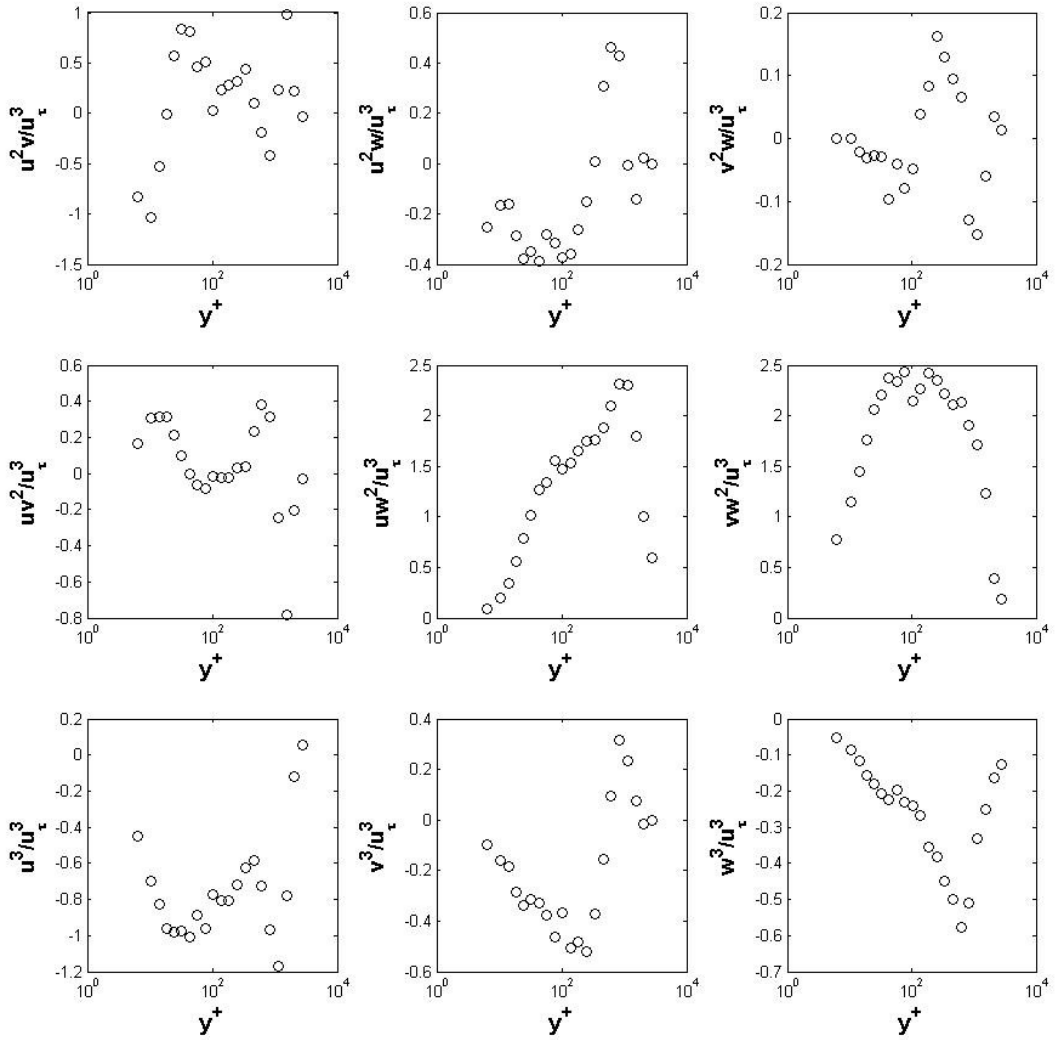

Figure A.3.14 Triple Products, z = 3.5 cm

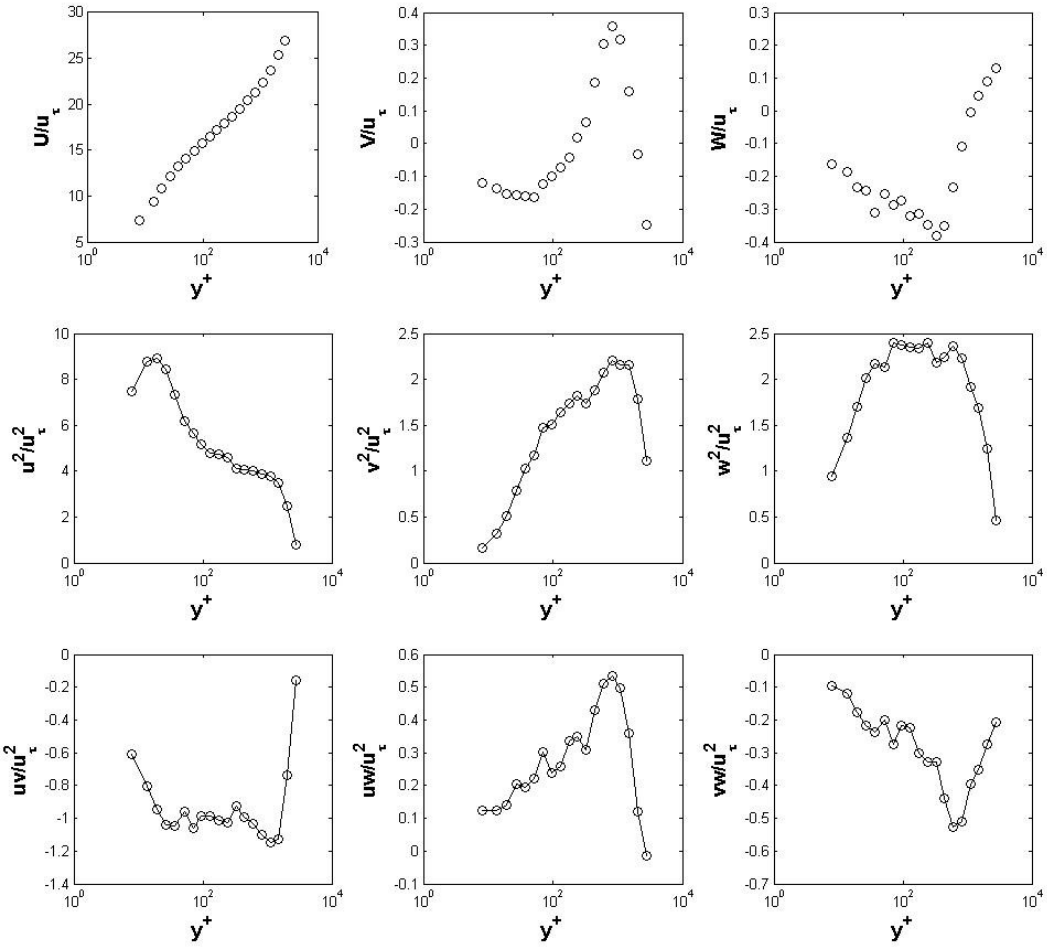

Figure A.3.15 Mean Velocities and Reynolds Stresses, z = 4.0 cm

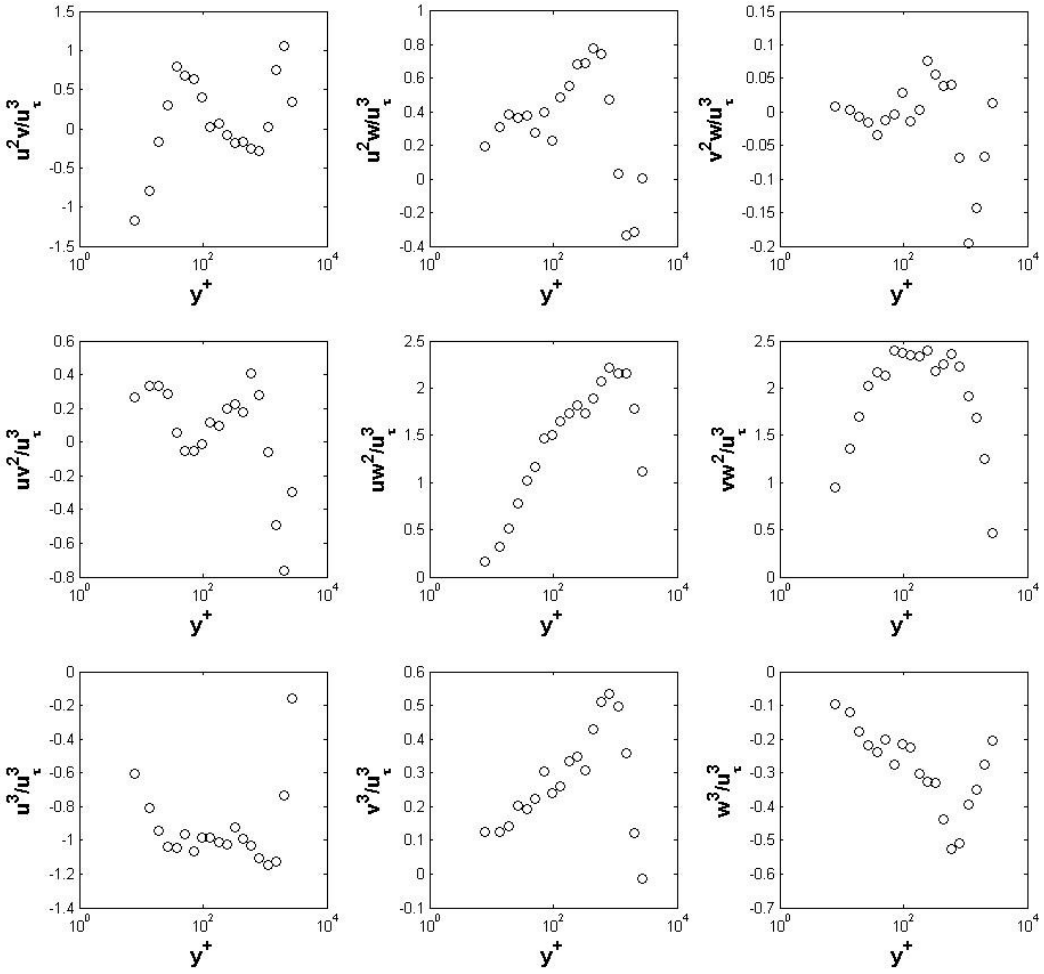

Figure A.3.16 Triple Products, z = 4.0 cm

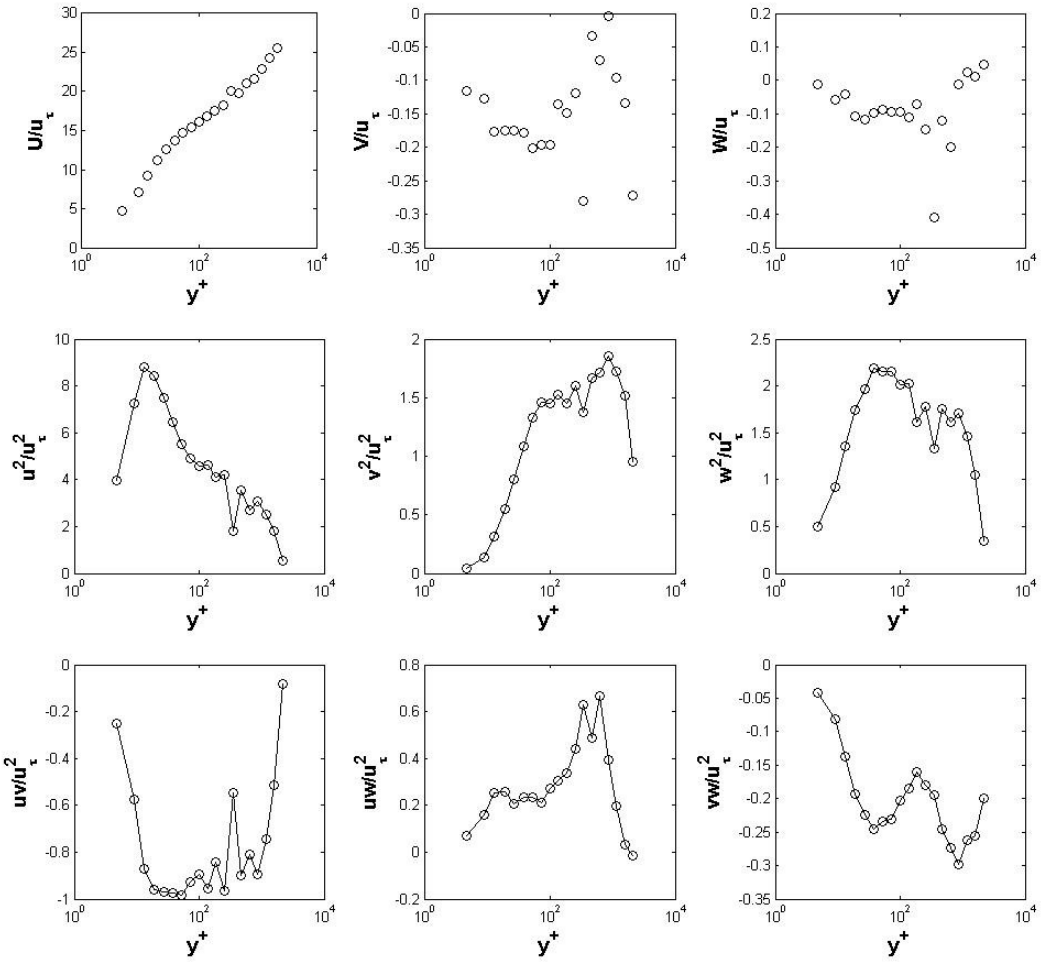

Figure A.3.17 Mean Velocities and Reynolds Stresses, z = 4.5 cm

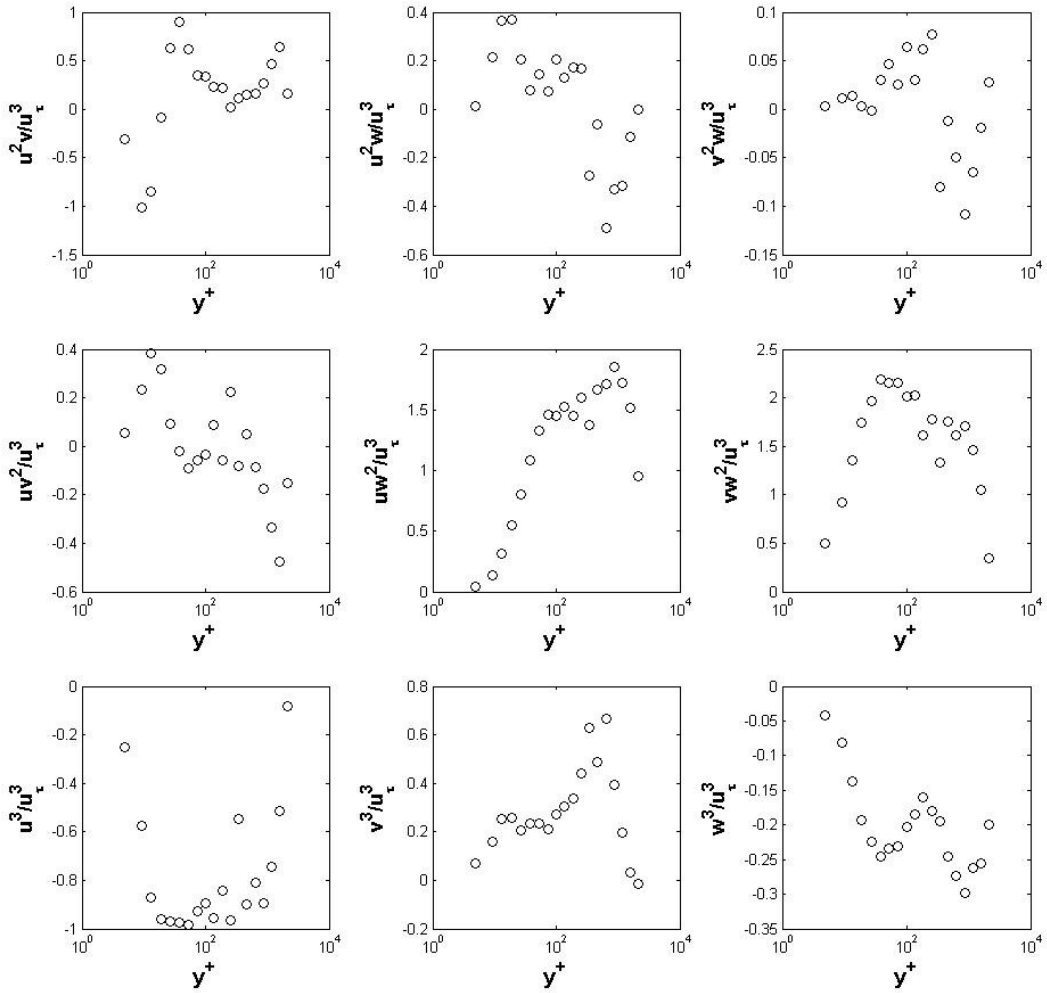

Figure A.3.18 Triple Products, z = 4.5 cm